Theoretical Modeling of Metallic Compounds with Versatile Properties by Combining First-Principles Calculations and Global Structure Prediction Algorithms

A Dissertation Presented for the

Doctor of Philosophy

Degree

The University of Tennessee, Knoxville

Jinseon Park

August 2020

Copyright © by Jinseon Park, 2020
All Rights Reserved.

ACKNOWLEDGEMENTS

First and foremost, I would like to express my sincerest gratitude to my research advisor, Dr. Mina Yoon. She provided me an opportunity to conduct my research at Oak Ridge National Laboratory with great colleagues. Dr. Mina Yoon introduced me to fascinating research topics and continued to support and encourage me so that I could complete my Ph.D. I would also like to thank my committee members, Dr. Hanno Weitering, Dr. Adolfo Eguiluz, Dr. Soren Sorensen, and Dr. Gerd Duscher, for their invaluable advice on my research and dissertation. The advice from the committee members provided good opportunities to broaden academic insights and perspectives.

I thank my colleagues and classmates, Rahul Soni, Hasitha Suriya-Arachchige, and Yadu Sarathchandran. The nights I spent discussing with them were the most valuable experiences of my Ph.D. and will remain unforgettable memories. I am also grateful for the help of research group members, Dr. Changwon Park, Dr. Lizhi Zhang, and Dr. Wei Luo. They provided vital help to me who had no prior experience in the numerical calculations, from configuring binary files to valuable discussions on various topics related to my research.

I am grateful for the sacrifice of my wife, Hana Jeon, who has raised our daughter pretty and healthy even in an unfamiliar environment for the past five years. And I am also thankful to my daughter, Hanseol Park, who has always been giving me the greatest happiness in the world.

Lastly, I would like to thank the South Korea government and the Army Headquarters for giving me the opportunity to pursue a Ph.D. in the United States.

ABSTRACT

Improving the target properties of existing materials or finding new materials with enhanced functionality for practical applications is at the heart of the materials research. In this respect, the first-principles approaches, which have been successfully integrated into modern high-performance computers, have become an indispensable part of the materials research, providing a better understanding of existing materials and guidance on the design of new materials. Using state-of-the-art computational/theoretical approaches that couple global structure prediction with *ab initio* density functional theory calculations, we investigate structural and electronic properties of Cs_xO [cesium oxides], $Li_{1+x}Mn_2O_4$ [lithium manganese oxides], and $Y_5Si_3H_x$ [hydrogenated yttrium silicide]. First, we identify thermodynamically stable crystal structures of Cs_xO ($1 \leq x \leq 3$), $Li_{1+x}Mn_2O_4$ ($0 \leq x \leq 1$), and $Y_5Si_3H_x$ ($0 \leq x \leq 8$), and analyze their properties that are relevant to practical applications. Cs_xO are known as low work function materials, and it is revealed that a very low work function (0.66 eV) is achievable for CsO compound over a relatively wide range of the oxygen chemical potential. Moreover, atomic adsorption on the surface of Cs_3O results in a decrease in the work function, which stems from the fact that it is an electride. In the case of $LiMn_2O_4$, a promising cathode material for secondary lithium-ion batteries, it is demonstrated that lithium insertion into the spinel structure results in the emergence of various degrees of freedom for crystal formation such as Li ions occupation sites, oxidation states of Mn ions, and local Jahn-Teller distortions. This finding suggests a possible cause of the cycle capacity fade. Finally, Y_5Si_3 is known as an electride that can improve catalytic reaction and reversibly store hydrogen. Investigation on the anionic electrons demonstrates that Y_5Si_3 contains two times more anionic electrons than reported value and that the anionic electrons are robust against lattice vibrations.

We also shed light on the hydrogenation mechanism of $Y_5Si_3H_x$ by identifying favorable hydrogen occupation sites and diffusion paths. It is revealed that the 1D hollow space is the dominant diffusion channel, and fast diffusion is possible in a specific hydrogen content range.

TABLE OF CONTENTS

1. Introduction 1

2. Theoretical and Computational Approaches 8

2.1 Density Functional Theory (DFT) 8

2.2 Global Structure Prediction 16

2.2.1 Global Structure Prediction Algorithms 16

2.2.2 Particle Swarm Optimization (PSO) 18

2.2.3 Global Structure Prediction Scheme Combining PSO with DFT 19

3. Cesium Oxides: Cs_xO 21

3.1 Background 21

3.2 Stable and Metastable Structures (x = 1, 2, and 3) 23

3.3 Surface Properties 31

3.3.1 Work Functions and Surface Energies (x = 1, 2, and 3) 35

3.3.2 CsO Immm (#71): The Lowest Work Function Structure 39

3.4 Changes in Work Functions due to Adatom Adsorption 44

3.4.1 Surface Dipole Moment Density and Work Function 44

3.4.2 Work Function Changes 46

3.5 Summary 57

4. Lithium Manganese Oxides: $Li_{1+x}Mn_2O_4$ 58

4.1 Background 58

4.2 Stable and Metastable Structures (x = 1, 1.5, and 2) 62

4.3 Electronic and Structural Properties Depending on the Stoichiometry (x) 64

4.3.2 Initial and Final Structures: $Li_xMn_2O_4$ (x = 1 and 2) 64

4.3.2 Intermediate Structures: $Li_xMn_2O_4$ (x = 1.5) 69

4.3.2.1 Oxidation States of Mn Ions 71

4.3.2.2 Crystal Sites Occupied by Li Ions 73

4.3.2.3 Configurations of Local Jahn-Teller Distortions 76

4.4 Summary 79

5. Yttrium Silicide: Y_5Si_3 80

5.1 Background 80

5.2 Structural and Electronic Properties of Y_5Si_3 as an Electride 82

5.2.1 Verification of the Presence of Anionic Electrons 82

5.2.2 Effect of Vibrational Modes on Anionic Electrons 89

5.2.3 Electron-Donating Ability of Y_5Si_3 (001) Surface to Metal Atoms 94

5.2.4 Crystal and Electronic Structures of Y_5X_3 (X = Si, Ge, Sn, and Pb) 99

5.3 Hydrogenation of Y_5Si_3 103

5.3.1 Stable Configurations of $Y_5Si_3H_x$ ($0.5 \leq x \leq 8$) 103

5.3.2 Diffusion of Hydrogen Ion in Y_5Si_3 Bulk Phase 126

5.3.3 Penetration of Hydrogen Atom and Molecule through Y_5Si_3 (001) Surface 132

5.4 Summary 140

6. Conclusion and Outlook 141

Bibliography 146

Vita 156

LIST OF TABLES

Table 3. 1 Space group and energy values of identified structures for CsO. Blue color indicates that the structure has been reported in literature. 25

Table 3. 2 Space group and energy values of identified structures for Cs_2O. Blue color indicates that the structure has been reported in literature. 27

Table 3. 3 Space group and energy values of identified structures for Cs_3O. Blue color indicates that the structure has been reported in literature. 29

Table 3. 4 Surface energies (γ) and work functions (Φ) of cesium oxide compounds with different orientation, cleavage plane, and terminations. 37

Table 3. 5 Changes in work functions upon the adsorption of atomic adsorbates on various surfaces. The unit of work function is eV. Negative work function changes are indicated by red color. 47

Table 3. 6 Work function changes of CsO (011) surface due to the structural deformation ($\Delta\Phi_1$) and the charge transfer ($\Delta\Phi_2$). 49

Table 4. 1 Information about identified structures for $Li_{1+x}Mn_2O_4$ (x = 0, 0.5, and 1) through global structure prediction. For index, S, I, and F stand for start, intermediate, and final composition, respectively. ΔE is the energy difference compared to the most stable structure of the corresponding composition. Local Jahn-Teller distortion represents the direction and type of the deformation for each $Mn^{(3+)}O_6$ octahedra, A character with an overbar indicates compression, otherwise elongation. 65

Table 4. 2 Linear combinations of d_{z^2} and $d_{x^2-y^2}$ representing relevant orbitals to elongations and compressions in the x, y, and z axes. The $d_{3z^2-r^2}$ orbital represents the more explicit form of the d_{z^2} 76

Table 5. 1 Electron configurations and amount of transferred charge for various metal atoms. ..98

Table 5. 2 Stable structures and corresponding energies for Y_5Si_3 (X = Si, Ge, Sn, and Pb) identified through crystal structure search. 99

Table 5. 3 Occupation sites of each hydrogen atom in $Y_5Si_3H_1$ 113

Table 5. 4 Occupation sites of each hydrogen atom in $Y_5Si_3H_{1.5}$ 118

Table 5. 5 Changes of structural parameters as x increases in $Y_5Si_3H_x$ 124

Table 5. 6 Diffusion barriers of possible paths for $Y_5Si_3H_x$ (x=0.5, 1, and 1.5). Initial and final sites for the hydrogen diffusion is given in parentheses. Site 1* is indicating a double occupation of hydrogen atoms in site 1. 130

LIST OF FIGURES

Figure 2. 1 Calculation scheme of combining PSO and DFT. 20

Figure 3. 1 Convex hull diagram and corresponding structures. (a) Convex hull diagram for Cs-O compounds. Each black triangle represents a structure identified through a global structure prediction, and blue triangles indicate the structures reported in the literature. (b) Atomic structures of the experimentally reported structures. (c) Atomic structures of CsO compound which show lower formation energy than the literature structure..24

Figure 3. 2 Band structure and DOS projected on each species for (meta)stable structures of CsO. 26

Figure 3. 3 Band structure and DOS projected on each species for (meta)stable structures of Cs_2O. 28

Figure 3. 4 Band structure and DOS projected on each species for (meta)stable structures of Cs_3O. 30

Figure 3. 5 Atomic structure and anionic electron density of (a) the most stable and (b-e) metastable structures of the Cs_3O compound. For the partial charge density of the anionic electrons, electronic bands near the Fermi level ($-1.2 < E-E_F < 0$ eV) are taken into account. Isosurfaces of the electron density is drawn to illustrate 1D or 2D anionic electron channels, and the isosurface level is chosen as the value that clearly shows an accumulation of the anionic electrons in the vacant space in the range of $0.0055 \sim 0.0065$ e/Å^3. 32

Figure 3. 6 Example of electrostatic potential energy. Atomic structure and the electrostatic potential energy along the z-direction are drawn for the Cs terminated CsO Immm (#71)

(001) surface. The two horizontal dotted lines indicate the vacuum level and the Fermi level. 33

Figure 3. 7 Work functions and surface energies for all surfaces examined in this study. Each structure is represented by its space group, and each circle corresponds to a particular surface. The vertical dotted line distinguishes different chemical compositions. 36

Figure 3. 8 Work functions and surface energies of 17 different surfaces of the CsO Immm (#71) structure. Each surface identified by four indices as described in the text. A different color is used to indicate each different surface orientation. 40

Figure 3. 9 surface free energy of 17 different surfaces of the CsO Immm (#71) structure as a function of oxygen chemical potential. The work function is also given by a numeric value inside the parentheses in the legend. 43

Figure 3. 10 Atomic structures of surface slabs with Li adsorbate. (a) Cs_3O $P6_3/mcm$ (100) surface. (b) Cs_2O $R\bar{3}m$ (001) surface. (c) CsO Immm (011) surface. (d) CsO Immm (001) surface. Upper 1/5 part of the slab with the adsorbate atom is fully relaxed. 45

Figure 3. 11 Changes in work functions upon the adsorption of atomic adsorbates on various surfaces. 47

Figure 3. 12 Relaxed structure of CsO Immm (#71) 011 surface with various adatoms. 49

Figure 3. 13 Change of the surface charge distribution and resulting surface dipole moment density of CsO (011) surface induced by (a) Na, (b) Al, and (c) Cl. 51

Figure 3. 14 Atomic structure and electron densities of Cl-adsorbed Cs_3O (100) surface. (a) Fully relaxed atomic structure. (b) The partial charge density of anionic electrons calculated from the anionic electron bands near the Fermi level. (c) Change of anionic electron

density upon the adsorption of the Cl on the surface. (d) Change of total electron density upon Cl adsorption. 53

Figure 3. 15 (a) Band structures and (b) DOS projected on each species of the Cs_3O (100) surface with and without the Cl adsorbate. 54

Figure 3. 16 Bader charge of adsorbate Cl on the Cs_3O (100) surface (a) Atomic structure of the surface and Bader volume for the Cl atom. (b) Integrated charge density of Cl Bader charge along the y-axis. The valence charge of the Cl atom is 7 e, whereas the Bader charge of the Cl is 7.896 e 55

Figure 3. 17 Changes in electron density and surface dipole moment density due to charge transfer between Cl adsorbate and Cs_3O (100) surface. 56

Figure 4. 1 Crystal structure of $LiMn_2O_4$, and phase transition from cubic spinel $LiMn_2O_4$ to tetragonal $Li_2Mn_2O_4$. 59

Figure 4. 2 Jahn-Teller distortions of MnO_6 octahedral complex. 60

Figure 4. 3 Common polymorphs of MnO_2 phase. The purple and brown octahedra indicate MnO_6 complexes with spin up and down Mn atoms. The grey polyhedra denote potential intercalation sites for inserted anions. Reprint from Ref. [112] 62

Figure 4. 4 Constraints imposed on crystal structure search. 63

Figure 4. 5 Crystal structures of the start (x = 0) and final (x = 1) compositions in (a) primitive unit cell and (b) pseudo-cubic unit cell. 66

Figure 4. 6 (a) Partial charge density in the energy range of -1.2 eV < $E-E_F$ < 0 eV. The isosurface is randomly selected to represent the shape of the Mn d orbital. (b) Total and orbital projected local density of states with both spin majority (positive) and minority

(negative) channel. While the contributions from every O ion are summed up, local DOS for each Mn ion is presented. 67

Figure 4. 7 (a) Identified structures through global structure prediction for $Li_{1.5}Mn_2O_4$. The black dots represent all the structures identified from the structure prediction, and the structures with the λ-MnO_2 framework are indicated by blue horizontal lines. (b) A schematic diagram for various degrees of freedom which can interplay to determine crystal and electronic structure. 70

Figure 4. 8 (a) Crystal structures of I-7 and I-9 representing two different charge states of Mn ions and (b) total and local density of states. Only the spin majority channel is depicted for Mn ions. 72

Figure 4. 9 (a) Crystal structure of the I-5, I-6, and I-7 with Li ions located in different crystal sites. (b) Total and local density of states 74

Figure 4. 10 Li intercalation into the octahedral 16c site (Li3) and change of positions of adjacent Li ions at 8a sites (Li1 and Li2). 75

Figure 4. 11 (a) Crystal structure of the I-1, I-3, and I-5 with different configurations of local Jahn-Teller distortions. (b) Partial charge density in the energy range of -1.2 eV < E-E_F < 0 eV. (c) Total and local density of states. Orbital projected local DOS for Mn3 of the I-1, and Mn2, Mn4 of the I-3 shows the linear combinations of d_{z^2} and $d_{x^2-y^2}$ orbitals in -1.2 eV < E-E_F < 0 eV with more contribution from $d_{x^2-y^2}$, which indicates elongations along the x or y axes. The direction can be determined by observing the partial charge dentisity. 78

Figure 5. 1 Crystal and electronic structures of Y_5Si_3 (a) Crystal structure of Y_5Si_3 with hexagonal lattice symmetry (space group of $P6_3/mcm$). Three yttrium and silicon atoms form a

triangular shape in the a-b plane, and these triangles form a 1D hollow space along the c-axis. (b) Atomically projected band structure and DOS. The blue lines in the band structure plot shows the contributions from the anionic electron (AE) site. 83

Figure 5. 2 Visualized anionic electrons. (a) Bader charge analysis is performed on a partial charge density (-1.5 eV < E-E_F < 0). The left figure shows a Bader volume for anionic electrons, and the right figure is an integrated charge density inside the Bader volume along the c-axis. The Bader volume contains 2.976 electrons, which is 1.488 per formula unit. (b) Distribution of a partial charge density (-0.5 eV < E-E_F < 0). Anionic electrons fill the 1D hollow space. 85

Figure 5. 3 Interactions between electrons from yttrium, silicon, and anionic electron site. (a) Symmetrically distinguishable atoms and anionic electron sites inside a unit cell. (b) Orbital projected DOS for each distinguishable atoms and anionic electrons. The purple boxes are indicating energy regions where interactions between each atom occur. (c) Partial charge densities of different energy ranges showing interactions between each atom and anionic electron.....87

Figure 5. 4 Projected band structure for each distinguishable atoms and anionic electron sites...88

Figure 5. 5 Phonon dispersion relation and Brillouin zone of Y_5Si_3.....90

Figure 5. 6 4th and 5th vibrational modes at Γ point. (a) Atomic configurations and (b) corresponding partial charge densities in the energy range of -1 eV < E-E_F < 0 eV for each vibrational mode.....91

Figure 5. 7 1st and 3rd vibrational modes at *A* point. (a) Atomic configurations and (b) corresponding partial charge densities in the energy range of -1 eV < E-E_F < 0 eV for each vibrational mode.....93

Figure 5. 8 Differential charge distribution of Y_5Si_3 (001) surface slab with metal atoms.....95

Figure 5. 9 Correlation between electron affinity and amount of transferred charge from Y_5Si_3 (001) surface to metal atoms. 97

Figure 5. 10 Crystal structures of Y_5X_3 (X=Si, Ge, Sn, and Pb). They all show the identical atomic configuration belonging to the hexagonal crystal system with a space group of $P6_3/mcm$ (#193). 100

Figure 5. 11 Changes of structural parameters of Y_5X_3 (X=Si, Ge, Sn, and Pb). Y-Y distance means the distance between yttrium atoms that build the triangular ring in the a-b plane....101

Figure 5. 12 Projected band structure and DOS of Y_5X_3 (X=Si, Ge, Sn, and Pb). The projected band structure shows contributions only from anionic electron sites.....102

Figure 5. 13 Restricted crystal structure search for identifying stable hydrogen occupation sites of $Y_5Si_3H_{0.5}$. 104

Figure 5. 14 Stable configurations of $Y_5Si_3H_{0.5}$ identified through crystal structure search. (a) ~ (e) Crystal structures of $Y_5Si_3H_{0.5}$ which contain one hydrogen atom in a unit cell. (f) Relative energy differences of identified configurations.....105

Figure 5. 15 Projected band structures and DOS of Y_5Si_3 and possible configurations of $Y_5Si_3H_{0.5}$ identified through crystal structure search. Contribution from the anionic electrons is indicated in purple color. 106

Figure 5. 16 Partial charge density of possible configurations of Y_5Si_3 and $Y_5Si_3H_{0.5}$ identified through crystal structure search. 3D and integrated (along c-axis) partial charge density in the energy range of $-0.5\ eV < E-E_F < 0$ are drawn. Amount of the Bader charges of the anionic electrons are calculated from partial charge density in the energy range of $-1.5\ eV < E-E_F < 0$. 108

Figure 5. 17 Differential charge density due to the insertion of a hydrogen atom into the site 1 of $Y_5Si_3H_{0.5}$. 109

Figure 5. 18 The effect of a hydrogen atom located at site 2 of $Y_5Si_3H_{0.5}$ on the charge distribution. (a) Crystal structure of the site 2 of $Y_5Si_3H_{0.5}$ where the hydrogen atom is located at another octahedron site surrounded by five yttrium and one silicon atoms outside of the 1D hollow space. (b) Partial charge density (-0.5 eV < E-EF < 0), and (c) differential charge density. (d) Integrated partial charge density along c-axis. Anionic electron density shows asymmetric distribution. (e) Integrated differential charge density along c-axis. The six blue circles indicate the position of Yttrium atoms. It shows different levels of charge depletion and accumulation depending on the position of the yttrium atom. 111

Figure 5. 19 Stable configurations of $Y_5Si_3H_1$ identified through crystal structure search. (a) ~ (e) Crystal structures of $Y_5Si_3H_1$ which contain two hydrogen atoms in a unit cell. (f) Relative energy differences of identified configurations. 112

Figure 5. 20 Projected band structures and DOS of Y_5Si_3 and possible configurations of $Y_5Si_3H_1$ identified through crystal structure search. Contribution from the anionic electrons is indicated in purple color. 114

Figure 5. 21 Partial charge density of Y_5Si_3 and possible configurations of $Y_5Si_3H_1$ identified through crystal structure search. 3D and integrated (along c-axis) partial charge density in the energy range of -0.5 eV < $E-E_F$ < 0 are drawn. Amount of the Bader charges of the anionic electrons are calculated from partial charge density in the energy range of -1.5 eV < $E-E_F$ < 0. 115

Figure 5. 22 Differential charge density due to the insertion of two hydrogen atoms into the config. 1 of $Y_5Si_3H_1$. 116

Figure 5. 23 Interaction between two hydrogen atoms in config. 1 and config. 2 of $Y_5Si_3H_1$. Projected band structure and DOS with partial charge density of bonding and anti-bonding electron band for (a) config. 1 and (b) config. 2. 117

Figure 5. 24 Stable configurations of $Y_5Si_3H_{1.5}$ identified through crystal structure search. (a) ~ (e) Crystal structures of $Y_5Si_3H_{1.5}$ which contain three hydrogen atoms in a unit cell. (f) Relative energy differences of identified configurations....119

Figure 5. 25 Crystal structures of the most stable configurations of $Y_5Si_3H_x$ ($0.5 \leq x \leq 4$) identified through crystal structure search. 121

Figure 5. 26 Crystal structures of the most stable configurations of $Y_5Si_3H_x$ ($4.5 \leq x \leq 8$) identified through crystal structure search. 122

Figure 5. 27 Changes in formation energy and structural parameters of $Y_5Si_3H_x$ ($0 \leq x \leq 8$) (a) Formation energy per formula unit, (b) volume of unit cell, (c) lengths of lattice vectors, and (d) angles between lattice vectors as a function of hydrogen content x. 125

Figure 5. 28 Diffusion paths for hydrogen migration in the unit cell of $Y_5Si_3H_{0.5}$. To clearly show the paths, the length of the c-axis is elongated three times. (a) Path 1: diffusion from site 1 to another site 1 along the c-axis. (b) Path 2: diffusion from site 1 to site 2 in the ab-plane. (c) Path 3: diffusion from site 1 to site 3 in the ab-plane....127

Figure 5. 29 Diffusion barriers for hydrogen migration in $Y_5Si_3H_x$ (a) x = 0.5, (b) x = 1, and (c) x=1.5. Images of the initial and final structures for each path are inserted inside the graph. For each composition, blue line is for the diffusion along the c-axis. Red and green lines are for diffusions in ab-plane. 129

Figure 5. 30 Energy barrier for penetration of a hydrogen atom through Y_5Si_3 (001) surface. (a) Energy of surface slab and force on the hydrogen atom as a function of the position of the hydrogen atom. (b) Differential charge densities at different positions of the hydrogen atom. 133

Figure 5. 31 Projected DOS of Y_5Si_3 (001) surface with a hydrogen atom at difference distances. Y1 and S1 mean the yttrium and silicon atom on the outermost surface. 135

Figure 5. 32 Energy barrier for penetration of a hydrogen molecule through Y_5Si_3 (001) surface. (a) Energy of surface slab and forces on hydrogen atoms as a function of the position of the bottom hydrogen atom. (b) Differential charge densities at different positions of the hydrogen atom. 137

Figure 5. 33 Projected DOS of Y_5Si_3 (001) surface with a hydrogen molecule at difference distances. Y1 and S1 mean the yttrium and silicon atom on the outermost surface...138

Chapter 1

Introduction

Metallic compounds are chemical compounds commonly found in nature and are used in a wide variety of devices because they show a broad spectrum of macroscopic behavior depending on their composition and crystal structure. Thanks to the development of theories and experimental techniques in condensed matter physics, the macroscopic properties of these crystalline materials can be understood and predicted at the atomistic level, and the field of materials science has evolved to improve the target properties of existing materials or find new materials with improved functionality for practical applications. Since various properties of metallic compounds are sensitive to the stoichiometry of the compound and the resulting crystal structure, adjusting the properties of materials by altering those parameters has been a widely used approach to improve the functionality of metallic compounds.

Even with state-of-the-art measuring equipment, however, sometimes it could be challenging to accurately measure the changing parameter and the resulting properties of a material at the same time, due to inherent characteristics of the material itself or the reaction. In addition, if the parameters, such as chemical composition, cannot be adjusted in real-time in the measuring equipment, it will take considerable time and effort to examine the correlation between the parameter and the resulting properties, because it is necessary to repeat the synthesis and measurement processes. In such cases, theoretical and computational approaches can play an essential role by providing clear understandings of physical phenomena and feasible guidance for the design of new materials.

Macroscopic behaviors of crystalline materials such as electronic, magnetic, chemical, and mechanical properties are determined by interactions between their constituents (nucleus and electrons) in a microscopic or atomistic level. In order to accurately understand and predict the properties of these materials at the atomistic level, we need to solve the Schrödinger equation that governs the behavior of quantum mechanical particles. The Schrödinger equation is an eigenvalue equation of a Hamiltonian operator, in which the energy of the system is an eigenvalue, and the wavefunction is an eigenfunction corresponding to each eigenvalue. Once the Hamiltonian operator that accurately describes the system is defined, including the interactions between the constituent particles, wavefunctions representing states of the system can be obtained by solving the equation. Instead of employing an empirical or semi-empirical model explaining experimental data of a particular macroscopic phenomenon, the method of describing the state of the condensed matter system by directly solving the Schrödinger equation is called the first-principles method.

In this study, the Density Functional Theory (DFT) [1,2] implemented in the Vienna Ab initio Simulation Package (VASP) [3] was used. The DFT enables us to calculate band structure, density of states, charge density, etc. We can also estimate the number of electrons assigned to each atom or the energy barrier for atomic migration by combining the DFT with Bader charge analysis [4,5] and nudged elastic band calculation [6,7].

However, methods for predicting various properties of materials using numerical calculations require a crystal structure as the necessary input data, so we have to start from the assumption that we know the crystal structure. However, even if the material has the same chemical composition, its physical, chemical, and mechanical properties can vary greatly depending on its allotropic form, and carbon is a typical example. Even materials consisting of only carbon atoms show different structures, such as graphite and diamond, depending on their crystal structure, and such

polymorphs show significant differences in physical and chemical properties. Even for this simple carbon compound, researches are still underway to find new, unknown structures [8]. Therefore, identification of the crystal structure is not only the first step in the study of materials but also an essential process for subsequent characterization.

In particular, the importance and necessity of the crystal structure prediction have been increasing in the field of materials design, but it has been challenging to predict stable crystal structure even for a simple chemical composition containing a few atoms in a unit cell. John Maddox's News and Views article in Nature [9] published in 1988, just 30 years ago, begins with the following sentence, which stresses the difficulty of crystal structure prediction. “One of the continuing scandals in the physical sciences is that it remains in general impossible to predict the structure of even the simplest crystalline solids from a knowledge of their chemical composition." Due to this difficulty in structure prediction, trial and error processes had to be repeated numerous times to synthesize a material with target properties.

In recent decades, however, various approaches for predicting the crystal structure of a specific chemical composition have been proposed and improved, making the research in the global structure prediction or the global structure optimization itself an essential and indispensable subfield of computational materials science [10-13]. These methods explore the energy landscape using trial structures as starting points in the solution space and try to find the optimal structure by improving the structures using various algorithms.

Among various available algorithms, the particle swarm optimization [14,15] implemented in the Crystal structure AnaLYsis by Particle Swarm Optimization (CALYPSO) software [16] was used in this study. The particle swarm optimization algorithm is one of the population-based algorithms, which is inspired by the social behavior of bird flocks or fish schools. This algorithm enables the

systematic exploration of stable structures for given chemical composition, and we can find not only the most stable structure but the metastable structure as well.

Thanks to the exponential growth of computational power along with the development of the first-principles methods and the global structure prediction algorithms described above, the time and efforts required for material design and development have been significantly reduced, and also the characterization of structures that was experimentally difficult to access has become possible.

The purpose of this study is to find correlation between the stoichiometry and properties of cesium oxides (Cs_xO, x = 1, 2, and 3), lithium manganese oxides ($Li_{1+x}Mn_2O_4$, x = 0, 0,5 and 1), and hydrogenated yttrium silicide ($Y_5Si_3H_x$, $0 \leq x \leq 8$) by applying the global structure prediction algorithm and first-principles calculations.

The cesium oxides exhibit two interesting properties. First, Cs_3O was identified as an electride with 1D building blocks [17], and the anionic electrons are distributed in the interstitial space between the building blocks. This material was the first electride with a non-trivial band topology. And, the low work function is also an interesting property of this material. Cesium itself exhibits a low work function of around 2 eV, and it has been demonstrated that the oxidation can significantly lower its work function [18] making it promising surface coating material for electronic devices such as thermionic energy converters [19], light-emitting devices [20], and solar cells [21]. However, the clear relationship between chemical composition, crystal structure, and the work function has not been fully established. This is because the experimental characterization of cesium oxides is still challenging due to its high air sensitivity, unusually large number of oxides with different ratios, and poor crystallinity. There have been limited experimental studies in which experimental environments were carefully designed [22,23]. Therefore, in this study, crystal structures and their electronic properties were investigated by combining the global structure

prediction algorithms and first-principles calculations. The global structure prediction was utilized to identify (meta)stable structures for chemical compositions of Cs_3O, Cs_2O, and CsO. After identifying stable structures, the relationship between stoichiometry, crystal structure, and the work function was investigated. The change of work function with the increase of oxygen contents showed a trend consistent with the experimental data, and it was theoretically confirmed that a work function of 0.66eV is possible by comparing surface free energies of various possible facets. It was also demonstrated that, in the case of Cs_3O known as an electride, adsorption of electronegative atoms results in a decrease in the work function. This phenomenon is caused by the redistribution of charge density near the surface where the adatom penetrates deep into the surface through the interstitial space of the Cs_3O lattice and absorbs anion electrons.

Next, Lithium manganese spinel, $LiMn_2O_4$, is one of the promising cathode materials for Li-ion rechargeable battery, where Li intercalation and extraction are an underlying mechanism for charge and discharge process. However, in the $0 < x < 1$ range of $Li_{1+x}Mn_2O_4$, the spinel structure experiences a phase transition from cubic to tetragonal structure due to the cooperative Jahn-Teller distortion of $Mn_6^{(3+)}O$ complexes. The Jahn-Teller distortion refers to the phenomenon of lowering the overall energy of an ionic complex by breaking of symmetry. This phase transition leads to anisotropic volume change, which is known as a major cause of the cycle capacity fade. To examine the phase transition process more closely, we need to have information about structures in the intermediate phase. However, since the transition proceeds in the two-phase reaction [24,25], the intermediate structures can occur only in a fairly narrow interface between $LiMn_2O_4$ and $Li_2Mn_2O_4$. As a result, experimental identification of the intermediate structures is practically challenging. In this respect, $Li_{1+x}Mn_2O_4$ is a suitable material for applying global structure prediction algorithm to explore the unknown intermediate phases. Since MnO_2 is a chemical

composition with various polymorphs, a constrained structure search was applied to effectively explore the intermediate phases associated with spinel structure. Also, because the lithium manganese oxides are strongly correlated materials containing highly localized d-electrons in Mn ions, a DFT+U method where Hubbard U term is added to the exchange-correlation functional was used to reflect onsite Coulomb interaction.

Through the constrained crystal structure prediction, twelve (meta)stable structures were identified within a narrow energy range of 40 meV/atom for $Li_{1.5}Mn_2O_4$. This implies that several different structural phases can exist as a mixed state in the off-stoichiometric stage of Li intercalation, which may deteriorate the cycle capacity of the secondary battery. The factors affecting the diversity of intermediate phases were systematically analyzed in terms of occupation sites of Li ions, charge states of Mn ions, and local Jahn-Teller distortions.

Finally, Y_5Si_3 is one of the electrides where anionic electrons reside in the 1D void space of the hexagonal lattice, and those anionic electrons are not strongly bound to any atoms. Due to the presence of anionic electrons, it has been expected that electrides can be used as a catalyst for the chemical reaction, which requires electrons. In 2016, It was demonstrated that Y_5Si_3 can enhance catalytic activity for direct ammonia synthesis, and this is attributed to the strong electron-donating ability of this material [26]. By donating electrons to nitrogen molecules, it can reduce the activation energy of nitrogen dissociation by half compared to conventional catalysts [27]. Another promising application of this material is an ion storage and transport. Since the electrides structurally exhibit hollow spaces, it has been expected that those void spaces can be used as a channel for ion transport. From hydrogenation experiments of this material, reversible hydrogen storage has been demonstrated, and a rapid change in the hydrogen diffusion rate accompanied by an alteration in crystal structure was observed [28]. The fast diffusion of the hydrogen in the

$Y_5Si_3H_x$ lattice was possible only in the specific hydrogen content range, $1 < x < 2$. Although the electron-donating ability for catalytic activity and the potential for ion transport using 1D hollow space inside the lattice have been demonstrated in experiments, the electronic properties of Y_5Si_3 itself and the exact mechanism of the hydrogenation process have not yet been fully understood. In this study, qualitative and quantitative analysis on the anionic electrons of the Y_5Si_3 was performed, and it was demonstrated that this material contains twice the anionic electrons than the reported value. Furthermore, through systematic exploration using crystal structure search, the crystal structure and hydrogen diffusion rate at different hydrogen content were examined, and the cause of fast diffusion occurring in a specific hydrogen content was elucidated.

Chapter 2

Theoretical and Computational Approaches

2.1 Density Functional Theory (DFT)

The time-independent and non-relativistic many-body Schrödinger equation for a system containing N electrons and M nuclei is given by

$$\hat{H}\Psi(\vec{r}_1,\vec{r}_2,...,\vec{r}_N,\vec{R}_1,\vec{R}_2,...,\vec{R}_M) = E\Psi(\vec{r}_1,\vec{r}_2,...,\vec{r}_N,\vec{R}_1,\vec{R}_2,...,\vec{R}_M)$$

where the wave function $\Psi(\vec{r}_1,\vec{r}_2,...,\vec{r}_N,\vec{R}_1,\vec{R}_2,...,\vec{R}_M)$ is a function of the coordinates for the electrons ($\vec{r}$) and nuclei ($\vec{R}$). The Hamiltonian operator describing this system can be written as

$$\hat{H} = \hat{T}_N + \hat{T}_e + \hat{V}_{N\text{-}e} + \hat{V}_{e-e} + \hat{V}_{N-N}$$

or more specifically,

$$\hat{H} = -\sum_{A=1}^{M}\frac{1}{2M_A}\nabla_A^2 - \sum_{i=1}^{N}\frac{1}{2}\nabla_i^2 - \sum_{i=1}^{N}\sum_{A=1}^{M}\frac{Z_A}{|\vec{r}_i-\vec{R}_A|} + \sum_{i=1}^{N}\sum_{j>i}^{N}\frac{1}{|\vec{r}_i-\vec{r}_j|} + \sum_{A=1}^{M}\sum_{B>A}^{M}\frac{Z_AZ_B}{|\vec{R}_A-\vec{R}_B|}$$

in atomic units ($m_e = \hbar = \mathrm{e}^2/(4\pi\varepsilon_0) = 1$). The first two terms are associated with the kinetic energy of the nuclei ($\hat{T}_N$) and electrons ($\hat{T}_e$), and the remaining terms are describing the electrostatic Coulomb interactions between nuclei-electrons ($\hat{V}_{N-e}$), electrons-electrons ($\hat{V}_{e-e}$), and nuclei-nuclei ($\hat{V}_{N-N}$).

Although exact analytic solutions of the Schrödinger equation exist for simplified problems such as hydrogen-like ions, it is practically impossible to analytically solve the many-body Schrödinger equation even for a small system with more than three particles [29]. However, methods have been proposed to solve the many-body Schrödinger equation as accurately as possible using various approximations. First, with the help of the Born-Oppenheimer approximation [30], the motion of the nuclei and electrons of a many-nuclei-electrons problem can be separated by assuming the electrons move much faster than the nuclei. This approximation is a reasonable approach given that the proton is 1,800 times heavier than the electron. Although several approaches have been proposed to include the non-adiabatic effect coming from the coupling between the motion of the nuclei and electrons recently [31-34], the Born-Oppenheimer approximation can still predict reasonably accurate results for phonon frequencies [35] and molecular dynamics [36,37] in wide range of systems. According to the Born-Oppenheimer approximation, we can consider the electrons as moving particles in the field of fixed nuclei, and the associated equation for the electrons is expressed as follow.

$$[\hat{T}_e + \hat{V}_{N\text{-}e}(\{\vec{R}_A\}) + \hat{V}_{e\text{-}e}]\psi(\vec{r}_1,\vec{r}_2,...,\vec{r}_N) = E(\{\vec{R}_A\})\psi(\vec{r}_1,\vec{r}_2,...\vec{r}_N)$$

Also, the large mass of nuclei allows us to ignore the quantum effect and predict the movement of ions using the classical Newton equation rather than the time-dependent Schrödinger equation by calculating the Hellmann-Feynman forces [38]. However, the problem of finding the ground state energy by solving the many-electron Schrödinger equation is still challenging because the N-electron Hamiltonian and the wave function depends on 3N spatial variables associated with the N electrons.

In 1964, the foundation of the DFT was established by Hohenberg and Kohn [1] by proving that the Hamiltonian of the many-electron system can be uniquely determined by the electron density $\rho(\vec{r})$ instead of the 3N spatial variables of the electrons. They also suggested that the ground state energy can be expressed as a unique functional of the electron density.

According to the first Hohenberg-Kohn theorem (proof of existence), the ground state density uniquely related to the external potential $V_{ext}(\vec{r})$ and therefore determines the Hamiltonian and, in principle, all properties of the system.

$$\rho_0(\vec{r}) \Rightarrow V_{ext}(\vec{r}) \Rightarrow \hat{H} \Rightarrow \Psi$$

Based on this theorem, Hohenberg and Kohn suggested that the ground state energy of the N-electron system in an external potential $V_{ext}(\vec{r})$ can be expressed as a functional of the electron density

$$E_0[\rho_0(\vec{r})] = T[\rho_0(\vec{r})] + E_{N-e}[\rho_0(\vec{r})] + E_{e-e}[\rho_0(\vec{r})]$$

or

$$E_0[\rho_0(\vec{r})] = \int d\vec{r}\,\rho_0(\vec{r})V_{ext}(\vec{r}) + F[\rho_0(\vec{r})]$$

where $E_{N-e}[\rho_0(\vec{r})] = \int d\vec{r}\,\rho_0(\vec{r})V_{ext}(\vec{r})$, and $F[\rho_0(\vec{r})] = T[\rho_0(\vec{r})] + E_{e-e}[\rho_0(\vec{r})]$. The former term, $E_{N-e}[\rho_0(\vec{r})]$, represents the Coulomb interaction energy between the electrons and the external potential generated by the nuclei, and this is system dependent. The latter, $F[\rho_0(\vec{r})]$, corresponds to the kinetic energy and the electron-electron interaction energy including classical Coulomb,

exchange, and correlation energy, and this is called the Hohenberg-Kohn functional. This Hohenberg-Kohn functional is the universal functional completely independent of the system.

Given the explicit form of the energy functional (not described in the Hohenberg-Kohn theorem itself), to obtain the energy of the ground state, the electron density of the ground state must be found. This can be achieved by applying the variational principle, which is the second part of the Hohenberg-Kohn theorem stating that the energy functional delivers the lowest energy if and only if the trial density $\rho(\vec{r})$ corresponds to the correct ground state density $\rho_0(\vec{r})$.

$$E_0[\rho(\vec{r})] = \min E[\rho(\vec{r})] \quad \Leftrightarrow \quad \left.\frac{\partial E[\rho(\vec{r})]}{\partial \rho(\vec{r})}\right|_{\rho(\vec{r})=\rho_0(\vec{r})} = 0$$

Therefore, by minimizing the energy functional with respect to the electron density, we can identify the ground state energy as well as the corresponding electron density. Although Hohenberg and Kohn demonstrated the theoretical justification of using the electron density as a fundamental variable for describing the electronic state of a system, the explicit form of the Hohenberg-Kohn functional and the practical way to find the electron density of the ground state had not yet been established.

In 1965, Kohn and Sham introduced the concept of a non-interacting reference system consisting of non-interacting one-electron wavefunctions and generating the same density as the actual interacting system, allowing the approximate calculation of the ground state electron density and the ground state energy [2]. In the Kohn-Sham (KS) theory, the electron density is expressed as

$$\rho(\vec{r}) = \sum_i \phi_i^*(\vec{r})\phi_i(\vec{r})$$

where $\phi_i(\vec{r})$ are the KS orbitals obtained from the KS equation which will be explained later. The energy functional is expressed in the form of

$$E[\rho(\vec{r})] = T_s[\rho(\vec{r})] + E_H[\rho(\vec{r})] + E_{XC}[\rho(\vec{r})] + E_{ext}[\rho(\vec{r})]$$

where

$$E_H = \frac{1}{2}\iint \frac{\rho(\vec{r}_1)\rho(\vec{r}_2)}{|\vec{r}_1 - \vec{r}_2|} d\vec{r}_1 d\vec{r}_2$$

is the Hartree energy (or the classical part of the Coulomb interaction between the electrons), and

$$E_{ext} = \int V_{ext}(\vec{r})\rho(\vec{r})\, d\vec{r}$$

represents the intercation between the electrons and the external potential. The KS kinetic energy term is calculated by considering the non-interacting electrons in the KS orbitals $\phi_i(\vec{r})$

$$T_s[\rho] = \sum_i \int \phi_i^*(\vec{r})(-\frac{1}{2}\nabla^2)\phi_i(\vec{r})\, d\vec{r}$$

.

It should be noted that this term is not the exact kinetic energy of the interacting electrons, but the approximate kinetic energy of the non-interacting electrons.

The only unknown part of the energy functional is the so-called exchange-correlation functional $E_{XC}[\rho(\vec{r})]$, which contains the remaining portion of the exact kinetic energy not covered by T_s, and non-classical contributions from the electron-electron interaction.

Now, we can apply the variational principle to find KS orbitals $\{\phi_i(\vec{r})\}$ minimizing the energy functional under the orthonormal condition for KS orbitals $\langle\phi_i|\phi_j\rangle = \delta_{ij}$ as a constraint. This variational method results in N one-electron Schrödinger-like equations with effective potential $V_{eff}(\vec{r})$ and Lagrange multipliers ε_i, and the ε_i is called KS orbital energies. The resulting equations are KS equations and expressed as

$$\left(-\frac{1}{2}\nabla^2 + V_{eff}(\vec{r})\right)\phi_i(\vec{r}) = \varepsilon_i\phi_i(\vec{r})$$

where

$$V_{eff}(\vec{r}) = \int \frac{\rho(\vec{r}')}{|\vec{r}-\vec{r}'|}d\vec{r}' + V_{ext}(\vec{r}) + V_{XC}.$$

The V_{XC} is a functional derivative of the exchange-correlation energy E_{XC}.

$$V_{XC} = \frac{\delta E_{XC}[\rho(\vec{r})]}{\delta\rho(\vec{r})}$$

By solving these KS equations, we can get the KS orbitals (and the electron density) minimizing the energy of the N-electron system. However, it should be noted that because the effective potential $V_{eff}(\vec{r})$ itself depends on the electron density $\rho(\vec{r})$ constructed from the KS orbitals $\{\phi_i(\vec{r})\}$, these equations have to be solved in an iterative way.

Although we have a well-established formalism for calculating the electron density and corresponding ground state energy from the Kohn-Sham theory, accurate calculations are possible only if an explicit form of the $E_{XC}[\rho(\vec{r})]$ is available, and the quality of the DFT calculation is

determined by the accuracy for the approximation of the $E_{XC}[\rho(\vec{r})]$. The simplest form of the approximation first presented by Kohn and Sham is the local density approximation (LDA) [2]. In this approximation, the exchange-correlation energy of the electrons at each position is considered to be the same as that of the uniform electron gas having the same electron density as that position. Consiquentely, the exchange-correlation functional $E_{XC}[\rho(\vec{r})]$ is expressed as

$$E_{XC}^{LDA}[\rho(\vec{r})] = \int \rho(\vec{r})\varepsilon_{XC}(\rho(\vec{r}))\,d\vec{r}$$

where $\varepsilon_{XC}(\rho(\vec{r}))$ is the exchange-correlation energy per electron of a homogeneous electron gas of density $\rho(\vec{r})$. Although LDA has achieved a remarkable success despite its simplicity, other types of exchange-correlation functionals have been proposed, such as the generalized gradient approximations (GGA) and the hybrid functionals, to correct errors in LDA caused by neglecting the actual inhomogeneities of the electron density. The form of the exchange-correlation functional in the GGA approximations can be generalized by

$$E_{XC}^{GGA}[\rho(\vec{r})] = \int \rho(\vec{r})\varepsilon_{XC}(\rho(\vec{r}),\ |\nabla\rho(\vec{r})|,\ \cdots)\,d\vec{r}\,.$$

The GGA functionals are designed to incorporate the gradient or even higher derivatives of the electron density. In this study, the GGA functional proposed by Perdew, Burke, and Enzerhof (PBE) [39] was used for the majority of the calculations.

The accuracy and reliability of the DFT calculations have been further improved through the development and application of advanced exchange-correlation functionals [40] such as meta-GGA [41,42] and hybrid [43-46] functionals. However, challenges remained in the accurate prediction of properties of materials, which were implementations of the relativistic effect of heavy elements and the onsite Coulomb interaction in the strongly correlated system. First, electron's

spin magnetic moment always relativistically interacts with the magnetic field induced by electron's own orbital motion in the electrostatic field of nuclei, and this is called spin-orbit coupling (SOC). Although the SOC can be neglected for light elements, the strength of the relativistic effects becomes stronger as the atomic number increases. Therefore, when it comes to heavier elements, SOC should be considered, and this can be achieved by adding $H_{so}^{\alpha\beta}$ term into the Hamiltonian, which is proportional to $\vec{\sigma}^{\alpha\beta} \cdot \vec{L}$, where $\vec{\sigma} = (\sigma_x, \sigma_y, \sigma_z)$ are the (2×2) Pauli spin matrices and $\vec{L}$ is the angular momentum operator [47]. Here, α and β stands for the spin-up and spin-down components of the two-component spinor wave functions.

Another challenge in the DFT calculations is the treatment of strongly correlated materials. The strongly correlated system refers to a material in which onsite Coulomb repulsion is considerably larger than intersite hopping energy, and transition metal oxides containing highly localized d- or f-electrons are typical examples. In the DFT approaches, the electron-electron interaction is expressed as the sum of the classical Coulomb interaction (Hartree energy, E_H) and the exchange-correlation energy (E_{xc}). Since the DFT is based on the non-interacting reference system consisting of one-electron wavefunctions, the DFT calculates the E_H in the way of the mean-field approximation. Therefore, the E_H intrinsically contains unphysical self-interaction energy, and the E_{xc} should ultimately cancel this. The failure of the accurate description of the strongly correlated system stems from the incomplete cancellation of the self-interaction energy embedded in the E_H. The inadequate cancellation of this unphysical energy leads to an over-delocalization of valence electrons, and this is why the standard DFT cannot accurately describe the highly localized d- and f-electrons. Several methods have been proposed to devise this problem and accurately describe the strongly correlated system [48], and DFT+U is one of the widely used methods due to its simple and easy implementation [49-53]. In the DFT+U approach, the strong onsite Coulomb interactions

of the highly localized (strongly correlated) d- and f-electrons are described by using the Hubbard model with Hubbard U value, and the remaining electrons are treated as in the standart DFT [54]. In addition to the DFT+U approach, methods such as DFT+Dynamical Mean Field Theory (DFT+ DMFT) [55,56], Reduced Density Matrix Functional Theory (RDMFT) [57,58] have been proposed, but these methods are computationally much more expensive than the standard DFT calculations.

Thanks to the improvements in approximation of exchange-correlation functionals, the development of practical algorithms, and the revolution of the computer technology, the DFT as a first-principle approach has been widely and successfully applied to predict various material's properties in the field of the condensed matter physics, quantum chemistry, and materials science [40,59,60].

2.2 Global Structure Prediction

2.2.1 Global Structure Prediction Algorithms

In the field of material design, there has been an increasing demand for the crystal structure prediction as a method for finding new materials with novel properties, and various global optimization algorithms have been consequently developed to meet these demands [10-13]. In recent years, this computational approach for finding stable structures has become an integral part of computational materials sciences, thanks to the exponential growth of computational power. Widely used methods include simulated annealing [61,62], basin hopping [63], metadynamics [64], genetic algorithm [65,66], and particle swarm optimization [16,67].

In the simulated annealing, basin hopping, and metadynamics methods, the search process starts from a single initial structure and perturbs the atomic configuration to overcome the energy barriers between neighboring polymorphs. The global minimum can be found by repeating this process. However, since we start the search from a single point in the solution space, it is limited to explore all possible local minimums extensively. Moreover, if the actual global minimum is far from the initial structure, a single execution of the algorithm cannot guarantee the prediction of the global minimum.

On the other hand, the genetic algorithm and the particle swarm optimization, which can be classified as population-based (or evolutionary) optimization algorithms, initiate the optimization process from multiple initial structures called population. Due to the diversity of the structures in the population, these algorithms can search a vast solution space efficiently by utilizing the information about the structural geometries and energies of the previous population to improve the structures of the next population. Each step (or generation) of these population-based optimization approaches consists of search, rank, and update stages. The search stage is to identify the locations (crystal structures) and energy values of the local minimums near the structures that make up the current population. This stage is typically performed in conjunction with the first-principles calculations using the density-functional theory. In the rank stage, the rank is determined by comparing the first-principles energy values of the local minimum. Finally, in the update stage, the structures of the next population are generated by updating the structures of the current local minimum utilizing unique algorithms depending on different optimization schemes.

In this study, global structure prediction using particle swarm optimization algorithm, which is one of the population-based optimization algorithms, was performed to identify not only the ground state structure but also metastable structures through extensive structure search.

2.2.2 Particle Swarm Optimization (PSO)

The PSO algorithm was first introduced in 1995 by Kennedy and Eberhart [14,15] as a biologically inspired optimization algorithm. In this algorithm, the movement of the candidate solutions in the solution space imitates the social behavior of bird flocks or fish schools. The PSO algorithm was first implemented in a practical software for prediction of crystal structures by Ma and co-workers [16] in 2010 and has been successfully applied to predict new materials such as nanoclusters, super-hard materials, and elecrides [67].

While the genetic algorithm improves the quality of candidate solutions by applying genetic operators such as mutation and crossover, the PSO avoids these operations and solves optimization problems very effectively by generating candidate solutions (which is called 'particles') and making them move around in the solution space according to a relatively simple updating formula composed of position and velocity, $\vec{x}_i^{t+1} = \vec{x}_i^t + \vec{v}_i^{t+1}$.

In the updating formula, $\vec{x}_i^t$ stands for the coordinate of the i^{th} particle in the current (t) generation before the local optimization, and $\vec{v}_i^{t+1}$ is the new velocity that determines the location of the i^{th} particle in the subsequent ($t+1$) generation. Here, it should be noted that the position vector $\vec{x}_i$ is not a 3 dimensional variable for each 'physical' particle (i.e., ions) included in the structure, but a 3N-dimensional variable including position information of N 'physical' particles included in the i^{th} crystal structure.

The velocity $\vec{v}_i^{t+1}$ is calculated by considering various outputs from the current generation.

$$\vec{v}_i^{t+1} = \omega\vec{v}_i^t + c_1 r_1(\vec{b}_i^t - \vec{x}_i^t) + c_2 r_2(\vec{g}_i^t - \vec{x}_i^t)$$

$\vec{v}_i^t$ is the current velocity and ω is the weight factor for the inertia of the velocity. $\vec{b}_i^t$ means the i^{th} particle's best location, which implies the location with the lowest energy experienced by the i^{th} particle up to the present time. Similary, $\vec{g}_i^t$ represents the global best location for the entire population. c_1 and c_2 reflect the self-confidence and swarm-confidence, respectively. Finally, r_1 and r_2 are random numbers between 0 and 1. The inertia weight factor and random numbers are intended to prevent premature convergence to the local minimum.

2.2.3 Global Structure Prediction Scheme Combining PSO with DFT

As described above, global structure prediction proceeds in three stages: search, rank, and update. The PSO algorithm performs its functions in the rank and update stages, and the PSO itself cannot carry out the search where we need to find a locally optimized structure near the updated structure. This search stage is performed through DFT calculation, and the result is transmitted to the PSO, so the overall structure prediction process proceed. Figure 2.1 is a schematic diagram presenting how DFT is combined with PSO to perform crystal structure prediction.

In the first step, a number of random structures are generated according to the population size. Then, DFT relaxation is performed on the current structures to search locally optimized structures. When this process complete, PSO updates the structures for the next generation based on the information of the optimized structures.

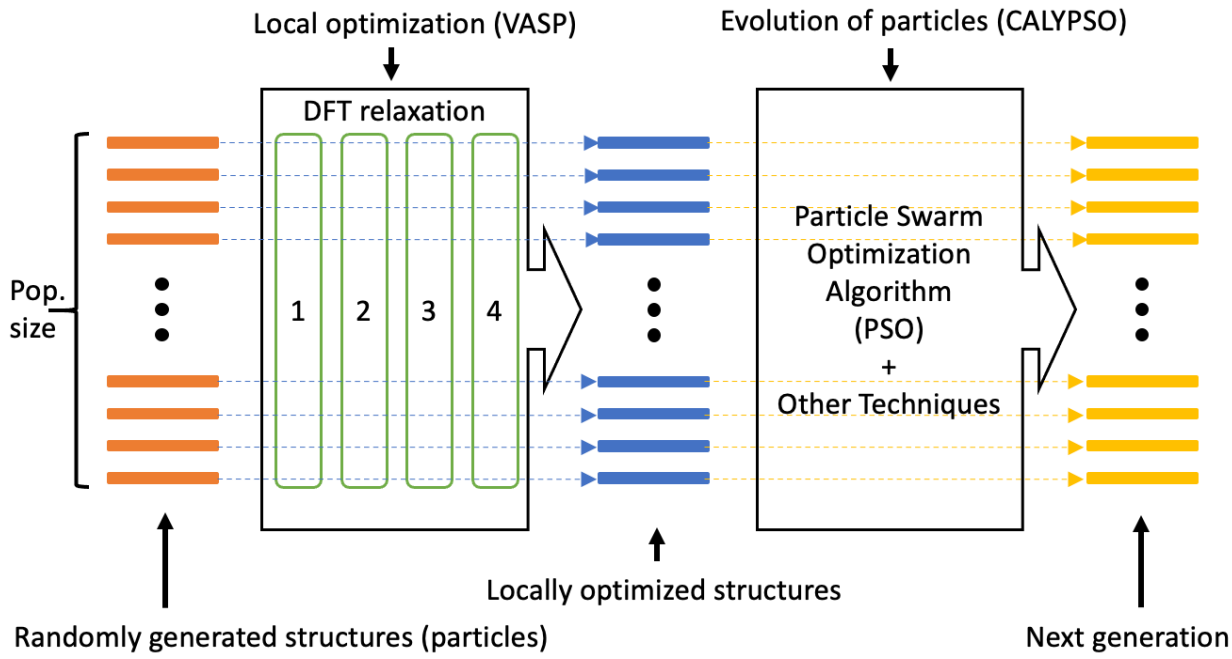


Figure 2. 1 Calculation scheme of combining PSO and DFT.

Chapter 3

Cesium Oxides: Cs_xO

3.1 Background

Alkali metals exhibit relatively low work functions, and cesium is known to show the lowest work function; the work function of polycrystalline cesium ranges between 1.95 and 2.14 eV [68,69], which makes it appealing for many technical applications. For example, a thin film coating of cesium helps to improve the photoelectric emission performance of the cathode [70-72]. The work function of cesium covered cathode can be further lowered through oxidation [73,74]; work functions of cesium oxide covered GaInAs [75] and GaAs [18], for example, reach to 0.8 and 0.7 eV, respectively. The low work function property of cesium oxides makes it also appealing as a surface coating and interfacial layer material to ameliorate the performance of other electronic devices such as thermionic energy converters [19], light-emitting devices [20], and solar cells [21].

Despite the successful application of cesium oxides coating to multiple electronic devices, our understanding of cesium oxide phases under the experimental conditions is far from complete. It is because cesium oxide compounds (Cs_xO_y) exist in many different stoichiometries with high chemical sensitivity [22,23,76], and it remains a challenge to characterize their structural properties and resultant electronic properties.

In this study, I employ first-principles DFT calculations coupled with global structure prediction algorithm to identify thermodynamically stable atomic configurations of Cs-O compounds with different chemical compositions (Cs_3O, Cs_2O, and CsO). Also, through additional first-principles

calculations on the identified structures, I verify previous experimental observations of decreasing trend in work function with increasing oxidation levels [77,78] and identify the lowest work function surface among various chemical compositions and possible surface facets.

However, no matter how low the work function of a particular surface is, it is meaningless if it is impossible to realize the surface experimentally. Therefore, it is necessary to check the thermodynamic stability of each surface under specific experimental conditions. Here, the experimental condition means oxygen chemical potential that can be controlled by temperature and pressure, and the thermodynamic stability of surfaces under different oxygen chemical potentials can be established by comparing surface free energies. I confirm the experimental feasibility of the lowest work function surface by comparing the surface free energy of the surface with other surfaces of the corresponding crystal structure.

One interesting phenomenon about work functions is that atomic adsorption on a material's surface can modify work functions [79-81]. The underlying mechanism of work function change is that the surface dipole moment density generated by the surface adatom forms a local electric field, thereby changing the energy barrier required for electrons to escape from the material. The reason for the surface dipole moment change is a redistribution of charge density near the outermost surface. DFT calculation can not only estimate the work function change through a direct calculation but also provide information which we need to explain the underlying mechanism of work function change by generating an electron density profile. It is confirmed that the mechanism of work function change appears exceptionally different in the case of Cs_3O ($P6_3/mcm$), recently reported electride [17], owing to the redistribution of “free” electrons distributed in its cavity space. Its work function is drastically reduced upon the adsorption of

electronegative atoms. Our theoretical study proposes a new avenue to develop ultralow work function materials for various technological applications.

3.2 Stable and Metastable Structures (x = 1, 2, and 3)

Figure 3.1 (a), a convex hull diagram, summarizes (meta)stable structures identified through the global structure search, where the formation energy (ΔE) is defined as

$$\left[E(\mathrm{Cs}_x\mathrm{O}_y) - \left(x \cdot E(\mathrm{Cs})/2 + y \cdot E(\mathrm{O}_2)/2\right)\right] / \left(x + y\right),$$

the energy difference to the reference systems, body-centered cubic (BCC) phase of bulk Cs and O_2 molecule in a gas phase. For each chemical composition, 5~9 polymorphs with different crystal structures were identified in the energy range of < 100 meV/atom.

The global structure search successfully reproduced the crystal structures reported in the literature (blue triangles in Fig. 3.1(a)), and Fig. 3.1(b) presents those structures: CsO with space group of Immm (#71) [82], multilayered Cs_2O with $R\bar{3}m$ (#166) space group [83], and Cs_3O with $P6_3/mcm$ (#193) [84] consisting of 1D building blocks forming large cavity space between the building blocks, reported as the first 1D electride with topological Dirac nodal lines [17]. The global structure search identifies two new CsO structures with space group of Pnnm (#58) and C2/m (#12) (see Fig. 3.1(c)), that are more stable than the one reported so far [82]. Although it is not guaranteed that all the identified structures through the global structure prediction are experimentally synthesizable, it is important to note that the energy difference of 100 meV/atom is within the free energy range that can be overcome by thermodynamic perturbations such as pressure and temperature [85]. Therefore, these metastable phases can be regarded as synthesizable candidates.

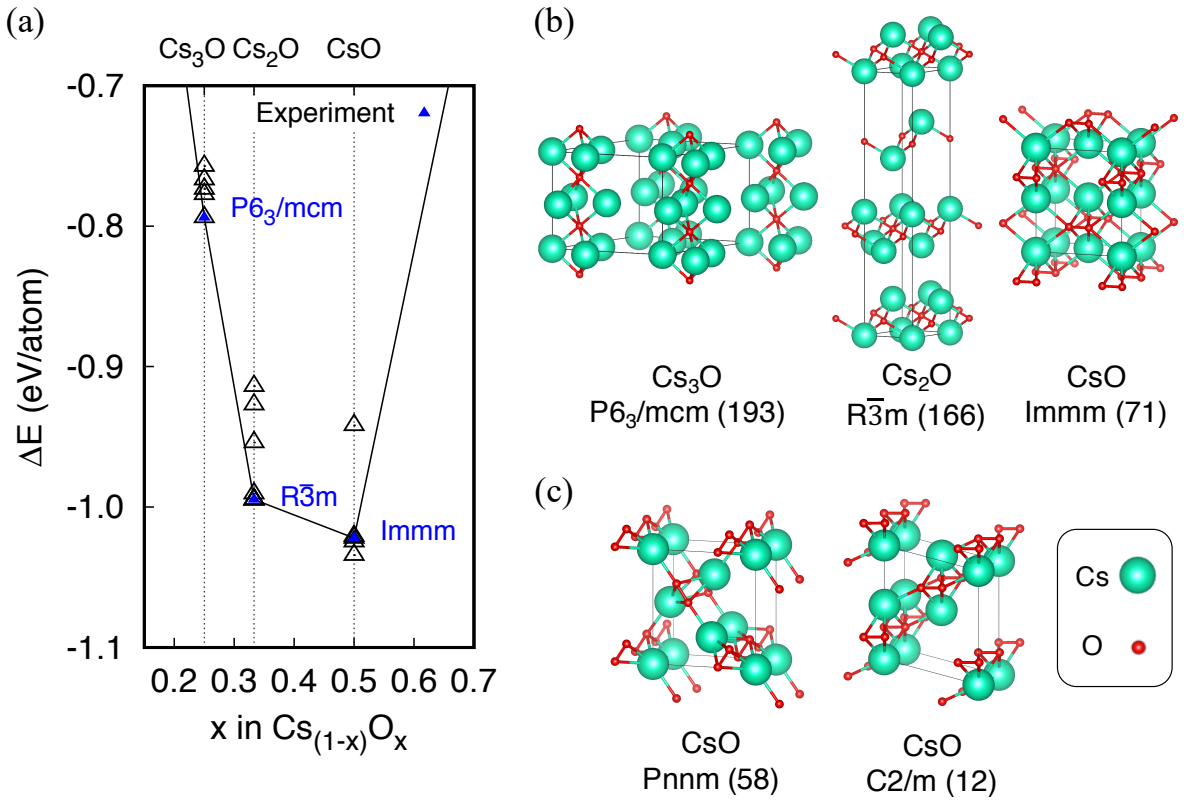


Figure 3. 1 Convex hull diagram and corresponding structures. (a) Convex hull diagram for Cs-O compounds. Each black triangle represents a structure identified through a global structure prediction, and blue triangles indicate the structures reported in the literature. (b) Atomic structures of the experimentally reported structures. (c) Atomic structures of CsO compound which show lower formation energy than the literature structure.

(meta)stable structures of CsO

Table 3.1 lists the (meta)stable structures identified through the global structure search for the chemical composition of CsO. The structure indicated in blue color (Immm #71) is the structure synthesized through experiments, and the remaining structures are not reported in literatures so far. Crystal and electronic structures of the four most stable atomic configurations are illustrated in Fig. 3.2.

Even though these structures belong to different space groups with different symmetry, they show very similar tendencies in the coordination of oxygen atoms and electronic structure. First, considering the stoichiometry, the oxygen atom needs two electrons, but there is only one Cs atom which can donate one electron. Therefore, oxygen atoms exist in the form of $[O_2]^{2-}$ rather than O^{2-}. We can see these $[O_2]^{2-}$ dimers from the crystal structures shown in Fig. 3.2. The projected band structures also confirm this. All four structures exhibit three oxygen bands (red lines) in the energy range of $-6\ eV < E-E_F < 0\ eV$, representing bonding σ, π, and anti-bonding π orbitals formed by covalent interaction between two oxygen atoms. All of these structures are semiconductors having a band gap of 1 eV ~ 2 eV.

Table 3. 1 Space group and energy values of identified structures for CsO. Blue color indicates that the structure has been reported in literature.

Composition	Space group	Energy/f.u. (eV)	ΔE (eV)
CsO	Amm2 (#38)	-7.665	-0.942
	$P2_1/c$ (#14)	-7.823	-1.021
	Immm (#71) [82]	-7.825	-1.022
	C2/m (#12)	-7.830	-1.025
	Pnnm (#58)	-7.850	-1.034

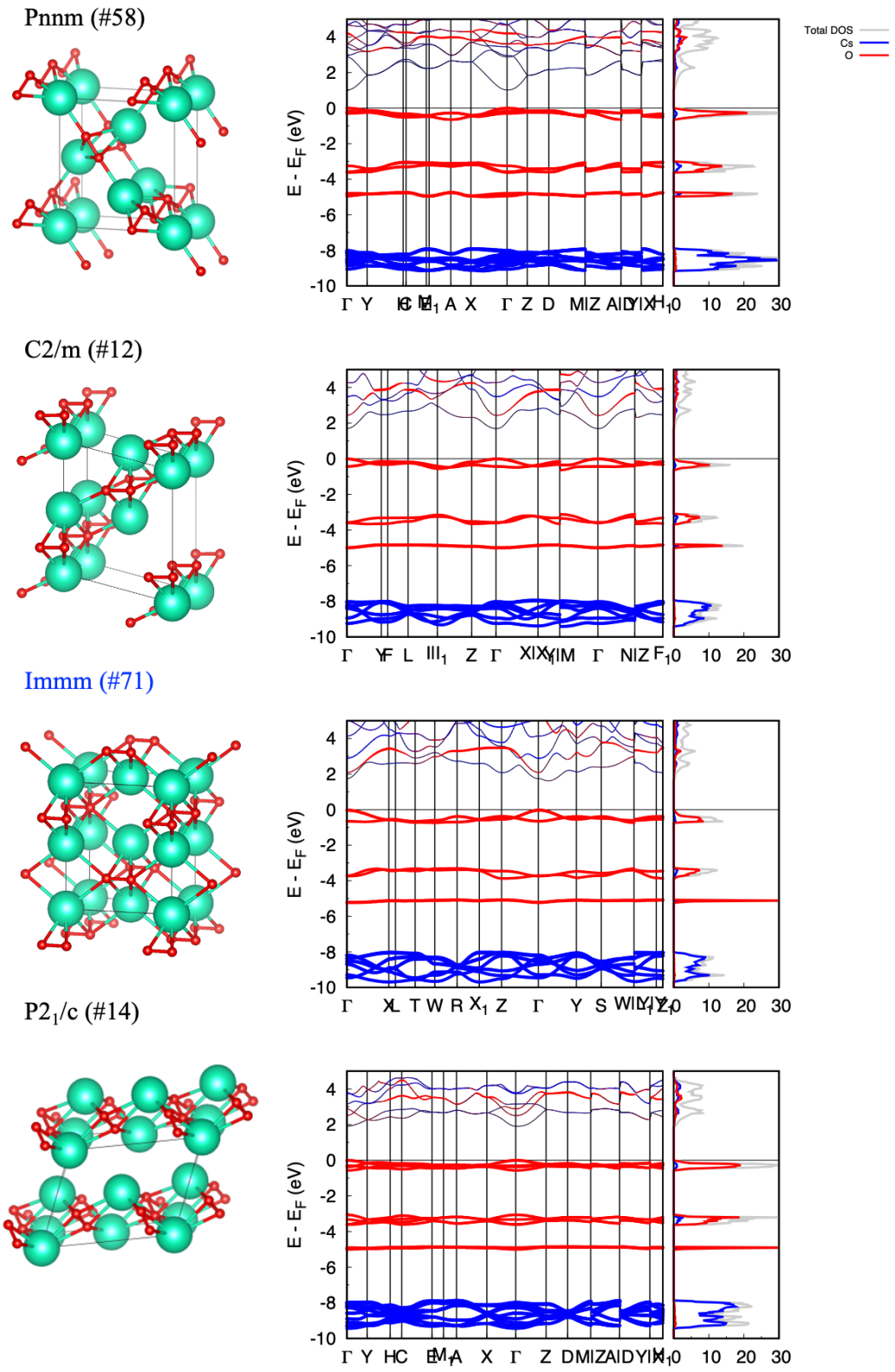


Figure 3. 2 Band structure and DOS projected on each species for (meta)stable structures of CsO.

(meta)stable structures of Cs_2O

The (meta)stable structures of Cs_2O also share similar properties coming from the stoichiometry, even though the specific atomic configurations are different from each other. The space groups to which each atomic configuration belongs, and calculated energy values are listed in Table 3.2. The structure search results confirm that the rhombohedral $R\bar{3}m$ (#166) structure, which has been synthesized, is energetically the most stable structure.

The (meta)stable structures of Cs_2O differ from the CsO structures in that the oxygen atom exists as O^{2-} ion, and as shown in Fig. 3.3, the O^{2-} ion forms an octahedral coordination geometry surrounded by six Cs atoms in all the four most stable structures. $R\bar{3}m$ (#166) and Cm (#8) structures exhibit layered structure, showing a sandwich arrangement of Cs-O-Cs in each layer. These two structures have the same atomic configuration in a single Cs-O-Cs layer, but they belong to different space groups because the stacking manner of each layer differs. This is why they show a negligible energy difference. Pmmn (#59) shows the same atomic arrangement with λ-MnO_2, which provides a framework of $LiMn_2O_4$ spinel structure. In all four structures, due to the O_h symmetry of octahedral coordination of O^{2-} ion, the p orbitals of the oxygen atom show bands that are almost degenerate in a very narrow energy region near the Fermi level (Fig. 3.3).

Table 3. 2 Space group and energy values of identified structures for Cs_2O. Blue color indicates that the structure has been reported in literature.

Composition	Space group	Energy/f.u. (eV)	ΔE (eV)
Cs_2O	Pnnm (#58)	-9.414	-0.927
	Pmmn (#59)	-9.495	-0.954
	$Fd\bar{3}m$ (#227)	-9.604	-0.991
	Cm (#8)	-9.617	-0.995
	$R\bar{3}m$ (#166) [83]	-9.617	-0.995

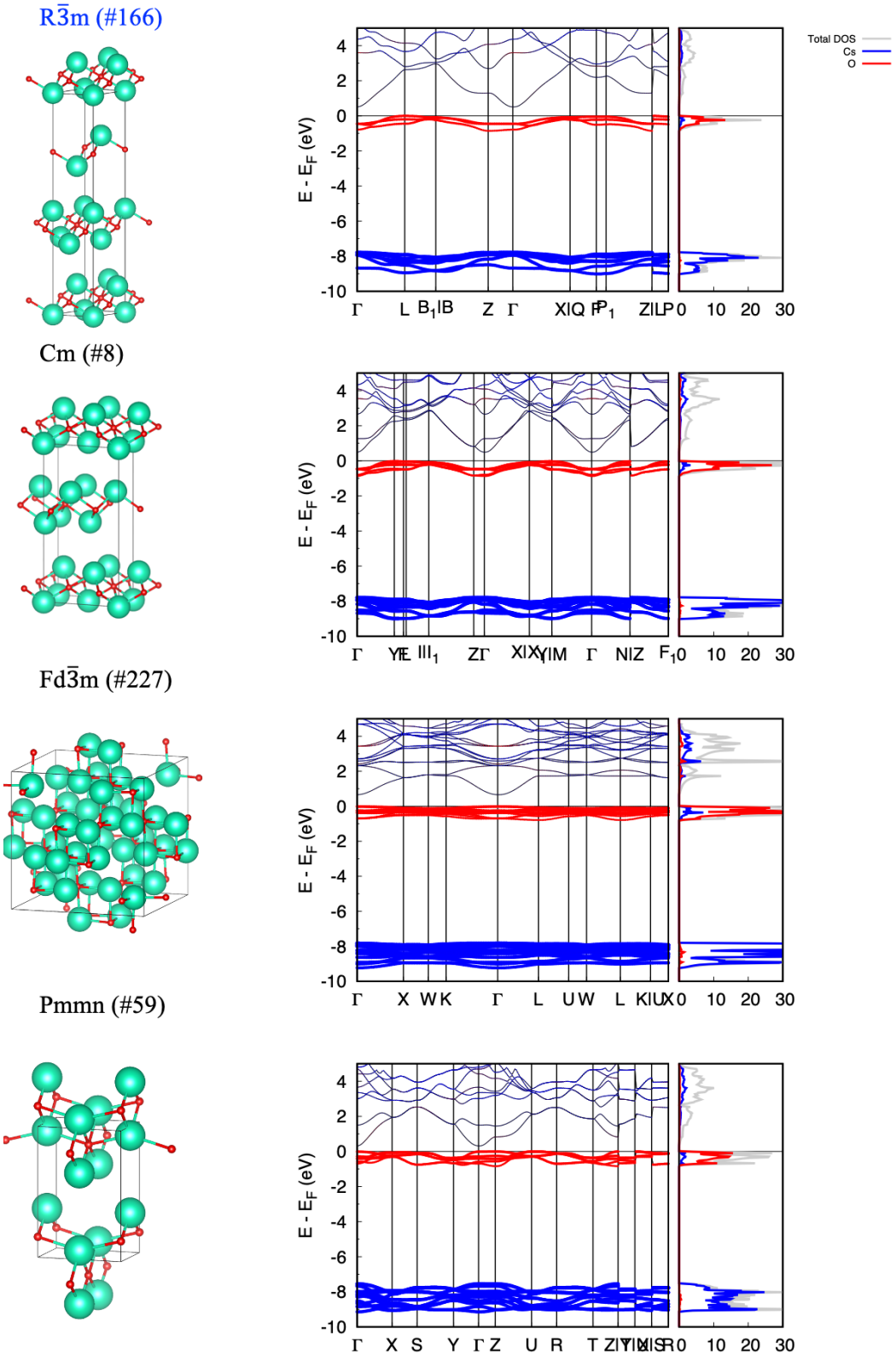


Figure 3. 3 Band structure and DOS projected on each species for (meta)stable structures of Cs_2O.

(meta)stable structures of Cs_3O

Cs_3O exhibits a peculiar phenomenon that is not seen in other chemical compositions, and all the identified (meta)stable structures listed in Table 3.3 share this property.

The most stable structure is the rhombohedral $P6_3/mcm$ (#193), and this structure was recently identified as an electride [17], which is a new class of materials where electrons are not strongly bound to any specific atom and serve as anions by occupying interstitial space. As shown in Fig. 3.4, this structure consists of 1D building blocks formed by connecting face-sharing Cs_6O octahedra along the c-axis, and anionic electrons are known to exist in the empty space between these building blocks. Interestingly, the (meta)stable structures identified through crystal structure search also exhibit the same characteristics.

The four (meta) stable structures consist of 1D or 2D building blocks and show enough space for the presence of anionic electrons. The projected band structures in Fig. 3.4, demonstrate similar characteristics showing highly dispersive metallic bands near the Fermi level. We should note that these metallic bands show contributions neither from the Cs nor O atoms. This is suggesting that these bands are associated with anionic electrons. To verify the distribution of electrons associated

Table 3. 3 Space group and energy values of identified structures for Cs_3O. Blue color indicates that the structure has been reported in literature.

Composition	Space group	Energy/f.u. (eV)	ΔE (eV)
Cs_3O	$P2_1/m$ (#11)	-10.513	-0.757
	$Pmc2_1$ (#26)	-10.552	-0.767
	$R\bar{3}$ (#148)	-10.578	-0.774
	$Cmc2_1$ (#36)	-10.593	-0.777
	$P6_3/mcm$ (#193) [84]	-10.659	-0.794

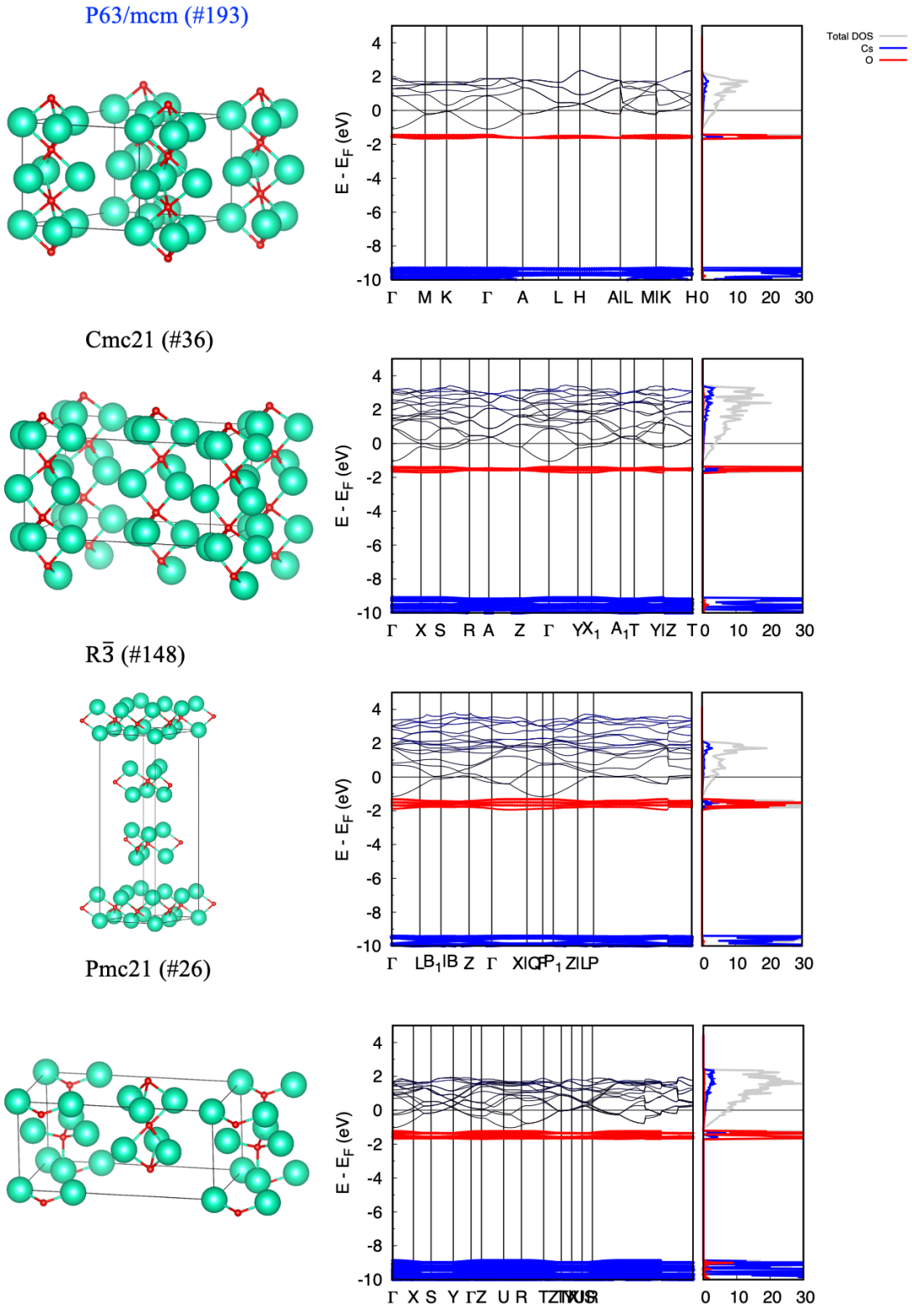


Figure 3. 4 Band structure and DOS projected on each species for (meta)stable structures of Cs_3O.

with these metallic bands, the partial charge densities in the energy range of -1.2 eV < E-E_F < 0 eV were calculated and shown in Fig. 3.5. Depending on the atomic configuration, those metallic electrons are distributed in 1D or 2D empty spaces of the lattices. In particular, in the case of $R\bar{3}$ (#148) structure, the 2D electron distribution is connected by 1D channels in the c-axis direction. The fact that $R\bar{3}$ (#148) structure, which shows a 2D layered atomic configuration, exhibits the same properties as electride indicates that the presence of anionic electrons comes from the stoichiometry of Cs_3O with one extra electron per formula unit rather than the atomic configuration.

3.3 Surface Properties

So far, the structural and electronic properties of the identified structures for Cs_xO (x = 1, 2, and 3) were explored. In this section, the surface properties such as work functions and surface energies are discussed. To scrutinize surface properties of the identified structures, slab models of various low index surface facets were constructed.

The work function (Φ) is defined as the minimum energy required to remove an electron from a specific surface of the material to the vacuum area. Therefore, it can be evaluated by subtracting the Fermi level (E_F) or the chemical potential of an electron (μ) from the vacuum level (E_{vac}), electrostatic potential energy at the vacuum area of the slab model as following.

$$\Phi = E_{\mathrm{vac}} - E_{\mathrm{F}} = -e \cdot V_{\mathrm{vac}} - \mu$$

Figure 3.6 shows the local electrostatic potential energy of the CsO Immm (#71) (001) surface slab computed from the DFT calculation as an example. The vacuum level is the electrostatic potential energy value converged in the vacuum area outside the surface.

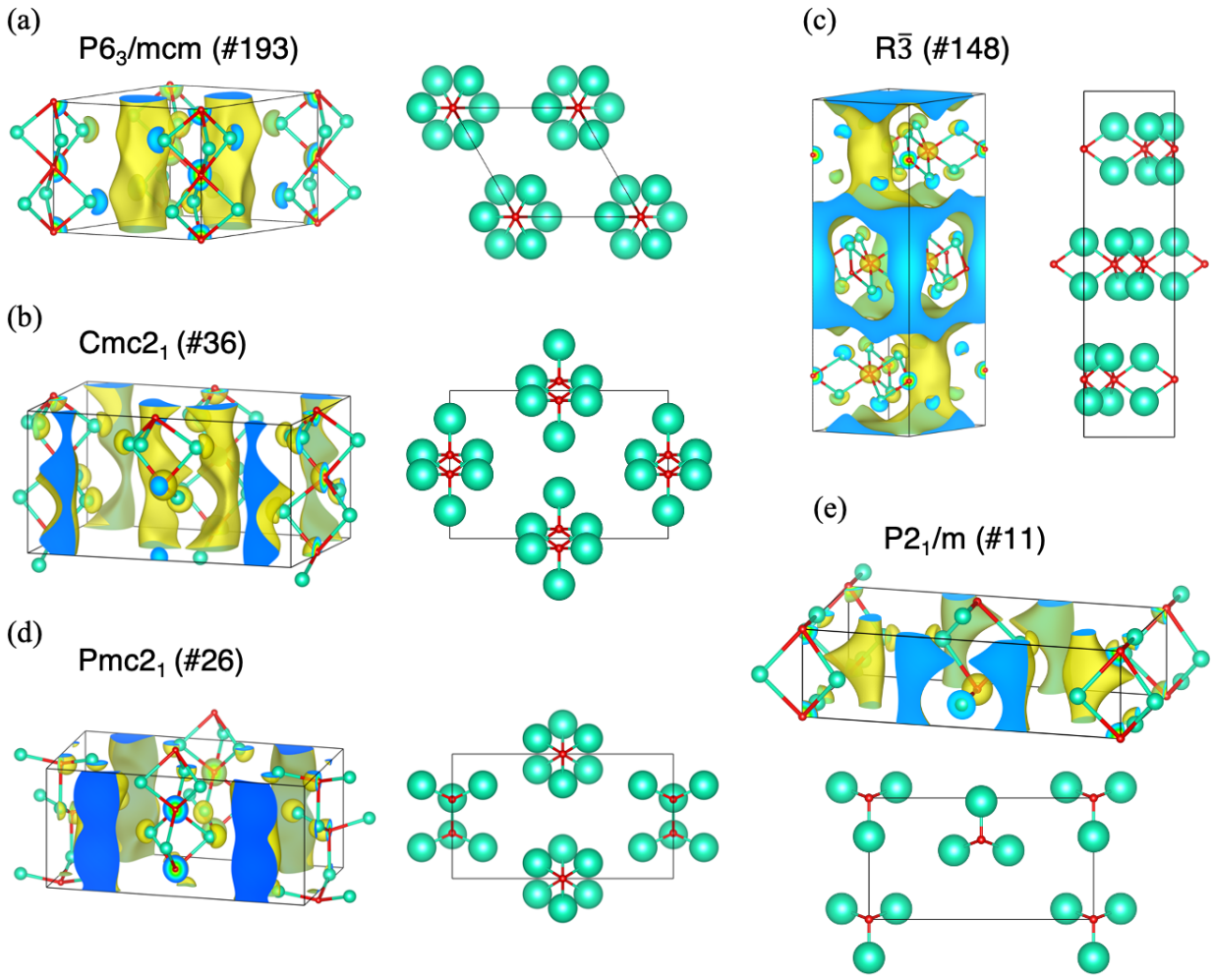


Figure 3. 5 Atomic structure and anionic electron density of (a) the most stable and (b-e) metastable structures of the Cs_3O compound. For the partial charge density of the anionic electrons, electronic bands near the Fermi level ($-1.2 < E-E_F < 0$ eV) are taken into account. Isosurfaces of the electron density is drawn to illustrate 1D or 2D anionic electron channels, and the isosurface level is chosen as the value that clearly shows an accumulation of the anionic electrons in the vacant space in the range of 0.0055 ~ 0.0065 e/Å^3.

The Fermi level is obtained through a separate calculation and also denoted in the plot as a dotted horizontal line. The distance between the two horizontal lines for E_{vac} and E_F is the work function. However, we need to be careful when using this value for the semiconductor because the value given by DFT calculation is instead the Fermi energy, which is the Fermi level at 0 K. And, because of the smearing of Fermi-Dirac distribution function, it lies slightly above the valence band maximum (VBM) and even varies depending on the applied smearing method. The Fermi level of the intrinsic semiconductor at finite temperature is known to be located right in the middle of the band gap under the assumption that the effective masses of electrons and holes are the same, which is not always true, but the variation is very small compared to the size of the band gap. Therefore, in this study, VBM + E_{gap} / 2 is regarded as the Fermi level of the semiconducting system.

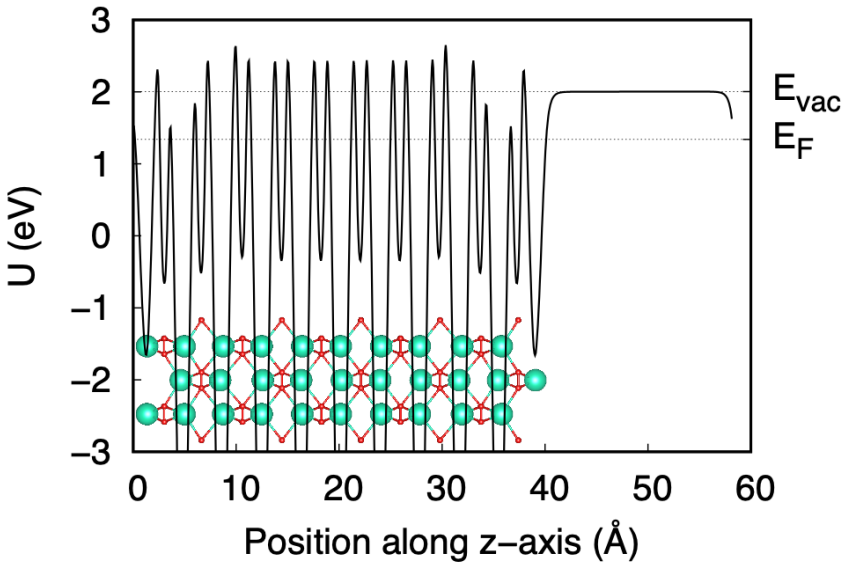


Figure 3. 6 Example of electrostatic potential energy. Atomic structure and the electrostatic potential energy along the z-direction are drawn for the Cs terminated CsO Immm (#71) (001) surface. The two horizontal dotted lines indicate the vacuum level and the Fermi level.

The surface energy (γ) is an amount of energy increased per unit area to form a surface from a bulk structure and defined as

$$\gamma = \frac{E_{\text{slab}} - N \cdot E_{\text{bulk}}}{2A},$$

where E_{slab} is the computed total energy of a surface slab relaxed on both side, E_{bulk} is the energy per formula unit of the bulk structure, N is the number of formula units contained in the surface slab, A is the area of the surface, and the 2 factor in front of A reflects the fact that top and bottom surfaces are created in the slab model. This surface energy can be used to compare the relative stability of the surfaces.

Although the above formula is a commonly used approach for calculating surface energy, one drawback of this formula is that it can be applied only to symmetric and stoichiometric slabs where the termination of both ends of the slab is the same (symmetric), and N is well defined as an integer value (stoichiometric). However, a more general method was suggested considering the cleavage energy (E_{cleavage}) and the relaxation energy ($E_{\text{relaxation}}$) as the two elements of the surface energy and applied to calculate surface energies of $PbTiO_3$ [86-88] and MoP [89]. By adopting this approach, the surface energy of specific termination can be calculated regardless of symmetry or stoichiometry of the slab using the following formulas.

$$\gamma(\alpha) = E_{\text{cleavage}}(\alpha) + E_{\text{relaxation}}(\alpha)$$

$$E_{\text{cleavage}}(\alpha) = E_{\text{cleavage}}(\beta) = \frac{[E_{\text{slab}}^{\text{unrelaxed}}(\alpha,\beta) - N \cdot E_{\text{bulk}}]}{2A}$$

$$E_{\text{relaxation}}(\alpha) = \frac{(E_{\text{slab}}^{\text{relaxed}(\alpha)} - E_{\text{slab}}^{\text{unrelaxed}}(\alpha,\beta))}{A}$$

where α and β stand for two terminations simultaneously generated by one cleavage, and stoichiometric slab with these two terminations on each end can always be formed. The cleavage energy can be estimated using this unrelaxed stoichiometric slab even though the two terminations of the slab are different because the two terminations contribute equally to the $E_{\text{cleavage,}}$ which is the reason that the cleavage energy is the same for α and β terminations. The relaxation energy for a particular termination is determined by comparing energies of the unrelaxed slab and the slab relaxed only on one side. In this study, the usual former method was exploited for symmetric and stoichiometric slabs, and the second approach was applied otherwise.

3.3.1 Work Functions and Surface Energies (x = 1, 2, and 3)

Figure 3.7 summarizes the work functions and surface energies of low index surfaces of four crystal structures for Cs, Cs_3O, Cs_2O, and CsO, and the numeric values are listed in Table 3.4. In the table, each surface is labeled by four indices, crystallographic orientation of the cleavage surface, cleavage plane, cleavage symmetry, and terminated atom(s). The cleavage plane implies that different ways of cutting with altered terminations are possible along the same direction, depending on a distance between the cleavage plane and the origin. The cleavage symmetry is denoted by 'S' or 'A', which indicates whether the bottom and top surfaces of the slab generated by the cleavage are symmetric or asymmetric. The last index, terminated atom(s), means the species of atoms located in the outermost layer of the surface. Surfaces with 'CsO' termination mean that both Cs and O appear in the outermost layer. For example, (001)-2-A-Cs surface means a surface generated by the second cleavage plane along the (001) direction, and this surface is the Cs-terminated side of an asymmetric slab, which have O-termination on the other side.

In Fig. 3.7, each circle represents the work function of a specific surface, and the color of each circle denotes its surface energy. Low index orientations considered in this study are (001), (010), (011), (100), (101), and (110). Note that most surfaces of the Cs_3O polymorphs display low surface energy values ($\gamma < 0.35$ eV/nm^2). It is because these structures are composed of 1D or 2D building blocks as super-atomic components to form crystals, where anionic electrons reside at the cavity space between the low-D building blocks.

Our work function values for BCC Cs are 1.97, 2.07, and 1.91 eV for (100), (110), and (111) surfaces, respectively, which agree well with the experimentally measured values [68,69]. The work functions show a decreasing trend as the oxygen content increases, reaching to the lowest value of 0.66 eV for the Cs-terminated (001) surface of CsO Immm (#71).

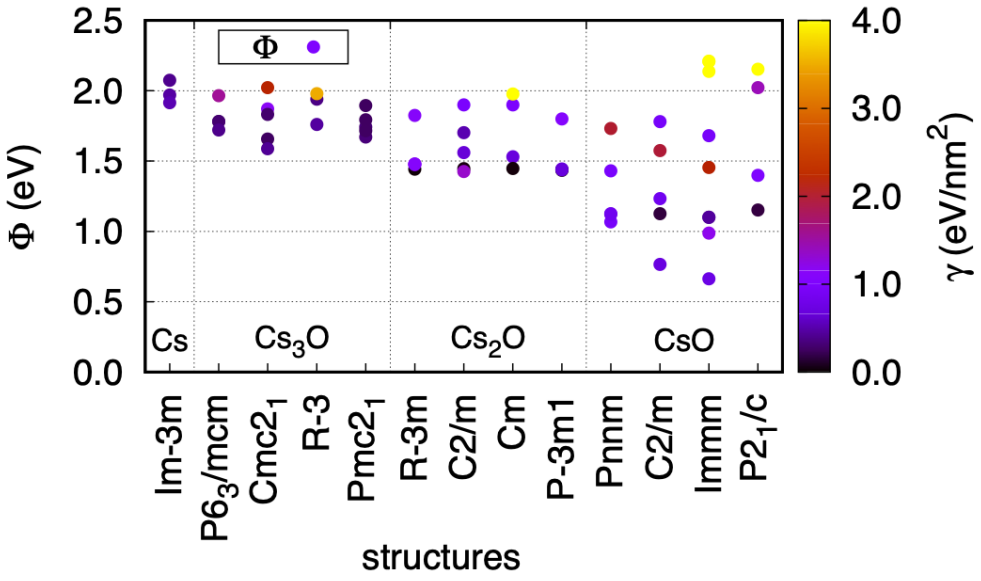


Figure 3. 7 Work functions and surface energies for all surfaces examined in this study. Each structure is represented by its space group, and each circle corresponds to a particular surface. The vertical dotted line distinguishes different chemical compositions.

Table 3. 4 Surface energies ($\boldsymbol{\gamma}$) and work functions ($\boldsymbol{\Phi}$) of cesium oxide compounds with different orientation, cleavage plane, and terminations.

Composition	Space group	Surface	γ (eV/nm^2)	Φ (eV)
Cs	$Im\bar{3}m$ (#229)	(100)-1-S-Cs	0.441	1.969
		(110-1-S-Cs	0.375	2.075
		(111)-1-S-Cs	0.496	1.915
Cs_3O	$P6_3/mcm$ (#193)	(100)-1-S-Cs	0.292	1.782
		(010)-1-S-Cs	0.292	1.780
		(001)-1-A-Cs	1.595	1.964
		(001)-1-A-O	0.856	2.908
		(110)-1-S-Cs	0.367	1.720
	$Cmc2_1$ (#36)	(010)-1-S-Cs	0.250	1.656
		(001)-1-A-Cs	1.166	1.871
		(001)-1-A-O	0.398	1.587
		(001)-2-A-Cs	2.092	2.022
		(001)-2-A-O	0.294	2.519
		(110)-1-S-Cs	0.282	1.832
	$R\bar{3}$ (#148)	(100)-1-S-CsO	0.428	1.760
		(001)-1-S-Cs	0.346	1.940
		(110)-1-S-Cs	3.499	1.980
	$Pmc2_1$ (#26)	(010)-1-A-Cs1	0.312	1.742
		(010)-1-A-Cs2	0.315	1.671
		(001)-1-A-Cs1	0.250	1.794
		(001)-1-A-Cs2	0.245	1.894
		(011)-1-S-Cs	0.250	1.717
Cs_2O	$R\bar{3}m$ (#166)	(100)-1-S-CsO	1.096	1.477
		(010)-1-S-CsO	1.095	1.480
		(001)-1-S-Cs	0.016	1.443
		(110)-1-S-CsO	1.106	1.825
	C2/m (#12)	(100)-1-S-CsO	0.937	1.901
		(010)-1-S-Cs	0.645	1.560
		(001)-1-S-Cs	0.039	1.446
		(011)-1-S-Cs	1.412	1.426
		(0-11)-1-S-Cs	0.488	1.701
	Cm (#8)	(100)-1-S-CsO	0.950	1.899
		(010)-1-S-Cs	0.669	1.530
		(010)-2-A-Cs	4.579	1.976
		(001)-1-S-Cs	0.024	1.447
	$P\bar{3}m1$ (#164)	(100)-1-S-Cs	0.666	1.440
		(010)-1-S-Cs	0.667	1.444
		(001)-1-S-Cs	0.040	1.434
		(110)-1-S-CsO	1.082	1.798

Table 3.4 (Continued)

Composition	Space group	Surface	γ (eV/nm^2)	Φ (eV)
CsO	Pnnm (#58)	(100)-1-S-CsO	1.885	1.732
		(010)-1-S-Cs	0.878	1.068
		(001)-1-S-Cs	0.922	1.431
		(011)-1-S-Cs	0.776	1.122
	C2/m (#12)	(100)-1-S-CsO	1.863	1.575
		(010)-1-S-O	0.873	1.780
		(001)-1-S-Cs	0.681	0.766
		(011)-1-S-Cs	0.780	1.232
		(0-11)-1-S-Cs	0.156	1.127
	Immm (#71)	(100)-1-S-CsO	2.027	1.454
		(010)-1-S-O	0.879	1.680
		(010)-2-A-Cs	6.403	1.248
		(010)-2-A-O	3.761	6.159
		(001)-1-S-Cs	0.708	0.663
		(001)-2-A-Cs	5.733	2.210
		(001)-2-A-O	3.939	5.112
		(110)-1-S-O	3.114	3.090
		(110)-2-A-Cs	5.385	2.138
		(110)-2-A-O	3.566	5.023
		(101)-1-S-Cs	1.241	0.988
		(101)-2-A-Cs	4.883	2.207
		(101)-2-A-O	3.020	3.206
		(011)-1-S-Cs	0.419	1.100
		(011)-2-S-O	4.517	3.305
		(011)-3-A-Cs	6.610	2.090
		(011)-3-A-O	2.745	3.699
	$P2_1/c$ (#14)	(100)-1-S-Cs	2.828	2.971
		(010)-1-S-Cs	0.165	1.153
		(001)-1-A-Cs	5.166	2.153
		(001)-1-A-O	3.411	4.321
		(011)-1-S-Cs	1.484	2.022
		(0-11)-1-S-Cs	0.989	1.398

Our results are in excellent agreement with the experimental measurement [77,78] showing continuous changes in the work function of Cs films as oxidation progresses by increasing oxygen exposure. Although experiments were unable to elucidate the relationship between work function and the degree of oxidation levels, it was shown that the work function can reach as low as ~ 0.7 eV with an increased oxygen exposure [77]. Further experiment identified that the chemical composition corresponding to the lowest work function is CsO [78].

3.3.2 CsO Immm (#71): The Lowest Work Function Structure

Next, the energetics and thermodynamic stabilities of the lowest work function material, CsO Immm (#71) structure is discussed. Figure 3.8 shows its surface energies and work functions for a given surface orientation and atomic termination, where all the possible 17 surfaces of low Miller index facets were taken into account.

Figure 3.8 shows substantial variations in the surface energies (~ 6 eV/nm^2) and the work functions (~ 6 eV) depending on the direction and termination of the surface, which is stemmed from various origins, such as ionic relaxation, charge redistribution [90], and the formation of electric dipoles inside asymmetric slabs [91]. Since these factors are sensitively affected by the nature of broken chemical bonding and ionic configuration of each surface termination, it requires a complicated procedure to estimate each influence independently. For example, a slab with an asymmetric termination, Cs- and O-terminations on each side, accumulates a net electric dipole moment pointing from O-terminated surface to Cs-terminated one, resulting in a higher electrostatic potential in the direction of the O-terminated surface, consequently an increased work function.

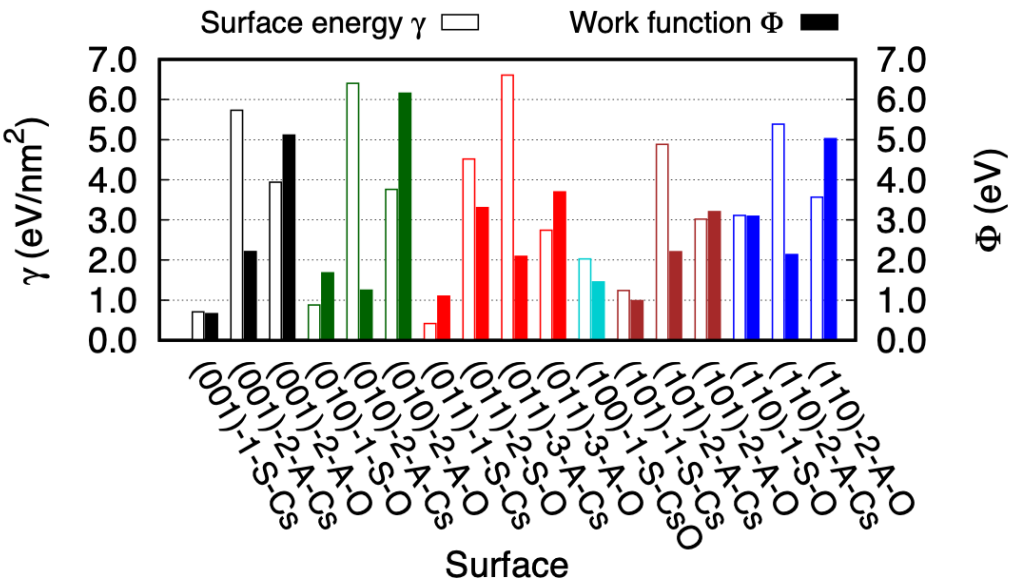


Figure 3. 8 Work functions and surface energies of 17 different surfaces of the CsO Immm (#71) structure. Each surface identified by four indices as described in the text. A different color is used to indicate each different surface orientation.

Moreover, spill out of surface electrons to the vacuum induces surface dipole barrier that is responsible for an increased work function. A higher spill out electron density of anions than that of cations [92] contributes to the relatively low work function of Cs-terminated surfaces than O-terminated ones. Consequently, for a given surface orientation, Cs-terminated surfaces show relatively smaller work functions than O-terminated surfaces. For all surface orientations except (100) where the symmetric Cs and O termination is the only possibility, the lowest work function surfaces are terminated with Cs and show the work functions of 0.66, 1.25, 1.10, 0.99, and 2.14 eV for (001), (010), (011), (101), and (110) directions. The surfaces with the lowest work function for the (001), (011), and (101) directions are also the most stable surfaces with the lowest surface energy for each direction.

Next, thermodynamic stabilities of the CsO surfaces for a given experimental condition, temperature (T) and pressure (P), are investigated. The relative thermodynamic stabilities of different surfaces can be determined by comparing surface free energies $\gamma(T,P)$ [89,93]. This quantity is defined as

$$\gamma(T,p)=\left[E_{\text{slab}}-N_{\text{Cs}}\cdot\mu_{Cs}(T,P)-N_{\text{O}}\cdot\mu_{\text{O}}(T,P)\right]/2A,$$

where μ_{Cs} and μ_O are the chemical potentials of Cs and O, N_{Cs} and N_O are the numbers of Cs and O atoms contained in the slab, respectively. Here, E_{slab} is DFT total energy of a slab neglecting vibrational entropy and volume changes for a given temperature. This approximation is commonly applied to calculate the surface free energy due to their negligible contributions [93].

If we limit our discussion to the chemical composition of CsO, and assume the thermodynamic equilibrium between the surface and the bulk material which is acting as a thermodynamic reservoir, the equilibrium condition for chemical potential is

$$\mu_{Cs}(T,P)+\mu_{\text{O}}(T,P)=E_{\text{bulk}}^{\text{CsO}}.$$

This equation implies that the sum of the chemical potentials of Cs and O is equal to the Gibbs free energy per formula unit of bulk material, and again the Gibbs free energy is replaced by DFT total energy. Using the above two equations, $\gamma(T,P)$ can be expressed as a function of a single variable $\mu_O(T,P)$ as follow.

$$\gamma(T,p)=\frac{1}{2A}\left[E_{\text{slab}}-N_{\text{Cs}}E_{\text{bulk}}^{\text{CsO}}+(N_{\text{Cs}}-N_{\text{O}})\mu_{\text{O}}(T,P)\right]$$

The slope of $\gamma(T,P)$ is determined by $(N_{Cs} - N_O)/2A$, the degree of off-stoichiometry per unit area, thus it becomes zero for stoichiometric slabs, and only the asymmetric cleavage shows non-zero slope because of extra atoms added to construct a symmetric slab.

Now, we need to specify appropriate limits for μ_O in which the thermodynamic equilibrium between the surface slab and the environment can be maintained. The chemical potential of each element cannot exceed that of the most stable elemental phase [94]. Otherwise, the thermodynamic equilibrium condition is broken, and the most stable elemental phase starts to form on the surface. For Cs and O, BCC bulk and free-standing O_2 molecule can be considered as the most stable elemental phases, and the upper limit for chemical potentials are

$$\mu_{\mathrm{Cs}} < E_{\mathrm{BCC}}^{\mathrm{Cs}}, \text{ and } \mu_{\mathrm{O}} < \frac{1}{2} E_{\mathrm{molecule}}^{\mathrm{O_2}}.$$

The lower limit for μ_0 can be determined by taking into account the equilibrium condition for chemical potentials and the upper limit of μ_{Cs}, and consequently, appropriate range for μ_0 is

$$E_{\mathrm{bulk}}^{\mathrm{CsO}} - E_{\mathrm{BCC}}^{\mathrm{Cs}} < \mu_{\mathrm{O}} < \frac{1}{2}\mu_{\mathrm{O_2}}^{\mathrm{molecule}}, \text{ or } E_{\mathrm{bulk}}^{\mathrm{CsO}} - E_{\mathrm{BCC}}^{\mathrm{Cs}} - \frac{1}{2}\mu_{\mathrm{O_2}}^{\mathrm{molecule}} < \mu_{\mathrm{O}} - \frac{1}{2}\mu_{\mathrm{O_2}}^{\mathrm{molecule}} < 0.$$

The left side is the formation energy per formula unit of CsO ($\Delta E^{\mathrm{f.u.}}$), and if we define $\Delta\mu_O$ as $\mu_O - 1/2 \cdot \mu_{O_2}^{\mathrm{molecule}}$, the limits for $\Delta\mu_O$ becomes

$$\Delta E^{\mathrm{f.u.}} < \Delta\mu_{\mathrm{O}} < 0.$$

The calculated $\Delta E^{\mathrm{f.u.}}$ for the CsO Immm (#71) structure is -2.04 eV, so the range of $\Delta\mu_O$ is -2.04 eV (O-poor condition) < $\Delta\mu_O$< 0 eV (O-rich condition).

Figure 3.9 presents surface free energies as a function of oxygen chemical potential, where the work function of a given surface is also listed in the parentheses. For most regions of oxygen chemical potential, the surface free energy of the (001)-1-S-Cs surface (solid black line) exhibiting the lowest work function of 0.66 eV lies below that of other surfaces oriented in the same direction (other two black lines). The other low work function surfaces, (101)-1-S-Cs (solid brown line, 0.99 eV) and (011)-1-Cs (solid red line, 1.10 eV), are also mostly stable except for the extremely O-rich condition.

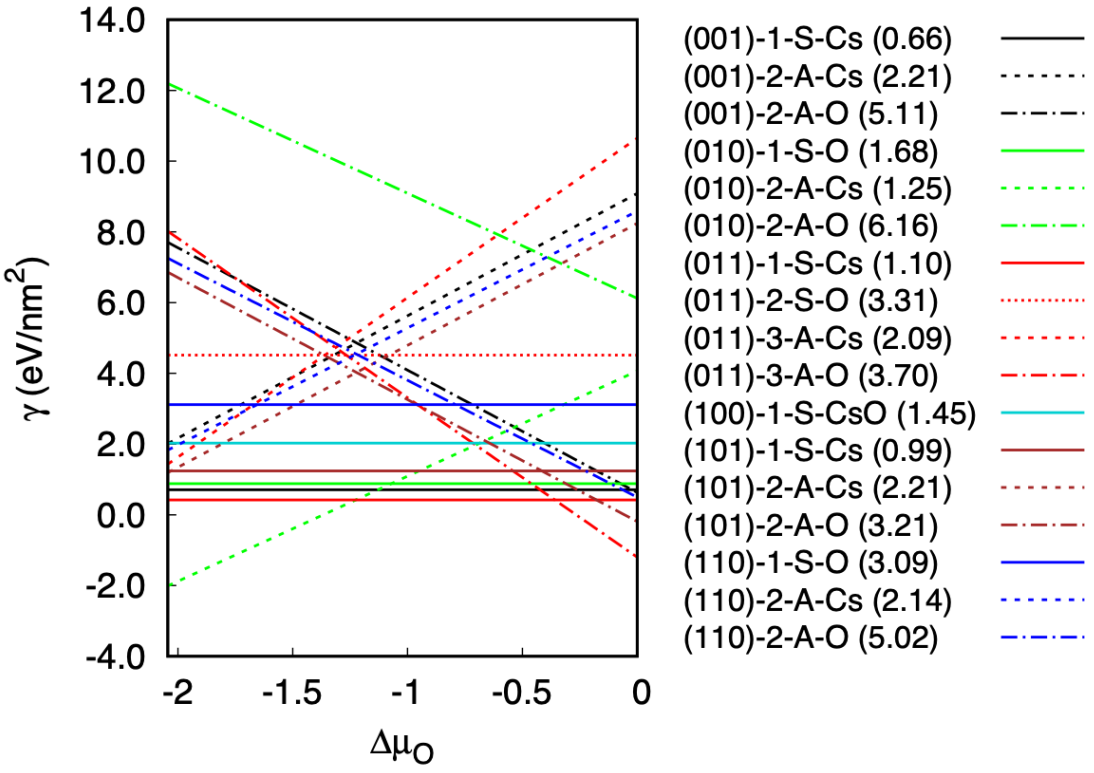


Figure 3. 9 surface free energy of 17 different surfaces of the CsO Immm (#71) structure as a function of oxygen chemical potential. The work function is also given by a numeric value inside the parentheses in the legend.

3.4 Changes in Work Functions due to Adatom Adsorption

Finally, changes in work functions by adding adsorbate atoms on the surfaces will be discussed. Specifically, I focus on the experimentally confirmed crystal structures of each chemical composition (Cs_3O $P6_3/mcm$, Cs_2O $R\bar{3}m$, and CsO Immm), and the surfaces which show the lowest surface energy or lowest work function for each atomic structure were studied. Figure 3.10 presents the selected surfaces for the investigation of work function changes.

3.4.1 Surface Dipole Moment Density and Work Function

An adsorbate can change the work function, and this phenomenon is directly connected to the changes in the surface dipole moment induced by the redistribution of charge density [79-81]. The reason for this is that the electric field induced by the dipole moment changes the potential energy barrier required for electrons to escape the material. The relationship between the changes in surface dipole moment and work function can be written as

$$\Delta\Phi = -\frac{e}{\varepsilon_0}\Delta p,$$

where Φ is the work function, e is the electron charge, ε_0 is the permittivity, and p is the dipole moment density. A positive dipole moment means that the dipole is pointing out of the surface. According to the equation, an increase in the surface dipole moment lowers the work function, whereas a decrease in the surface dipole moment increases the work function. If we consider the fact that the redistribution of charge density is caused by two factors: a structural deformation of the surface due to the presence of the adsorbate and the charge transfer between the surface and the adsorbate, the above equation can be expressed as follows.

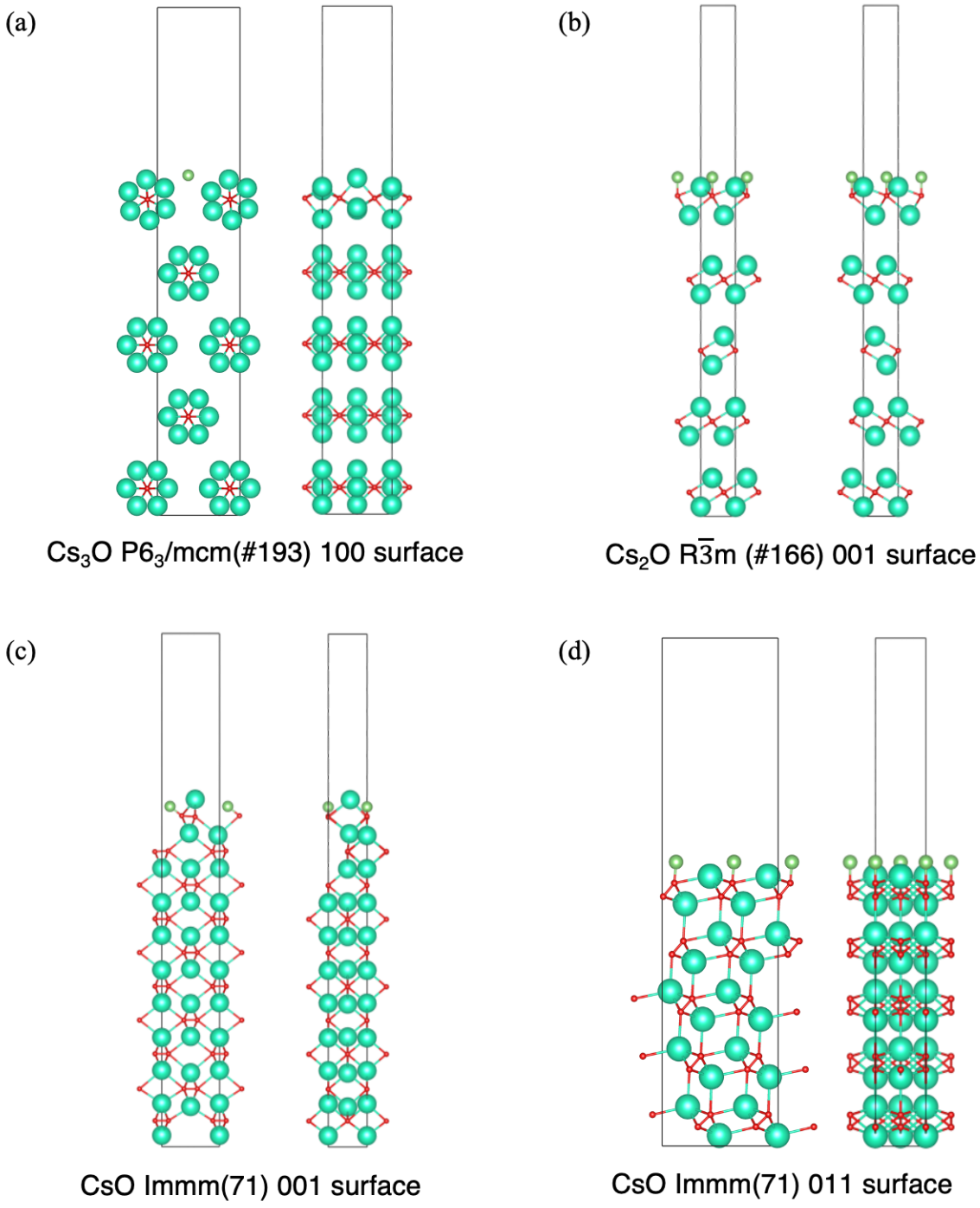


Figure 3. 10 Atomic structures of surface slabs with Li adsorbate. (a) Cs_3O $P6_3/mcm$ (100) surface. (b) Cs_2O $R\bar{3}m$ (001) surface. (c) CsO Immm (011) surface. (d) CsO Immm (001) surface. Upper 1/5 part of the slab with the adsorbate atom is fully relaxed.

$$\Delta\Phi = \Delta\Phi_1 + \Delta\Phi_2 = -\frac{e}{\varepsilon_0}(\Delta p_1 + \Delta p_2)$$

Δp_1 is the surface dipole moment density produced by the deformation of the substrate, and Δp_2 is the surface dipole moment density induced by the charge transfer. The dipole moment change due to the charge transfer is a major factor in work function change unless significant reconstruction of the surface takes place.

The general rule for metal substrates is that the direction of charge transfer is determined by the difference in electronegativity between the adsorbates and substrates. Adsorbates with low electronegativity (i.e., electropositive adatom) are expected to lower the work function because the charge transfer from the adatom to the surface takes place, resulting in negative surface dipole moment. However, it has been shown that this general rule does not always predict the correct work function change, because even though charge transfer occurs in the same direction, induced surface dipoles can be formed in different directions due to detailed differences in charge redistribution [79]. Also, in the case of the ionic compounds, the redistribution of the charge density can be further complicated according to the underlying atomic structure of the surface and chemical bonds between the substrate and the adsorbate. Therefore, numerical computations are required to accurately estimate the magnitude and direction of surface dipole caused by adsorbates.

3.4.2 Work Function Changes

Calculated work function changes of four different surfaces due to various adsorbates are listed in Table 3.5 and plotted in Fig. 3.11. In most cases, work functions tend to increase with adsorbates, even for alkali metals with low electronegativity. Cs_3O 100 surface is the only one with lowered work function upon the adsorption of highly electronegative atoms such as N, S, F, and Cl, where

Table 3. 5 Changes in work functions upon the adsorption of atomic adsorbates on various surfaces. The unit of work function is eV. Negative work function changes are indicated by red color.

Adsorbate	Cs_3O (100)		Cs_2O (001)		CsO (001)		CsO (011)	
	Φ	ΔΦ	Φ	ΔΦ	Φ	ΔΦ	Φ	ΔΦ
pristine	1.783	0.000	1.443	0.000	0.662	0.000	1.101	0.000
Li	2.335	0.552	3.573	2.131	2.434	1.771	3.426	2.325
Na	2.147	0.364	2.842	1.399	2.589	1.926	3.161	2.060
K	2.154	0.371	2.420	0.978	2.174	1.511	2.474	1.373
Rb	2.096	0.313	2.219	0.776	2.224	1.561	2.313	1.212
Cs	1.961	0.178	2.127	0.684	2.247	1.584	2.096	0.995
Mg	2.201	0.418	2.998	1.556	2.826	2.163	4.051	2.950
Al	2.214	0.430	3.358	1.916	2.439	1.776	5.199	4.098
Si	2.410	0.627	4.680	3.237	2.399	1.736	3.221	2.120
N	1.500	-0.283	6.000	4.557	2.529	1.866	3.397	2.296
P	2.422	0.639	6.053	4.610	1.072	0.409	4.281	3.180
O	1.560	-0.223	3.576	2.133	1.466	0.803	2.423	1.322
S	2.332	0.549	7.366	5.923	2.416	1.753	4.121	3.020
F	1.379	-0.404	6.138	4.696	2.745	2.082	3.369	2.268
Cl	1.351	-0.432	8.524	7.081	3.915	3.252	6.125	5.025

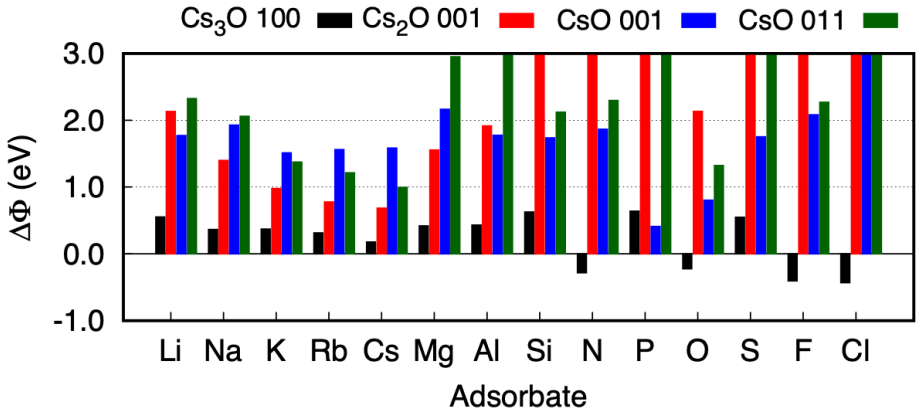


Figure 3. 11 Changes in work functions upon the adsorption of atomic adsorbates on various surfaces.

the work function can be lowered as much as 0.43eV. This result is very interesting because, according to the general rule, electronegative atoms are known to increase the work function. These results indicate that the change in work function is influenced not only by charge transfer between the adsorbate and Cs atoms located on the outermost surface but also by other factors. I will discuss the atomic origins of those changes in work functions in detail.

Increasing cases

As mentioned earlier, electropositive adsorbates can be expected to lower the work function due to the charge transfer from the adatom to the outermost layer of the surface. However, in the case of Cs-terminated surfaces, which show low work functions, the charge transfer usually occurs from Cs atoms in the outermost layer to the adatom because the Cs have lower electronegative than any other element. This is the first reason for the increase in work function in most cases. Secondly, in some cases, surface deformation caused by adsorbate also leads to an increase in work function. This phenomenon can be explained by taking the CsO Immm (#71) (011) surface as an example. Figure 3.12 shows relaxed atomic structures with various adatoms. In the case of most metal adsorbates (Li, Na, K, Rb, Cs, Mg, Ag, Au), the structure of the CsO (001) surface does not change significantly, but in other cases, the surface structure is notably deformed.

This difference implies that the increase in work functions of these surfaces is resulted by other factors. Table 3.6 shows contributions of the structural deformation and the charge redistribution to the total work function change in the cases of Li, Na, Al, P, and Cl. As mentioned earlier, in the case of Li and Na, the structure is almost unchanged, so $\Delta\Phi_1$ has a small value, and the total work function change is mostly determined by $\Delta\Phi_2$. However, in the case of Al and P, the degree of structural deformation is significant so that the value of $\Delta\Phi_1$ is substantial.

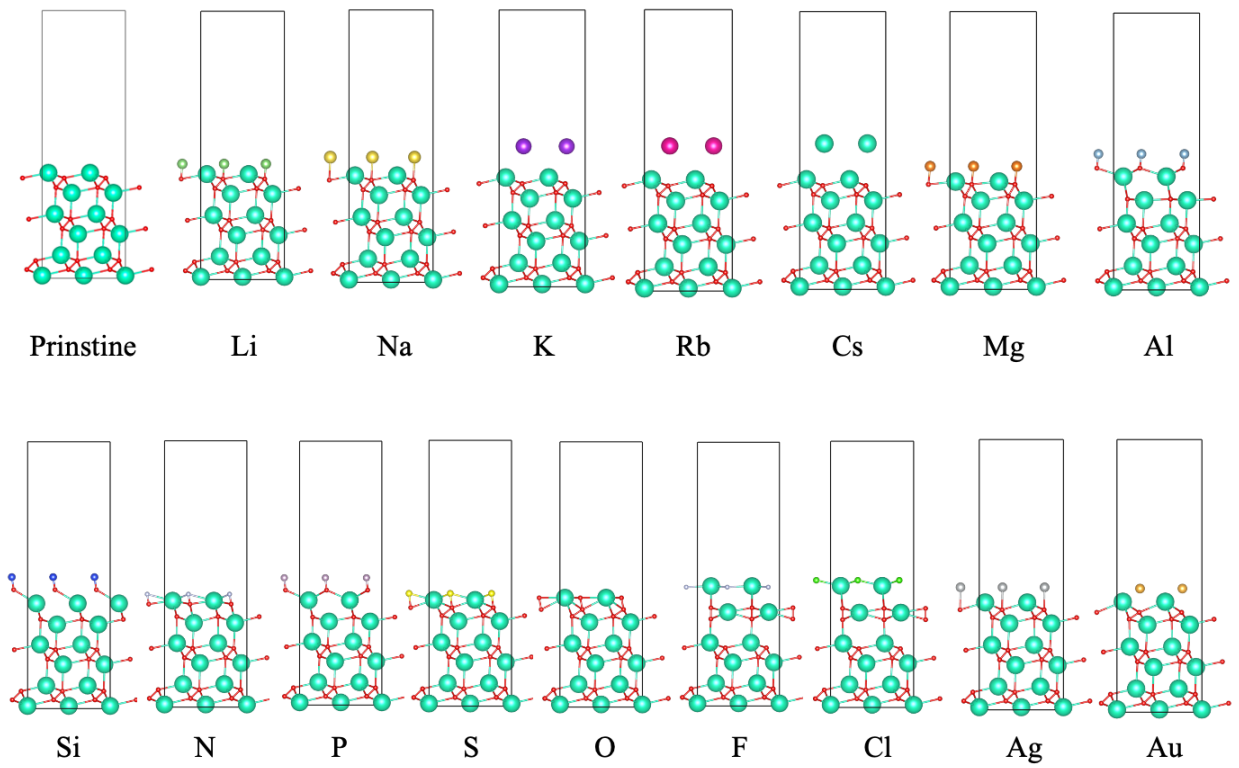


Figure 3. 12 Relaxed structure of CsO Immm (#71) 011 surface with various adatoms.

Table 3. 6 Work function changes of CsO (011) surface due to the structural deformation ($\boldsymbol{\Delta\Phi_1}$) and the charge transfer ($\boldsymbol{\Delta\Phi_2}$).

Adsorbate	$\Delta\Phi_1$ (eV)	$\Delta\Phi_2$ (eV)	$\Delta\Phi_{total}$ (eV)
Li	0.185	2.140	2.325
Na	0.374	1.686	2.060
Al	5.346	-1.248	4.098
P	5.751	-2.571	3.180
Cl	1.220	3.805	5.025

The contribution of $\Delta\Phi_1$ is not negligible also in the case of Cl. Figure 3.13 shows changes in the charge distribution and resulting surface dipole moment density (Δp_2) in the case of Na, Al, and Cl adsorbate. Na is an atom with low electronegativity, but it is higher than that of Cs. Hence the charge transfer from the nearby Cs atom to the Na atom occurs, resulting in a negative surface dipole moment, which lead to an increase of work function ($\Delta\Phi_2$). All alkali metal atoms show the same tendency. In the case of Al, the direction in which charge transfer occurs is quite different. Oxygen atoms come out of the Cs layer, and charge transfer from Al atoms to O atoms occurs through ionic bonding.

This charge transfer is in the opposite direction to that of Na, and therefore the work function ($\Delta\Phi_2$) is lowered through the positive surface dipole moment. However, the negative surface dipole moment induced by the structure deformation, where negative oxygen ions move out of the surface, is more significant, and the total work function increases. Finally, in the case of the electronegative Cl atom, the electrons inside the substrate move toward the Cl atoms to form a negative surface dipole moment, thereby increasing the work function together with the structural deformation.

Decreasing cases

Cs_3O ($P6_3/mcm$ #193) (100) surface is the only surface that shows a decrease in work function. This happens when highly electronegative atoms such as N, S, F, and Cl are adsorbed on the surface. In the case of the Cl adatom, the work function can be lowered by 0.43eV from 1.782 eV to 1.351 eV. This phenomenon is attributed to the fact that Cs_3O is an electride containing anionic electrons in a hollow space.

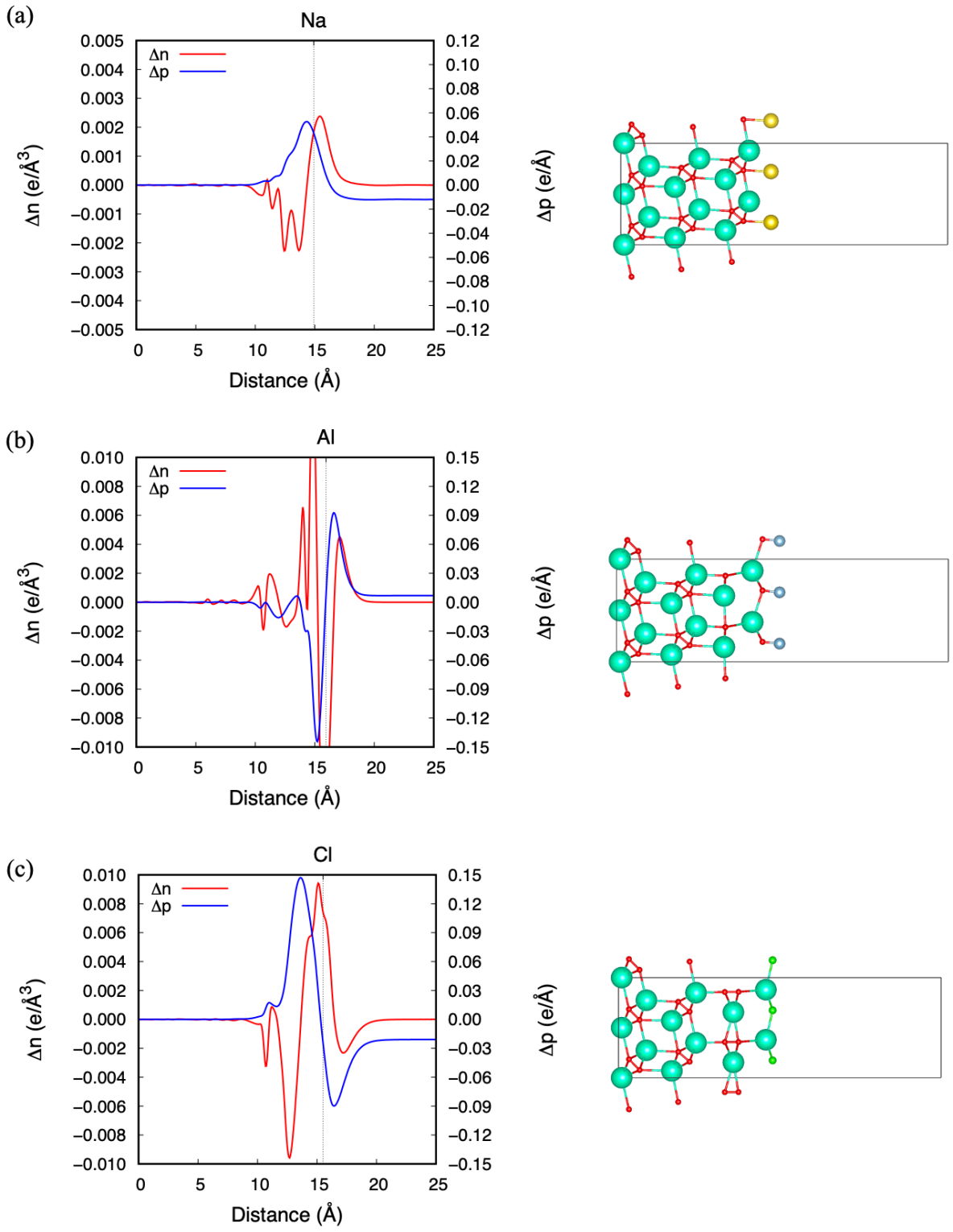


Figure 3. 13 Change of the surface charge distribution and resulting surface dipole moment density of CsO (011) surface induced by (a) Na, (b) Al, and (c) Cl.

Figure 3.14 (a) shows a fully relaxed atomic structure of the Cl-adsorbed Cs_3O (100) surface. Cs_3O contains anionic electrons at the cavity space between the 1D building blocks as shown in Fig. 3.14 (b), which illustrates the partial charge density near the Fermi level. The regions indicated with cyan color are where the anionic electrons reside. As shown in Figure 3.14, the empty space between 1D building blocks on the outermost surface allows the Cl atom to penetrate into the surface, and this adatom absorbs the anionic electrons distributed in this void space. This is why the anionic electron density in the vicinity of the Cl atom at the top of the slab is significantly smaller than that of the bottom as shown in Fig. 3.14 (b). Figure 3.14 (c) is the differential charge density showing how the anionic electron density distributed near the Fermi level changes by adsorption of the Cl atom. The green regions clearly show a decrease in the anionic electron density due to the Cl adsorption. Figure 3.14 (d), which shows the changes in total electron density, also evidently indicates that charge transfer occurs from the region of anionic electrons (blue) to the vicinity of the Cl atom (green and red). The projected band structures and DOS of this surface shown in Fig.3.15 also provide the evidence for this charge transfer. First, comparing two DOS with and without Cl adsorbate, it can be seen that s ($-16\ eV < E-E_F < -15\ eV$) and p ($-4\ eV < E-E_F < -3\ eV$) orbitals of Cl atom are fully occupied. The projected band structure also shows that three p orbital bands of Cl atom are occupied, which implies that one of the anionic electrons near the Fermi level is transferred to the Cl atom. Bader charge analysis (Fig. 3.16) was also performed to check the amounts of electrons assigned to the Cl adsorbate, and it also demonstrates that there is an increase of 0.896 electrons on Cl site.

So far, the charge transfer where the anionic electron is absorbed into the Cl atom penetrating deep into the surface was discussed. It is this charge transfer that induces the positive surface dipole moment and finally leads to a decrease in work function.

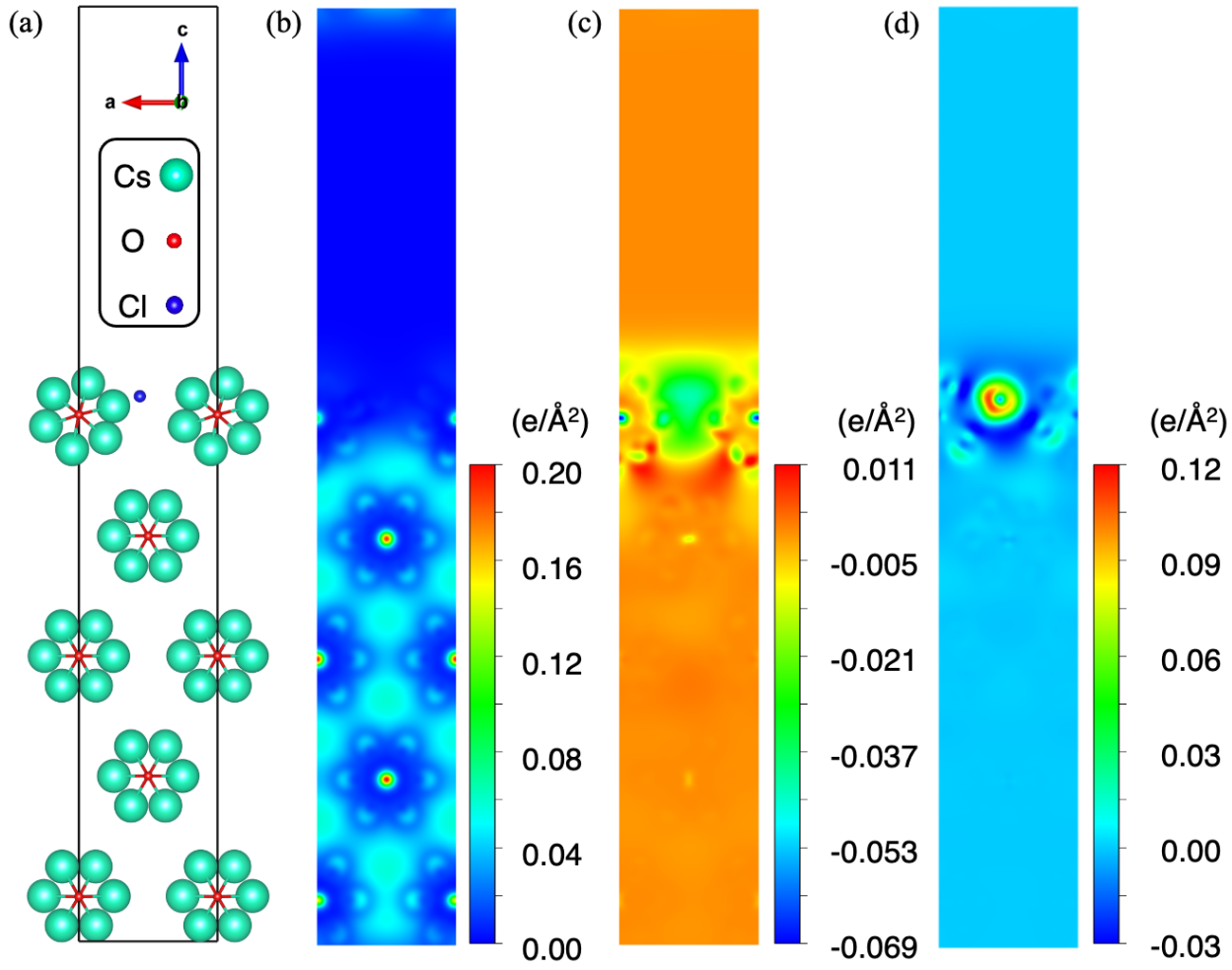


Figure 3. 14 Atomic structure and electron densities of Cl-adsorbed Cs_3O (100) surface. (a) Fully relaxed atomic structure. (b) The partial charge density of anionic electrons calculated from the anionic electron bands near the Fermi level. (c) Change of anionic electron density upon the adsorption of the Cl on the surface. (d) Change of total electron density upon Cl adsorption.

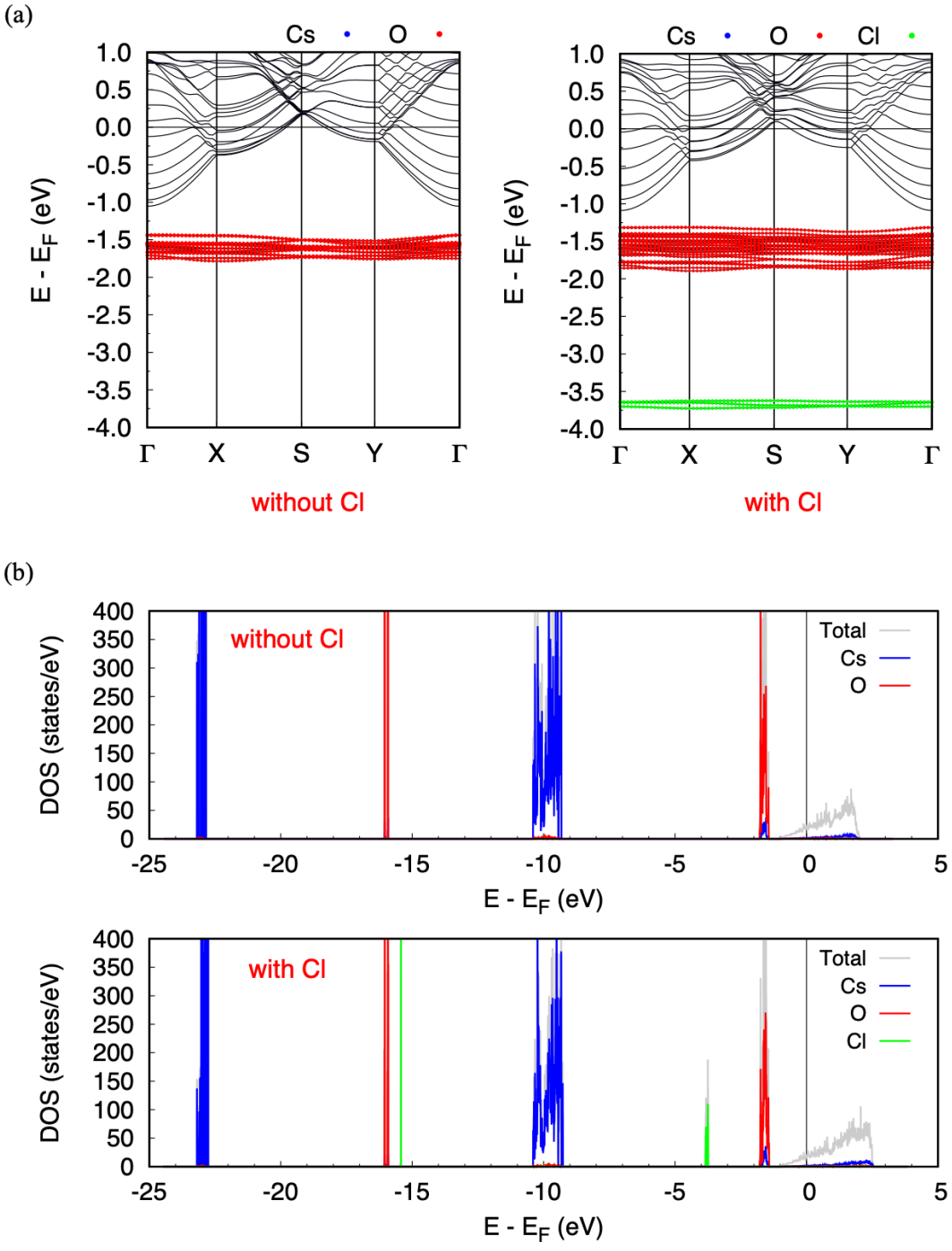


Figure 3. 15 (a) Band structures and (b) DOS projected on each species of the Cs_3O (100) surface with and without the Cl adsorbate.

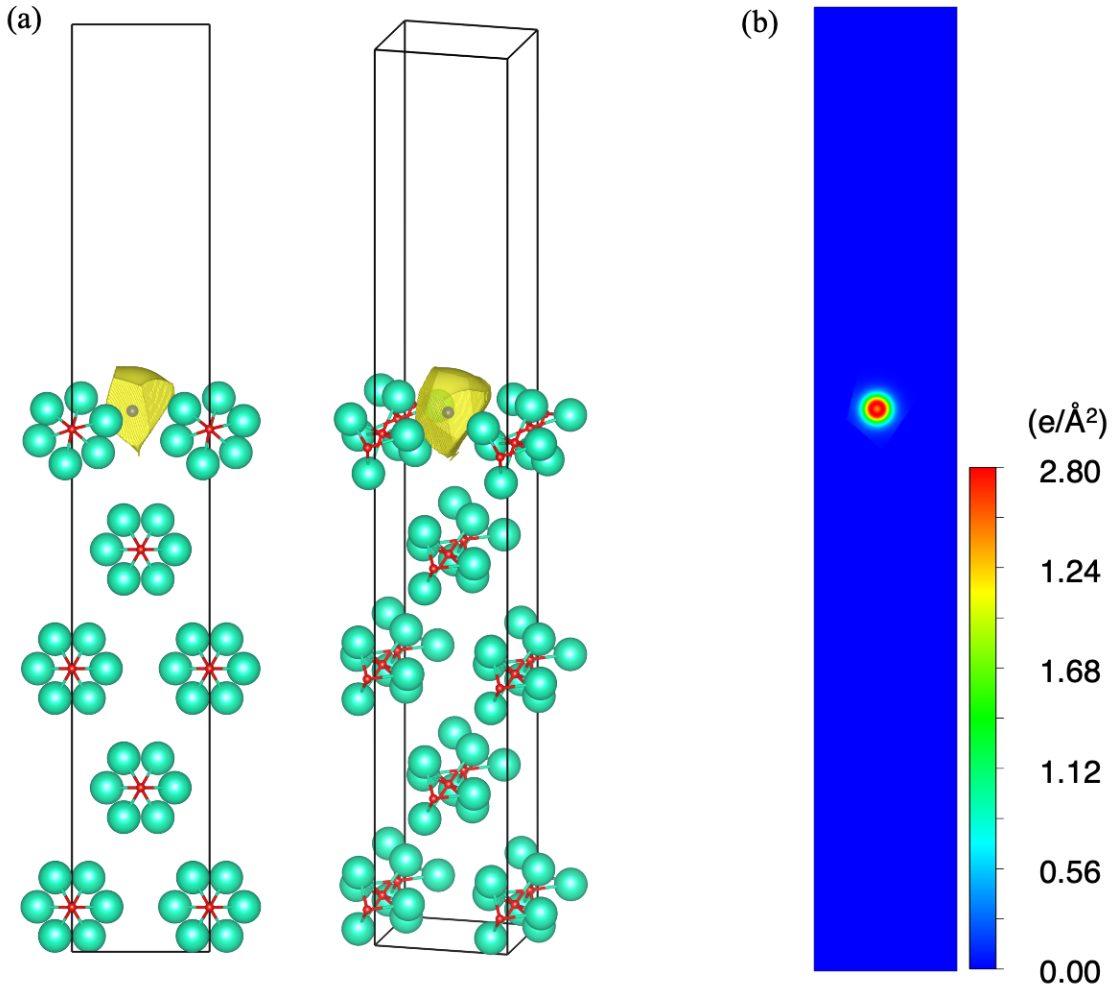


Figure 3. 16 Bader charge of adsorbate Cl on the Cs_3O (100) surface (a) Atomic structure of the surface and Bader volume for the Cl atom. (b) Integrated charge density of Cl Bader charge along the y-axis. The valence charge of the Cl atom is 7 e, whereas the Bader charge of the Cl is 7.896 e

The estimated surface dipole moment density induced by the charge transfer is shown in Fig. 3.17 The electron density around the Cl atom shows the depletion of anionic electrons near the Cl atom and the charge accumulation at the Cl atom. The induced surface dipole moment density converges to 0.0021 e/A in the vacuum region of the slab, which results in a decrease of the work function ($\Delta\Phi_2$) by -0.38 eV. This value is combined with a decrease in work function caused by structural deformation ($\Delta\Phi_1$= -0.05 eV), and the total work function change is -0.43eV.

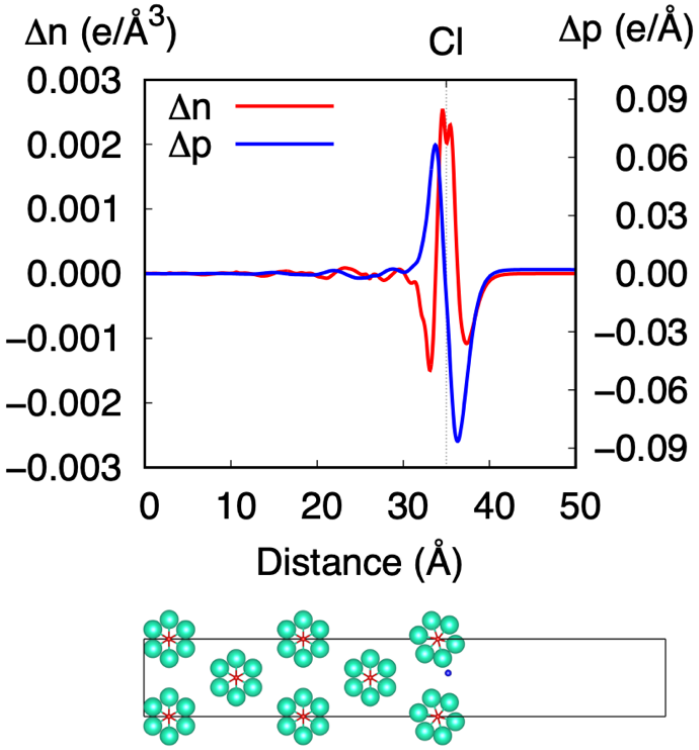


Figure 3. 17 Changes in electron density and surface dipole moment density due to charge transfer between Cl adsorbate and Cs_3O (100) surface.

3.5 Summary

The global structure predictions for the chemical composition of Cs_xO (x = 1, 2, 3) were carried out to explore the change of atomic structure according to the degree of oxidation of Cs, and the globally stable and metastable structures were identified for each chemical composition. In the case of Cs_3O, it was revealed that not only the most stable structure, but also metastable structures possess characteristics of the electride. The work functions for the low index orientation surfaces of all identified structures were calculated, and it was confirmed that the decreasing trend of work function as oxidation proceeds, which well agrees with experimental data. The lowest work function is calculated as 0.66eV for the (001) Cs terminated surface of the CsO Immm (#71) structure, which is not the most stable structure of this chemical composition but experimentally synthesized structure. A comparison of surface free energy according to the change of oxygen chemical potential shows that, in the wide range of experimental conditions, the surface with the lowest work function is the most stable in the same orientation and second stable among all possible low index orientations, suggesting that the work function of 0.66 eV is highly feasible. The work function change induced by adsorbates was also studied. The Cs_3O $P6_3/mcm$ (#193) structure, which is the electride, showed that the work function could be lowered by changing the distribution of the anionic electrons through the adsorption of electronegative atoms. In the case of the Cl adatom, the work function can be lowered by 0.43eV from 1.782 eV to 1.351 eV.

Chapter 4

Lithium Manganese Oxides: $Li_{1+x}Mn_2O_4$

4.1 Background

Beginning with the proven possibility of TiS_2 as cathode materials for Li-ion rechargeable batteries in 1976 [95], a variety of cathode materials have been studied to improve the performance of batteries for portable electronic devices [96,97]. In recent decades, intensive research has led to improvements in the stability and performance of rechargeable batteries, enabling the realization of electric vehicles with high power battery [98]. The underlying operating mechanism of Li-ion secondary batteries is reversible intercalation and deintercalation of Li ions into or from the cathode materials through electrolyte without significant change in their crystal structure.

Lithium manganese spinel $LiMn_2O_4$ began to attract attention as a promising cathode material after it was verified that Li ion insertion [99] and extraction [100] were possible without affecting its underlying MnO_2 framework. Figure 4.1 illustrates the crystal structure of $LiMn_2O_4$ cubic spinel, and phase transition induced by Li intercalation. 32 oxygen anions form a cubic-close-packed structure by occupying 32e sites, and 8 lithium cations are located in 8a tetrahedral sites. 16 manganese cations are occupying 16d octahedral sites leaving 8b tetrahedral and 16c octahedral sites empty. 32e oxygen and 16d manganese ions form MnO_2 framework which is known as λ-MnO_2. (To facilitate understanding of the changes in phase, throughout this document, the ionic positions in all structures will be described in terms of Wyckoff positions of the cubic spinel structure which belongs to space group $Fd\bar{3}m$, even if the structure is not a cubic spinel.)

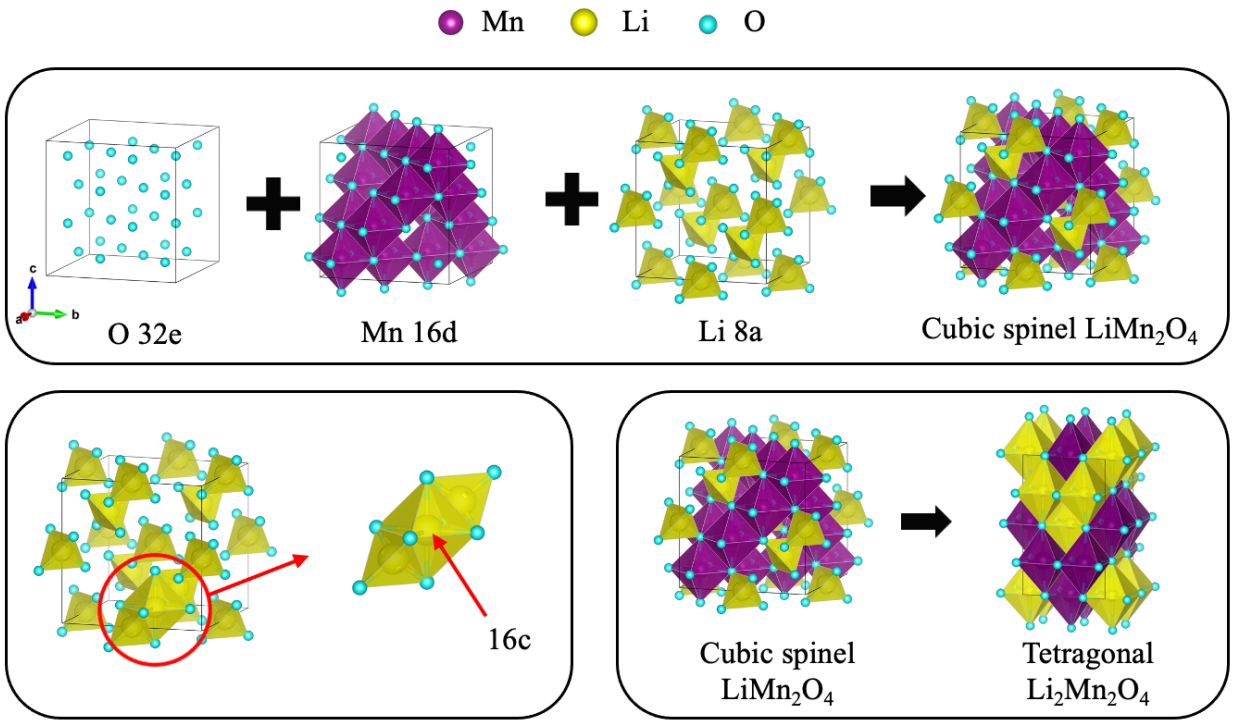


Figure 4. 1 Crystal structure of $LiMn_2O_4$, and phase transition from cubic spinel $LiMn_2O_4$ to tetragonal $Li_2Mn_2O_4$.

When Li intercalation takes place on this cubic spinel structure, newly inserted Li ions begin to occupy energetically favorable octahedral 16c sites. If the structure is fully intercalated with Li ions, the phase transition to tetragonal $Li_2Mn_2O_4$ structure occurs as all Li ions occupying 8a sites also move to 16 sites.

$LiMn_2O_4$ spinel turned out one of the successful cathode materials with low cost and low toxicity as well as high charge-discharge rate because it has three dimensional Li ion diffusion channel [101,102]. However, despite its advantages as a cathode material, the use of $LiMn_2O_4$ spinel is limited to the region of $-1 \leq x \leq 0$ ($Li_{1+x}Mn_2O_4$), because of local fracture resulting from anisotropic volume change during Li ion intercalation ($0 < x \leq 1$) into the $LiMn_2O_4$ spinel and

thus loss of electrical contact leading to degradation of cyclability of the secondary battery [99,103]. This anisotropic volume change is attributed to the cooperative Jahn-Teller distortion of Mn^{3+} ions [104]. Jahn-Teller distortion refers to the phenomenon of lowering the overall energy of an ionic complex by breaking of symmetry, octahedral complexes are typical cases. This phenomenon is related to removing orbital degeneracy by structural distortion under a specific electron configuration and consequently leading to energetic stabilization.

In the case of the MnO_6 octahedral complex (Fig.4.2), the Mn ion is surrounded by six oxygen anions, and the five-fold degeneracy of the d orbital is removed and divided into two levels due to the crystal field. These two levels are called t_{2g} and e_g, and d_{xy}, d_{xz}, d_{yz} orbitals correspond to the relatively low t_{2g} level, and d_{z^2} and $d_{x^2-y^2}$ orbitals belong to the high energy e_g level. Given those two energy levels for d orbitals, if the Mn ion is in the high spin Mn^{3+} ($[Ar]3d^4$) state, a single electron occupies e_g orbital, and the octahedral complex is stabilized by removing the degeneracy of the e_g level through the elongation (by occupying d_{z^2}) or compression (by occupying $d_{x^2-y^2}$) in the z-axis direction.

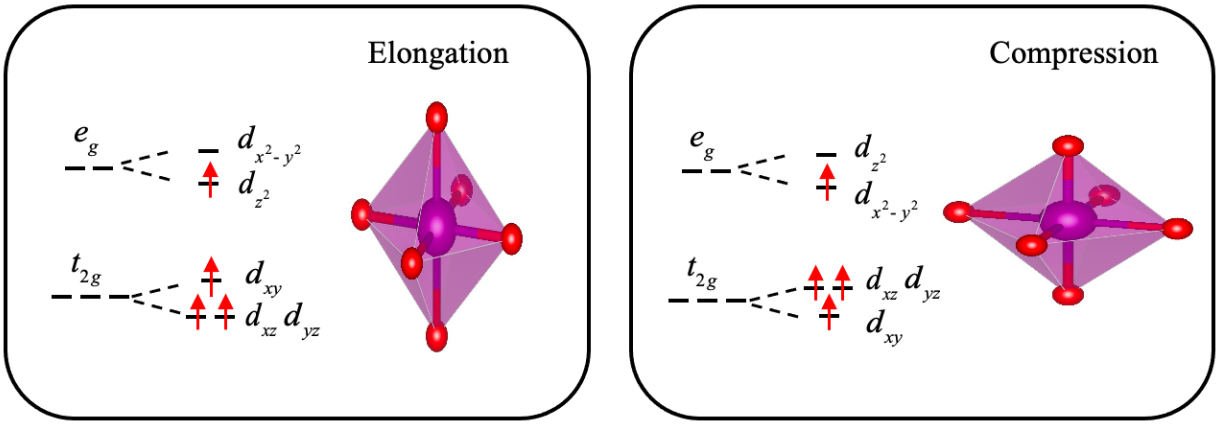


Figure 4. 2 Jahn-Teller distortions of MnO_6 octahedral complex.

In $LiMn_2O_4$ spinel, oxidation states for oxygen and lithium ions are O^{2-}, Li^{1+}, and Mn ions balance charge neutrality by occupying Mn^{3+} and Mn^{4+} states. Even though the spinel $LiMn_2O_4$ contains Jahn-Teller active Mn^{3+} ions, it maintains the cubic symmetry above T > 280K by randomly distributing Mn^{3+} and Mn^{4+} ions [105-109]. However, by the intercalation of Li ions into the spinel, Mn^{4+} ions change to Mn^{3+} state, which drives a phase transform to tetragonal $Li_2Mn_2O_4$ due to the cooperative Jahn-Teller distortion [110]. This phase transition from cubic $LiMn_2O_4$ to tetragonal $Li_2Mn_2O_4$ is known to occur through two-phase reaction in the compositional range $0.1 < x < 0.8$ in $Li_{1+x}Mn_2O_4$ [99,103], and first-principle phase diagram supports this with miscibility gap between $0 < x < 1$ [111]. However, the phase diagram can be significantly influenced by the size of the crystallites constituting the cathode material, and it has been found that when the crystallite size is considerably small (< 15 nm), the reaction occurs in a solid solution state without phase boundary which occurs in two-phase reaction [24]. Although the phase transition from the cubic $LiMn_2O_4$ to tetragonal $Li_2Mn_2O_4$ is well known, its intermediate structures have not been reported experimentally. This is because the two-phase reaction occurs in the lithium intercalation process, so that the intermediate phases can appear only at the phase boundary. These intermediate phases, which occur in only a fraction of the sample, are challenging to observe experimentally.

In this study, I concentrate on identifying possible intermediate phases ($Li_{1.5}Mn_2O_4$) that can appear locally near the phase boundary of the two-phase reaction. After identifying possible intermediate phases, their magnetic, electronic, and structural properties are analyzed, including cubic $LiMn_2O_4$ (x=0) and tetragonal $Li_2Mn_2O_4$ (x=1).

4.2 Stable and Metastable Structures (x = 1, 1.5, and 2)

MnO_2 is a polymorphic compound with a wide variety of crystal structures, and the most common 6 phases are β, γ, R, α, δ, and λ [112]. The phases are shown in Fig. 4.3. These phases are known to accommodate alkali or alkali-earth cations without significant changes in their underlying MnO_2 framework. Among these, the cubic spinel $LiMn_2O_4$ and the tetragonal $Li_2Mn_2O_4$ structures share the MnO_2 framework of the λ phase.

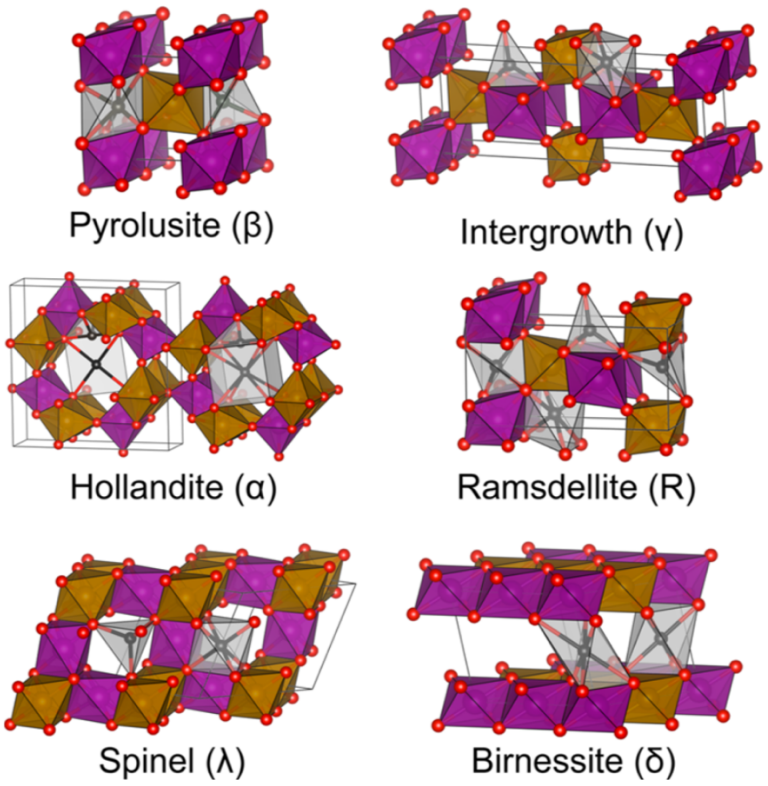


Figure 4. 3 Common polymorphs of MnO_2 phase. The purple and brown octahedra indicate MnO_6 complexes with spin up and down Mn atoms. The grey polyhedra denote potential intercalation sites for inserted anions. Reprint from Ref. **[112]**

This polymorphism of MnO_2 significantly expands the possible solution space in global structure prediction, which can be an obstacle in fully exploring $Li_{1+x}Mn_2O_4$ with the λ phase. Therefore, analyzing the structures of the $Li_{1+x}Mn_2O_4$ with the λ phase by performing a structure prediction using only the chemical composition is not only very inefficient but also cannot guarantee the acquisition of a sufficient amount of data. This is because that the global structure prediction may converge to other phases that we are not interested in, and even if it converges to the λ phase, we additionally need to extract structures with λ phase from large amounts of data. Fortunately, however, the δ and λ phases share the same oxygen sublattices of the face-centered cubic (FCC), whereas the other phases exhibit hexagonal close packing (HCP) oxygen sublattice. By using this difference, we can impose constraints on the positions of oxygen atoms during the structure prediction, which can significantly reduce the search space.

I performed a constrained global structure prediction using simulation cells that contain two formula units of $Li_{1+x}Mn_2O_4$ (x = 0, 0.5, and 1) and have the same cell parameters and oxygen positions as cubic spinel $LiMn_2O_4$ (Fig 4.4).

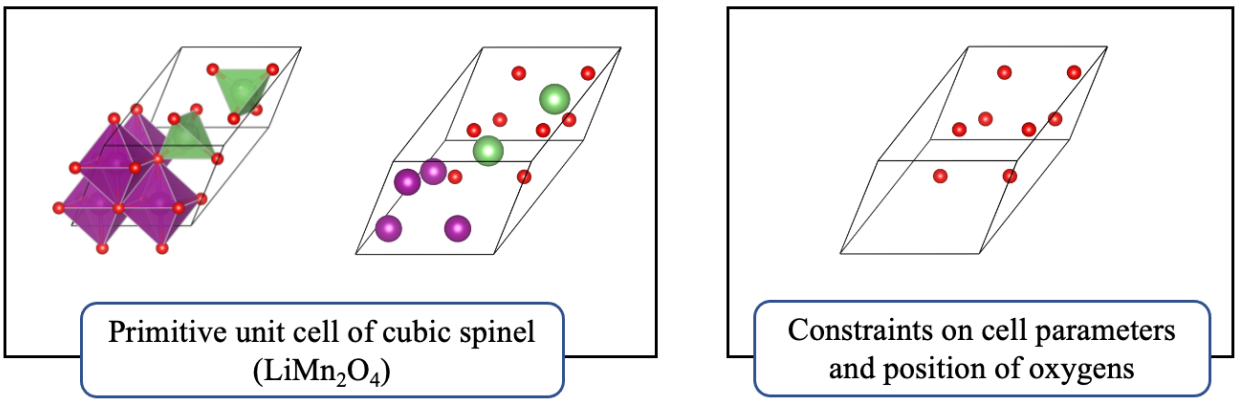


Figure 4. 4 Constraints imposed on crystal structure search.

The magnetic configurations of Mn ions were set to the ferromagnetic spin order, and the same magnetic configuration was used to analyze the identified structures. Table 4.1 shows energy values and structural, electronic features of the identified structures corresponding to the λ phase.

Interestingly, one or two structures were identified for the initial (x = 0) and final (x = 1) compositions of the phase transitions, whereas, twelve structures were found for the intermediate (x = 0.5) composition in a relatively small energy range of 40 meV/atom. These results show that structures of different phases can exist as metastable states in the middle of a phase transition. I will take a closer look at the structures identified in the initial and final compositions and intermediate phases in the following sections.

4.3 Electronic and Structural Properties Depending on the Stoichiometry (x)

4.3.2 Initial and Final Structures: $Li_xMn_2O_4$ (x = 1 and 2)

Figure 4.5 (a) shows the crystal structures of S-1, S-2 (x = 0), and F-1 (x = 1) structures, and the oxidation states of each Mn ion are distinguished by different colors. In all three structures, MnO_6 octahedra complexes centered by Jahn-Teller active Mn^{3+} ion ($Mn^{(3+)}O_6$) are all elongated in the same direction, and these structures were analyzed by selecting this direction as the z-axis.

The oxidation state of Mn ions and the local Jahn-Teller distortions of MnO_6 octahedra summarized in Table 4.1 are determined by examining the density of states and partial charge distribution of d orbitals. Figure. 4.6 (b) shows the density of states projected on d orbitals for each Mn ion.

Table 4. 1 Information about identified structures for $Li_{1+x}Mn_2O_4$ (x = 0, 0.5, and 1) through global structure prediction. For index, S, I, and F stand for start, intermediate, and final composition, respectively. ΔE is the energy difference compared to the most stable structure of the corresponding composition. Local Jahn-Teller distortion represents the direction and type of the deformation for each $Mn^{(3+)}O_6$ octahedra, A character with an overbar indicates compression, otherwise elongation.

x	Index	Energy/atom (eV)	ΔE (meV)	Oxidation State of Mn	Local JT distortion	Li Sites (Tet. : Oct.)	Space Group	Lattice System
0	S-1	-6.7397	-	4/4/3/3	zz	2 : 0	Imma (74)	Orthorhombic
	S-2	-6.6890	50.7	4/4/3/3	zz	0 : 2	C2/c (15)	Monoclinic
0.5	I-1	-6.5916	-	4/3/3/3	zxz	0 : 3	P1 (1)	Triclinic
	I-2	-6.5913	0.3	4/3/3/3	zxz	0 : 3	P-1 (2)	Triclinic
	I-3	-6.5912	0.4	4/3/3/3	xzy	0 : 3	P1 (1)	Triclinic
	I-4	-6.5907	0.9	4/3/3/3	xzy	0 : 3	$R\bar{3}$ (148)	Rhombohedral
	I-5	-6.5886	3.1	4/3/3/3	zzz	0 : 3	C2/m (12)	Monoclinic
	I-6	-6.5868	4.8	4/3/3/3	zzz	2 : 1	C2/m (12)	Monoclinic
	I-7	-6.5839	7.7	4/3/3/3	zzz	1 : 2	P1 (1)	Triclinic
	I-8	-6.5763	15.3	4/3/3/3	z$\bar{y}$x	0 : 3	C2/m (12)	Monoclinic
	I-9	-6.5741	17.6	4/4/3/2	y	1 : 2	Cm (8)	Monoclinic
	I-10	-6.5726	19.0	4/4/3/2	y	2 : 1	C2/m (12)	Monoclinic
	I-11	-6.5694	22.2	4/3/3/3	$\bar{z}$xy	1 : 2	Cm (8)	Monoclinic
	I-12	-6.5534	38.2	4/3/3/3	$\bar{z}\bar{y}\bar{x}$	0 : 3	$R\bar{3}$m (166)	Rhombohedral
1	F-1	-6.4962	-	3/3/3/3	zzzz	0 : 4	$I4_1$/amd (141)	Tetragonal

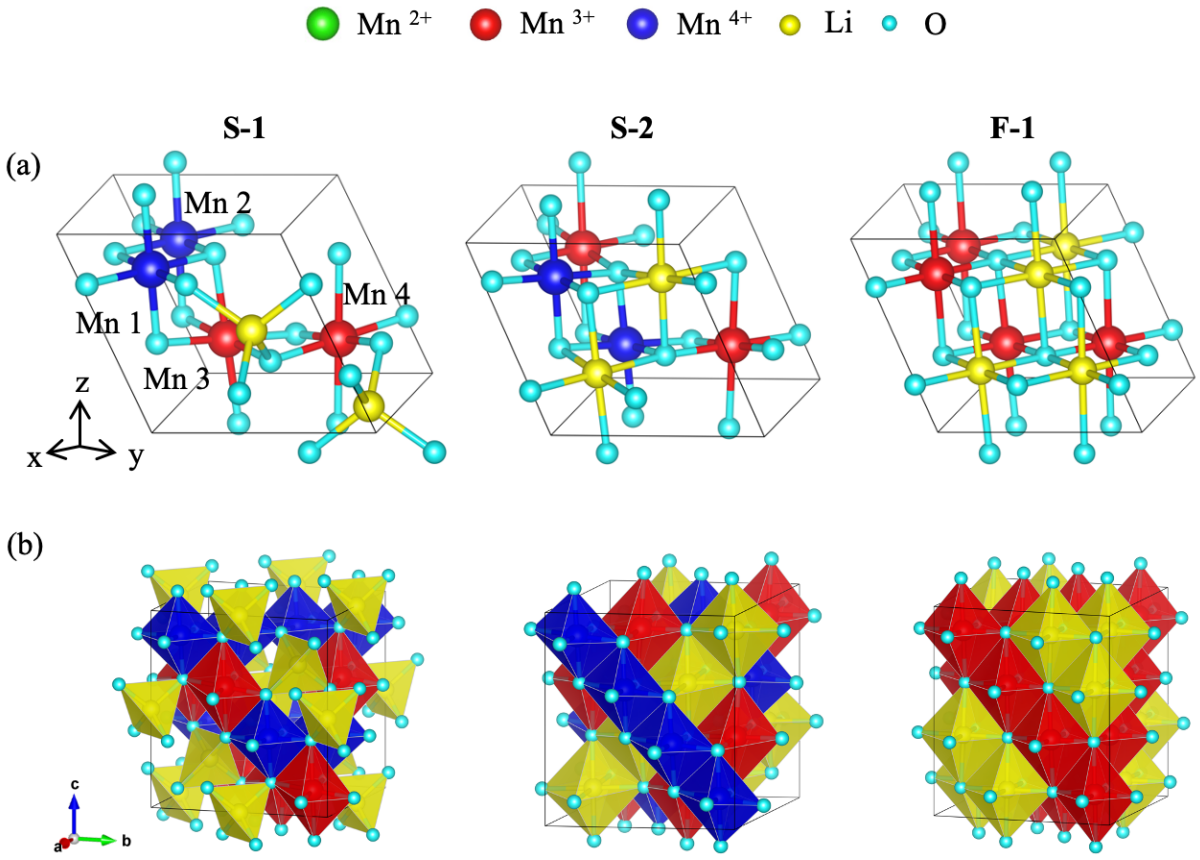


Figure 4. 5 Crystal structures of the start (x = 0) and final (x = 1) compositions in (a) primitive unit cell and (b) pseudo-cubic unit cell.

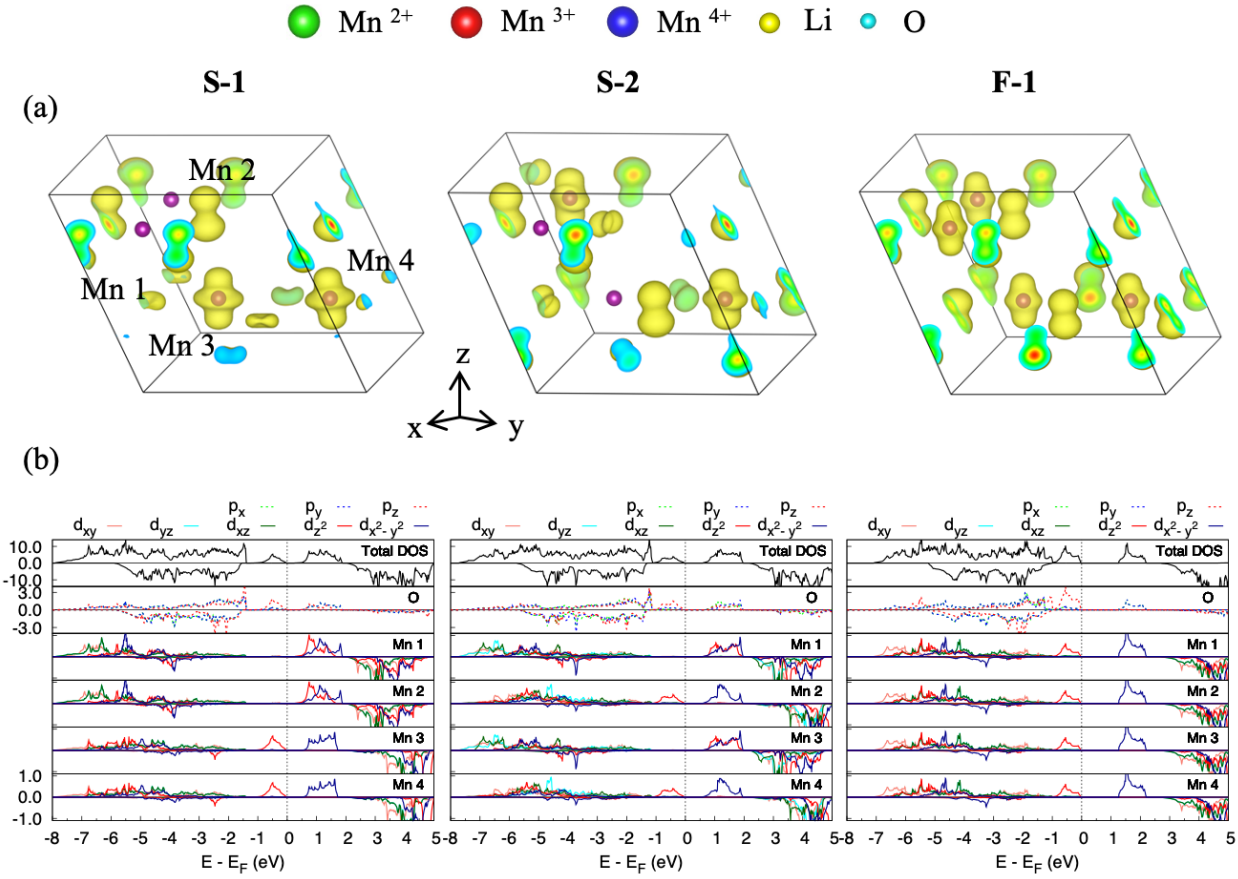


Figure 4. 6 (a) Partial charge density in the energy range of -1.2 eV < E-E_F < 0 eV. The isosurface is randomly selected to represent the shape of the Mn d orbital. (b) Total and orbital projected local density of states with both spin majority (positive) and minority (negative) channel. While the contributions from every O ion are summed up, local DOS for each Mn ion is presented.

From the DOS, it can be seen that the t_{2g} level electrons (d_{xy}, d_{xz}, d_{yz}) are filled in -7 eV < E-E_F < -2 eV, while the e_g level electrons (d_{z^2}, $d_{x^2-y^2}$) are distributed in -1 eV < E-E_F < 2 eV due to the crystal field of the MnO_6 octahedral complex. According to the ligand field theory, which more specifically explains the separation of energy levels by applying molecular orbital theory to accommodate covalent interactions, t_{2g} electrons of metal ion form relatively weak π bonding with electrons from ligands, whereas e_g electrons build strong σ bonding. This σ bonding results in a significant separation of the bonding and anti-bonding levels. The e_g electrons in -1 eV < E-E_F < 2 eV correspond to the anti-bonding level, and the contribution of the e_g electrons in -7 eV < E-E_F < -2 eV relates to the bonding level. e_g^* symbol will be used to indicate the anti-bonding e_g level. For the S-1 and S-2 structures, the e_g^* level shows the degeneracy corresponding to d_{z^2} and $d_{x^2-y^2}$ orbitals in the case of two Mn^{4+} ions, whereas, for the other two Mn^{3+} ions, the degeneracy of the e_g^* level is removed by Jahn-Teller elongation, and an electron occupies d_{z^2} orbital. On the other hand, in the F-1 structure, all four Mn ions exhibit Mn^{3+} oxidation state occupying d_{z^2} orbital by lithium intercalation. The occupancy of this d_{z^2} orbital can be reconfirmed through the visualization of the partial charge density of the electrons in the energy range of –1.2 eV ≤ E-E_F ≤ 0 eV, as shown in Fig. 4.1 (a).

By examining the pseudo-cubic unit cells shown in Fig.4.5 (b), their structural differences can be understood more clearly. The S-1 structure, the ground state of the $LiMn_2O_4$ composition, is a spinel structure deformed from cubic to orthorhombic structure by Jahn-Teller distortion at 0K. The S-2 structure differs from the S-1 in terms of the crystal site occupied by Li ions. In the case of S-1, eight Li ions occupy the most favorable 8a tetrahedral site, whereas those are located at unfavorable 16c octahedral sites in the metastable S-2 structure making its energy 50.7 meV/atom higher than the S-1. In the S-2 structure, half of the possible 16c sites are occupied by Li ions, and

layers fully filled with Li ions and the Li ion free layers are alternately repeated along the [100] direction. The F-1 structure saturates all possible 16c octahedral sites with fully intercalated Li ions. Another difference between the S-1 and the S-2 is the arrangement of Mn^{3+} and Mn^{4+} ions. In the S-1, Mn ions located in the plane parallel to the (001) plane have the same oxidation state, and the states of Mn^{3+} and Mn^{4+} alternately appear along the [001] direction. However, in the S-2, the layer fully filled with Li ions in the [100] direction have Mn^{3+} ions, and Mn^{4+} ions are located in the Li ion free layer.

4.3.2 Intermediate Structures: $Li_xMn_2O_4$ (x = 1.5)

Figure 4.7 (a) shows the results of the global structure prediction performed on the chemical composition of $Li_{1.5}Mn_2O_4$, and the horizontal blue lines in the graph indicate the structures exhibiting the λ-phase MnO_2 which is a framework of the spinel structure. As shown in Table 4.1, unlike the initial (x = 0) and final (x = 1) compositions, relatively large numbers of (meta)stable structures have been identified for the intermediate (x = 0.5) composition.

The reason why a large number of metastable structures appear in a relatively narrow energy range is that various degrees of freedom for crystal formation are arisen by additionally intercalated Li ions. Those degrees of freedom are oxidation states of Mn ions, local Jahn-Teller distortions of Mn^{3+}, and position of Li ions as shown in 4.7 (b). In the following discussion, the analysis of 12 identified structures explains how these three variables influence crystal phases.

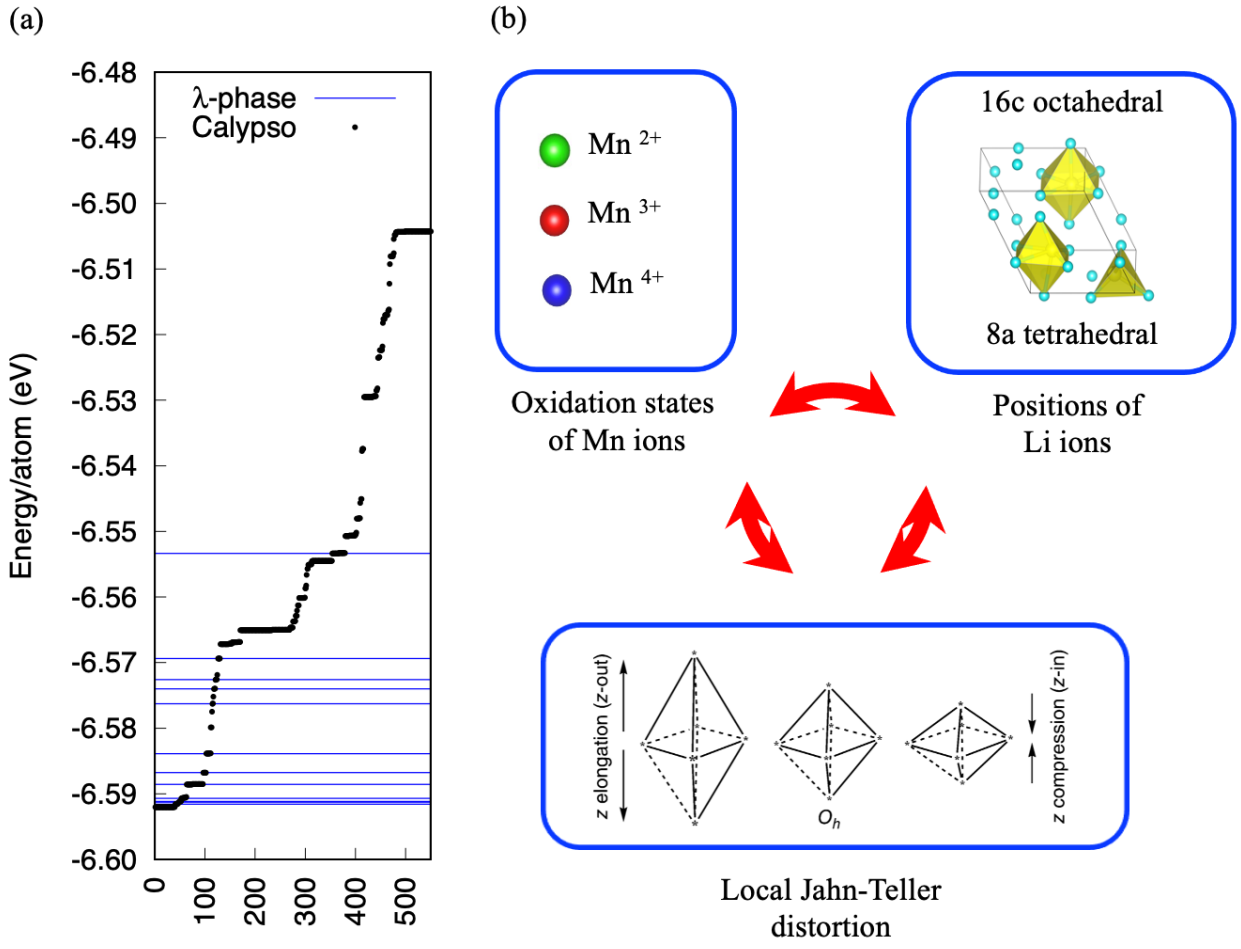


Figure 4. 7 (a) Identified structures through global structure prediction for $Li_{1.5}Mn_2O_4$. The black dots represent all the structures identified from the structure prediction, and the structures with the λ-MnO_2 framework are indicated by blue horizontal lines. (b) A schematic diagram for various degrees of freedom which can interplay to determine crystal and electronic structure.

4.3.2.1 Oxidation States of Mn Ions

The first degree of freedom is the oxidation states of Mn ions. If we consider the chemical composition ($Li_{1.5}Mn_2O_4$) and the charge neutrality, Mn ions can have one Mn^{4+} and three Mn^{3+} (4/3/3/3), or two Mn^{4+}, one Mn^{3+}, and one Mn^{2+} (4/4/3/2) states. The I-9 and I-10 structures in Table 4.1 correspond to the latter, and the other ten structures exhibit the oxidation states of the former. By comparing the I-7 and I-9 structures, we can see how the oxidation states of the Mn ions affect the electronic structures. As shown in Fig. 4.8 (a), these two structures share almost the same atomic configurations in which two and one Li ions occupy the octahedral and tetrahedral site, respectively, in the λ-phase MnO_2 framework. However, in the I-7 structure, three Mn ions (Mn2, Mn3, Mn4) are Jahn-Teller active Mn^{3+} elongated along the z-axis, whereas in the I-9 structure, only one Mn ion (Mn2) shows Mn^{3+} elongated in the y-axis, and another Mn ion (Mn4) is in Mn^{2+} state. By comparing the localized density of states of Mn ions of the I-9 structure depicted in Fig. 4.8 (b), the difference in electronic structures between Mn^{4+} (Mn1 and Mn3), Mn^{3+} (Mn2), and Mn^{2+} (Mn4) states can be understood. In the $Mn3^{(4+)}$ ion, electrons do not occupy the e_g^* level, and there is a significant gap between the t_{2g} and e_g^* bands. In the $Mn2^{(3+)}$ ion, which has one more electron than the $Mn3^{(4+)}$, the degeneracy of the e_g^* level is removed, and the occupancy of the low energy orbital causes the Jahn-Teller elongation along the y-axis direction. Compared to the $Mn3^{(4+)}$, the energy distribution of the t_{2g} and bonding e_g band electrons does not change much. However, in the $Mn4^{(2+)}$ ion, the degeneracy of the e_g^* level is restored by occupying the remaining e_g^* orbital, and the octahedron eventually expands in all directions. Compared to the $Mn3^{(4+)}$ and $Mn2^{(3+)}$, a splitting gap between the t_{2g} (and also e_g) and e_g^* level is clearly reduced, and this can be explained as a result of the reduced ligand field on Mn *d* orbitals due to the expansion of the octahedron.

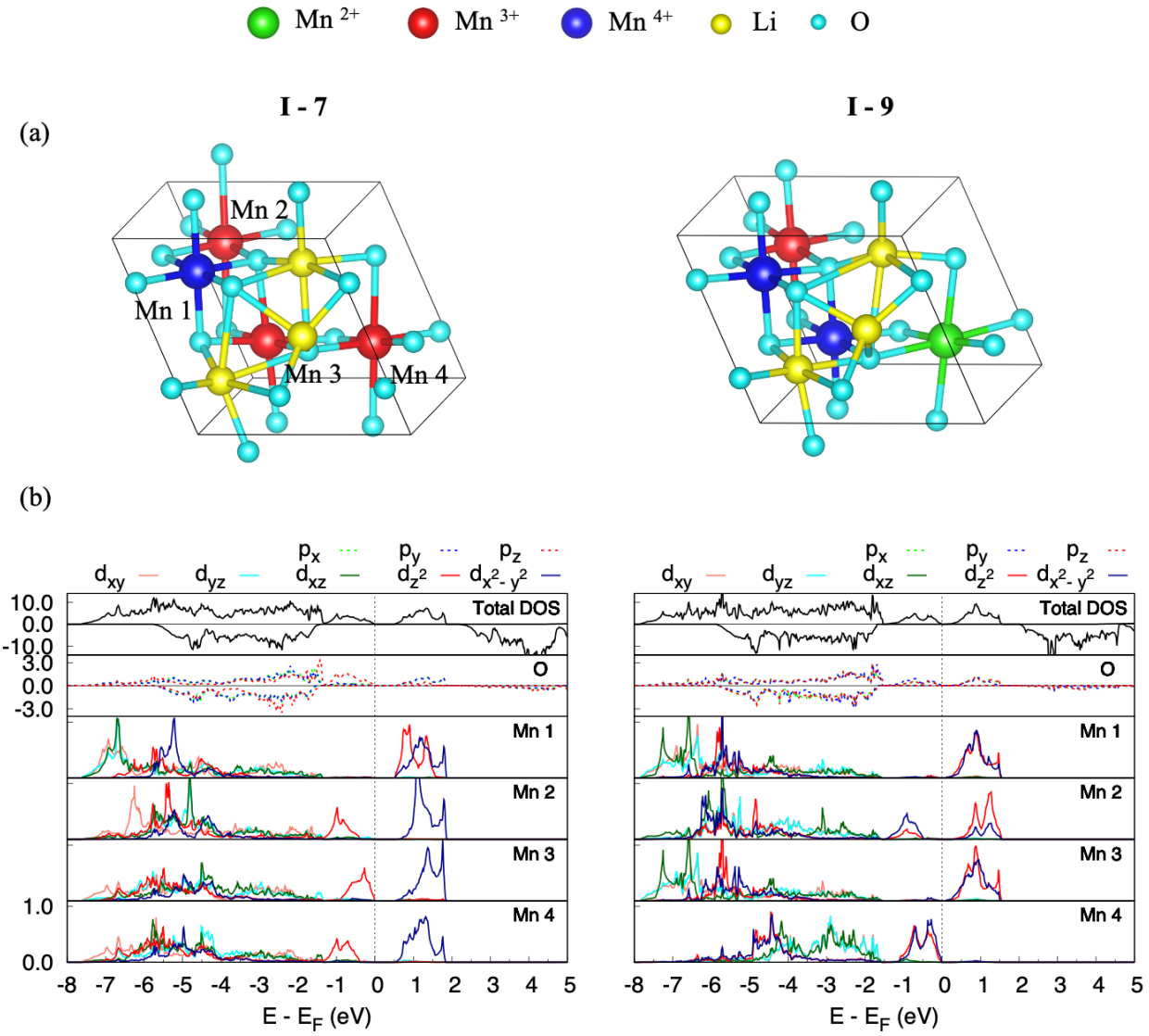


Figure 4. 8 (a) Crystal structures of I-7 and I-9 representing two different charge states of Mn ions and (b) total and local density of states. Only the spin majority channel is depicted for Mn ions.

The I-9 structure (4/4/3/2) shows higher energy (10 meV/atom) than the I-7 (4/3/3/3), and this increase in the energy might result from the fact that the energy level of the t_{2g} and e_g bands are elevated due to the contraction of the splitting gap in the $Mn4^{(2+)}$ ion. That is, the 4/3/3/3 configuration, which contains more Jahn-Teller active Mn^{3+} ions in which the e_g^* level is partially filled, is more favorable than 4/4/3/2 configuration holding the Mn^{2+} ion in which the e_g^* orbitals are fully filled.

4.3.2.2 Crystal Sites Occupied by Li Ions

The second possible degree of freedom is crystal sites occupied by Li ions. It was predicted that the Li ions intercalated into the $LiMn_2O_4$ spinel would gradually start to occupy the 16c octahedral sites because 8a sites are already saturated [99,113]. However, there is a disagreement on the effect of the newly introduced Li ions at the 16c sites on the existing Li ions located at the adjacent 8a tetrahedral sites. While there is an assertion that the electrostatic repulsion between Li ions located at the 16c site and the adjacent 8a site is not strong enough so that Li ions can be inserted into the 16c sites without changing the position of existing 8a sites [99], it is also argued that the Li ion inserted into the 16c octahedral site causes immediate displacement of the face sharing Li ions at the adjacent 8a sites into the vacant 16c site [113].

The structures I-5, I-6, and I-7 in Table 4.1 lie in a very narrow energy range of about 5 meV/atom and show the same status of oxidation states of Mn ions and local Jahn-Tell distortions of $Mn^{(3+)}O_6$ octahedra. However, they differ in the crystal sites occupied by Li ions. As shown in Fig. 4.9 (a), whereas all three Li ions occupy the octahedral sites in the I-5 structure, two and one Li ions are located at the tetrahedral sites in I-6 and I-7, respectively. The change in positions of Li ions due to the Li intercalation is shown in Fig 4.10.

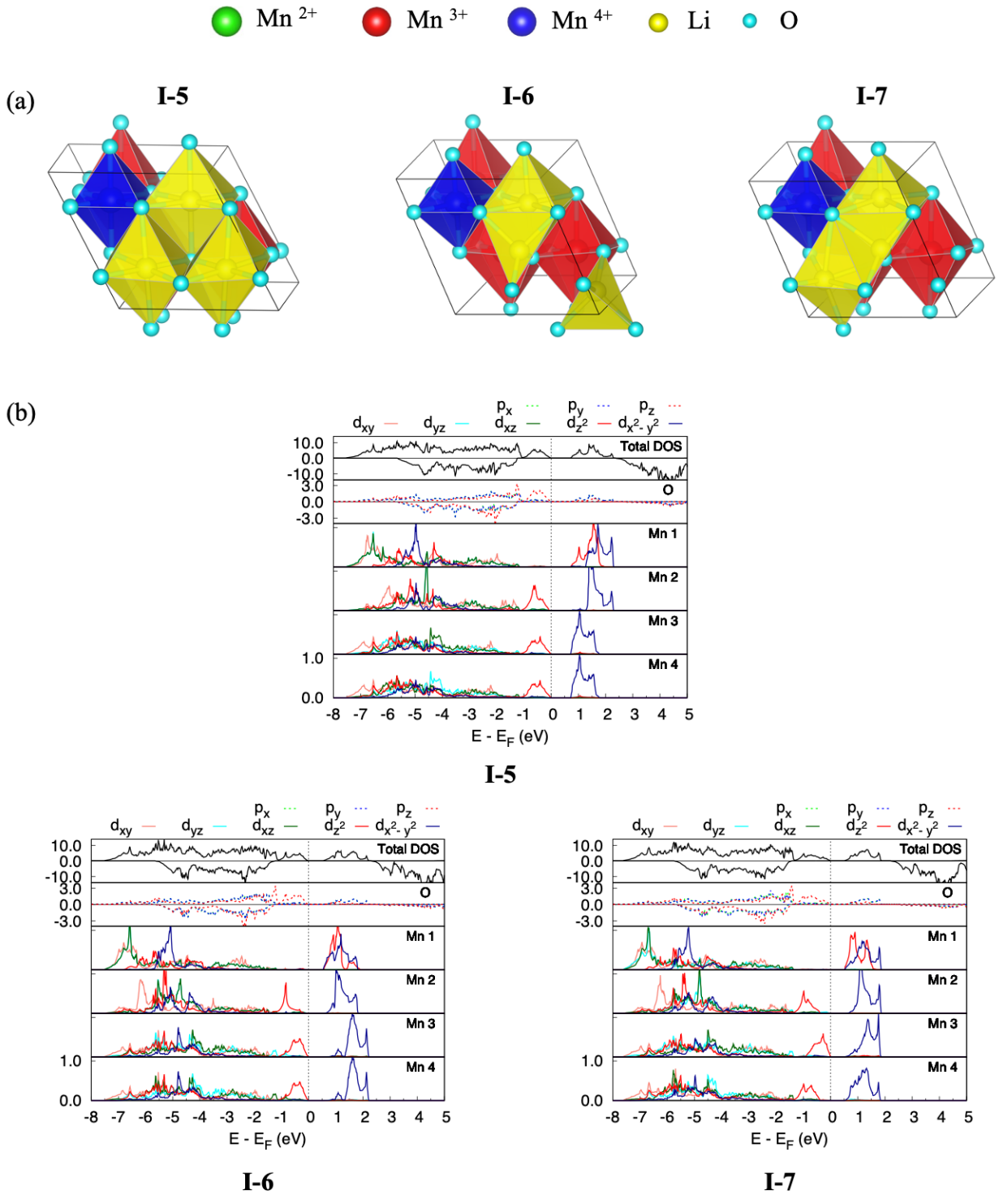


Figure 4. 9 (a) Crystal structure of the I-5, I-6, and I-7 with Li ions located in different crystal sites. (b) Total and local density of states

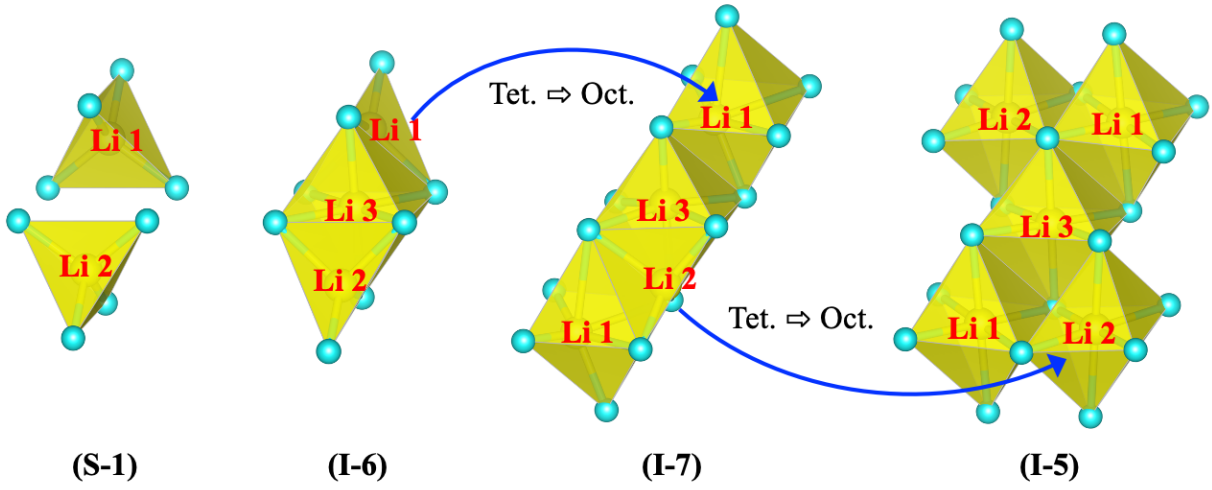


Figure 4. 10 Li intercalation into the octahedral 16c site (Li3) and change of positions of adjacent Li ions at 8a sites (Li1 and Li2).

In the S-1 structure, two Li ions (Li1 and Li2) are located at the tetrahedral sites, and newly inserted Li3 ion enters into the octahedral 16c site between the two existing Li ions, and this corresponds to I-6 structure. From this structure, if the Li1 ion in the tetrahedral site moves to the octahedral site, it forms an edge-sharing Li octahedra chain consisting of Li1 and Li3, and Li2 in the tetrahedral site shares its two faces with adjacent Li ions. This is the case of the I-7 structure. Furthermore, if the Li2 at the tetrahedral site finally moves to another octahedral site, forming an edge-sharing Li-octahedral plane, the I-7 structure transforms into the I-5 structure which is the most stable configuration among those three. The important point to note here is that those three structures are all fully relaxed. This suggests that, although the I-5 structure shows the favored Li ion configuration, the Coulomb repulsion between the Li ions itself is not sufficient to have the Li ions at the tetrahedral sites spontaneously move into the vacant octahedral sites. However, the fact

that all Li ions in the low energy structures (I-1 ~ I-5) occupy octahedral sites reconfirms that the 16c octahedral site is more favorable for Li ions in the $Li_{1.5}Mn_2O_4$ composition.

4.3.2.3 Configurations of Local Jahn-Teller Distortions

The third degrees of freedom to examine is a different configuration of local Jahn-Teller distortions that take place at each $Mn^{(3+)}O_6$ octahedron. The Jahn-Teller effect occurs in either elongation or compression along the z-axis, depending on which e_g^* orbital (d_{z^2} and $d_{x^2-y^2}$) is occupied by *d* electron of the metal ion located in the center of the octahedron. However, considering that the crystal field of the octahedral complex has cubic symmetry, the Jahn-Teller distortion can occur in any direction of *x*, *y*, and *z*. The e_g^* orbitals associated with elongation and compression along each axis can be represented by a linear combination of two orthogonal d_{z^2} and $d_{x^2-y^2}$ orbitals, $|\psi(\theta)\rangle = \cos\theta\,|d_{3z^2-r^2}\rangle + \sin\theta\,|d_{x^2-y^2}\rangle$, and six possible cases are listed in Table 4.2.

Table 4. 2 Linear combinations of $\boldsymbol{d_{z^2}}$ and $\boldsymbol{d_{x^2-y^2}}$ representing relevant orbitals to elongations and compressions in the x, y, and z axes. The $\boldsymbol{d_{3z^2-r^2}}$ orbital represents the more explicit form of the $\boldsymbol{d_{z^2}}$.

	elongation	compression
x	$\|d_{3x^2-r^2}\rangle = -1/2\,\|d_{3z^2-r^2}\rangle + \sqrt{3}/2\,\|d_{x^2-y^2}\rangle$	$\|d_{y^2-z^2}\rangle = -\sqrt{3}/2\,\|d_{3z^2-r^2}\rangle - 1/2\,\|d_{x^2-y^2}\rangle$
y	$\|d_{3y^2-r^2}\rangle = -1/2\,\|d_{3z^2-r^2}\rangle - \sqrt{3}/2\,\|d_{x^2-y^2}\rangle$	$\|d_{z^2-x^2}\rangle = \sqrt{3}/2\,\|d_{3z^2-r^2}\rangle - 1/2\,\|d_{x^2-y^2}\rangle$
z	$\|d_{3z^2-r^2}\rangle$	$\|d_{x^2-y^2}\rangle$

Given the structures containing three Jahn-Teller active ions (Mn^{3+}) in the unit cell (that is, 4/3/3/3 oxidation states of Mn ions), the first phenomenon we can notice from the intermediate structures concerning the local Jahn-Teller distortion is that structures containing compressed $Mn^{(3+)}O_6$ octahedron, such as I-8, I-11, and I-12, show relatively higher energies. This is consistent with the DFT calculation results performed on the Mn(β-diketonato)$_3$ molecule containing the $Mn^{(3+)}O_6$ octahedral complex [114]. Next, it should be noted that when elongation occurs in all three $Mn^{(3+)}O_6$ octahedra, the relative direction of each elongation can appear differently.

Figure 4.11 shows crystal and electronic structures of I-1, I-3, and I-5 structures. These structures exhibit the same Mn oxidation states and Li ion occupations. The only difference is the directions of local Jahn-Teller distortions occurring at each Mn^{3+} ion. In the partial charge densities shown in Fig. 4.11 (b), the lobes of the charge distribution corresponding to the occupied Mn d orbital show the direction of Jahn-Teller elongations. As shown in the figure, elongation occurs in all three $Mn^{3+}O_6$ octahedra for all three structures, but the relative directions of elongation are different. In the I-5 structure, all three Mn^{3+} ions are elongated in the same direction (*zzz*), while in the I-3 structure, they are all elongated in different directions (*xzy*). In the most stable I-1 structure, the two octahedra are elongated in the same direction, and the other one is elongated in a direction perpendicular to that (*zxz*). I-1 and I-3 show a very small energy difference of 0.4 meV/atom, while the energy of I-3 and I-5 differ by 2.7 meV/atom.

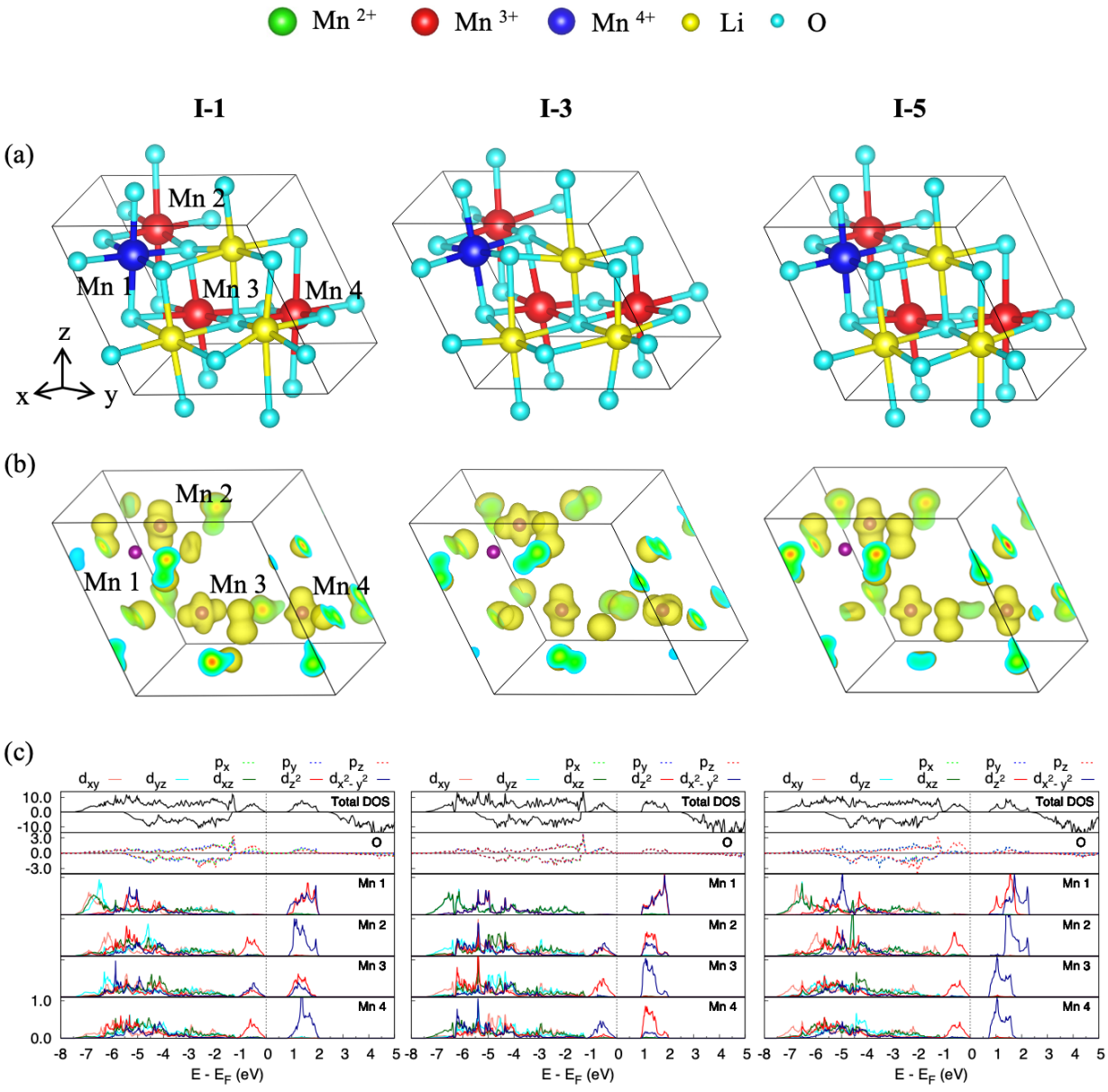


Figure 4. 11 (a) Crystal structure of the I-1, I-3, and I-5 with different configurations of local Jahn-Teller distortions. (b) Partial charge density in the energy range of -1.2 eV < E-E_F < 0 eV. (c) Total and local density of states. Orbital projected local DOS for Mn3 of the I-1, and Mn2, Mn4 of the I-3 shows the linear combinations of $\boldsymbol{d_{z^2}}$ and $\boldsymbol{d_{x^2-y^2}}$ orbitals in -1.2 eV < E-E_F < 0 eV with more contribution from $\boldsymbol{d_{x^2-y^2}}$, which indicates elongations along the x or y axes. The direction can be determined by observing the partial charge dentisity.

4.4 Summary

The crystal structure prediction with constraints imposed on oxygen positions and lattice parameters were performed for the chemical composition of $Li_{1+x}Mn_2O_4$ (x=0, 0.5, 1) to investigate the change of crystal and electronic structures induced by Li insertion. The results of the crystal structure prediction revealed the complexity of intermediate phases. While only one or two structures were identified in the composition of the initial (x = 0) and final (x = 1) stages of the phase transition, 12 structures were identified in the intermediate (x = 0.5) composition. Differences between these 12 structures distributed over a relatively narrow energy range of 40 meV/atom can be explained by considering various degrees of freedom caused by Li intercalation. The identified structures were analyzed in terms of oxidation states of Mn ions, positions of Li ions, and local Jahn-Teller distortions of $Mn^{(3+)}O_6$ octahedron by utilizing first-principles DFT calculations. The cycle capacity fade that occurs in the $0 < x < 1$ range of spinel $Li_{1+x}Mn_2O_4$ during the operation of a Li ion rechargeable battery has been explained by anisotropic volume change between the cubic and tetragonal phases. However, our study suggests that the presence of various metastable structures in the intermediate composition of $Li_{1.5}Mn_2O_4$ could be another cause of the capacity fade.

Chapter 5

Yttrium Silicide: Y_5Si_3

5.1 Background

Electrides are a kind of new class of materials where electrons are not strongly bound to any specific atom and serve as the anions [115]. Hence, those electrons are called anionic electrons and confined within a cavity space of the lattice. The name, electride, was coined by James Dye who identified anionic electrons from thin films produced by evaporating methylamine containing cryptated alkali cations in 1978 [116]. After the existence of anionic electrons was confirmed by Dye, efforts were made to find crystalline electrides, and in 1983, the first crystalline organic electride, $Cs^+(18\text{-crown-}6)_2e^-$, was synthesized [117] and characterized [118] by Dye et al. Although other types of organic elecrides have been synthesized [119-123], they were thermally unstable and highly sensitive to air and water [124]. Therefore, it was desired to find inorganic electrides for practical applications. The first inorganic electride, $[Ca_{24}Al_{28}O_{64}]^{4+}(4e^-)$, was synthesized by Kitano et al. in 2012 [125]. This material has a cage structure capable of trapping anionic electrons. Since then, other types of inorganic electrides such as Ca_2N [126] and LnRuSi [127] have been successfully synthesized. Recently, efforts have been made to design new electrides by combining database screening, crystal structure prediction with first-principle calculations [17,128-131]. Researchers have been trying to synthesize and design new electrides because of the unique characteristics of the electrides and their potential in various applications. One of the unique characteristics of electride is its electron-donating ability. Electrides show a low work function and can continuously provide excess electrons. Thanks to these properties,

$[Ca_{24}Al_{28}O_{64}]4^{+}(4e^{-})$ shows an efficient thermionic electron emission in the applied electric field, which can be utilized in a display device [132]. It was also demonstrated that a low barrier electron injection is possible in organic light-emitting diodes using this electride [133]. Ru-loaded electrides are also known as an excellent electron donor for catalytic reactions for direct ammonia synthesis [125-127]. Y_5Si_3 is one of those electrides that can effectively activate the N_2 molecule by lowering the energy barrier of the N_2 dissociation which is a rate-limiting process of the ammonia synthesis [26]. Although it was verified that Y_5Si_3 can enhance the catalytic activity for ammonia synthesis, the electronic properties of Y_5Si_3 itself have not been fully understood yet. Another promising application of the electrides is ion storage and transport. Since the electrides structurally have a hollow space in which anionic electrons are distributed, it has been expected that those void space can be used for ion transport. Even before Y_5Si_3 was identified as an electride, experiments on hydrogenation of this material were conducted and showed very interesting results. From the experiment, as the hydrogen content x of $Y_5Si_3H_x$ increased, a rapid change in the hydrogen diffusion rate accompanied by an alteration in crystal structure was observed [28]. However, the exact mechanism of the hydrogenation process, which can explain the changes in the hydrogen diffusion rate and crystal structure, is still unknown.

In section 5.2, the structural and electronic properties of Y_5Si_3 as an elecride will be investigated in detail to understand how Y_5Si_3 can contribute to catalytic activity. The effect of vibrational modes on anionic electrons and interactions between metal atoms and Y_5Si_3 (001) surface will also be discussed. In section 5.3, the hydrogenation mechanism of $Y_5Si_3H_x$ will be systematically explored. I will investigate how the occupation sites of hydrogen atoms and diffusion barriers change as the hydrogen content increased. Penetration barriers of a hydrogen atom and molecule at the Y_5Si_3 (001) surface will also be discussed.

5.2 Structural and Electronic Properties of Y_5Si_3 as an Electride

In this section, I will take a closer look at the crystal and electronic structures of Y_5Si_3 in terms of electride. After qualitatively and quantitatively analyzing the presence of anionic electrons in the unit cell of Y_5Si_3, I will explore how vibrational modes affect the distribution of anionic electrons. Also, by examining the interaction between the Y_5Si_3 (001) surface and metal atoms, the electron-donating ability of Y_5Si_3 to adsorbates, which is a critical part of the catalytic activity, will be discussed.

5.2.1 Verification of the Presence of Anionic Electrons

As shown in Fig. 5.1 (a), the primitive unit cell of Y_5Si_3 consists of ten yttrium atoms and six silicon atoms corresponding to 2 formula units, and the Bravais lattice belongs to a hexagonal crystal system with a space group of $P6_3/mcm$ (#193). Three yttrium and three silicon atoms form a triangular ring in the a-b plane, and these triangular rings are stacked in the c-axis to build a 1D hollow space along the c-axis as shown in top view. This vacant space is what commonly seen from the electrides, which contains anionic electrons. As will be seen below, anionic electrons are distributed in this empty space. Qualitative analysis of the presence of anionic electrons is possible by looking at the projected band structure and DOS. Figure 5.1 (b) shows the projected band structure and DOS. In the band structure plot, the blue line represents contributions from the empty space between triangular rings composed of yttrium and silicon atoms, that is, anionic electron sites. In the DOS plot, contributions from each species and anionic electron sites are shown in different colors. The contributions from the void space to the band structure and DOS indicate the presence of electrons in those interstitial space, and these anionic electrons are distributed in

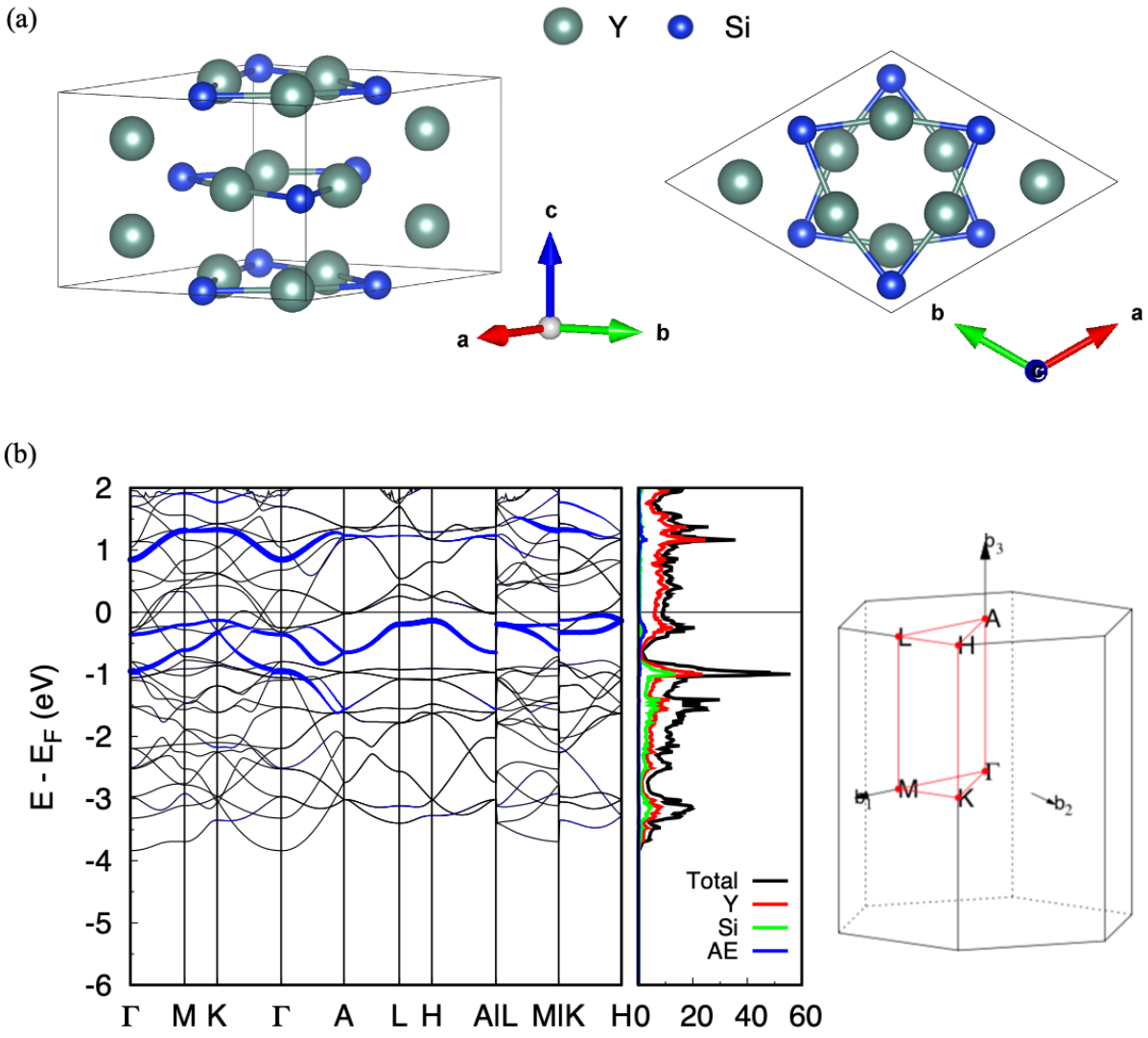


Figure 5. 1 Crystal and electronic structures of Y_5Si_3 (a) Crystal structure of Y_5Si_3 with hexagonal lattice symmetry (space group of $P6_3/mcm$). Three yttrium and silicon atoms form a triangular shape in the a-b plane, and these triangles form a 1D hollow space along the c-axis. (b) Atomically projected band structure and DOS. The blue lines in the band structure plot shows the contributions from the anionic electron (AE) site.

the energy range of -1.5 eV <$E-E_F$ < 0 eV, near the Fermi level. Another fact we can notice from the projected band structure is that the contribution of anionic electrons comes mostly from two bands, which corresponds to four electrons per unit cell. The reason why only one line is shown in the A-L-H-A path is that the two bands are degenerate. The Hosono group's report [26] claimed that anionic electrons were associated with a single band, while our study confirmed that two bands were related to anionic electrons.

Bader charge analysis was performed to quantitatively analyze the amounts of anionic electrons distributed in the vacant space, and the results are shown in Fig. 5.2 (a). Bader charge analysis was performed on the partial charge density corresponding to the energy range of -1.5 eV < $E-E_F$ < 0 eV, where anionic electrons are distributed. The red area in the figure on the left side shows the Bader volume containing anionic elections that have charge centers in the 1D hollow space. This figure clearly shows that electrons that are not bound to yttrium or silicon atoms are distributed in the empty space. The figure on the right side shows an integrated charge density along the c-axis inside the Bader volume containing the anionic electrons. It shows the maximum point of electron density in the center of the unit cell where no atom is located, and the amount of charge in this Bader volume is 1.488 electrons per formula unit. In other words, 2.976 of anionic electrons exist in the unit cell. This is almost twice the amount reported by Hosono's group [26], which is 0.79 e/f.u. These results are consistent with the fact that the two bands are related to the orbitals formed by anionic electrons. In Fig. 5.2 (b) a partial charge density distributed in the energy range of -0.5 eV < $E-E_F$ < 0 eV is visualized. To minimize noise from electrons bound to other atoms and effectively visualize the distribution of anionic electrons, a relatively narrow energy range was selected, and it can be confirmed that anionic electrons are distributed in a 1D hollow space in the center of the Y_5Si_3 lattice.

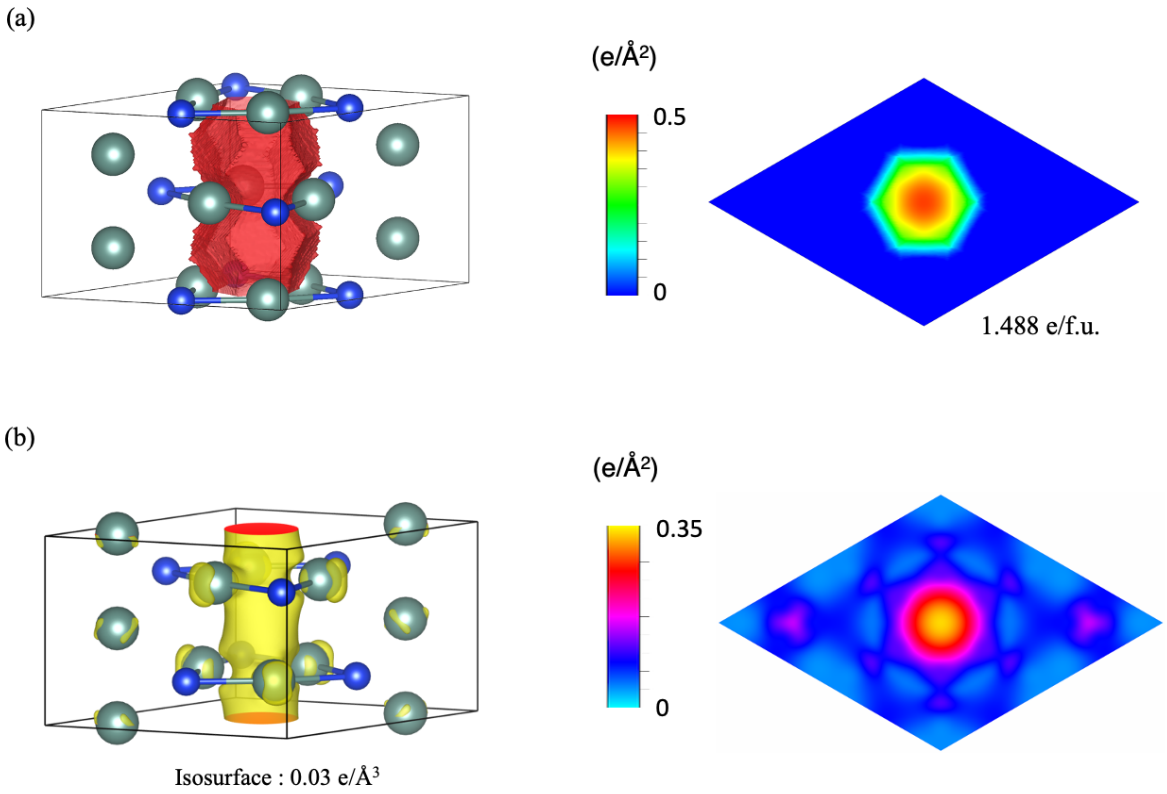


Figure 5. 2 Visualized anionic electrons. (a) Bader charge analysis is performed on a partial charge density (-1.5 eV < E-E_F < 0). The left figure shows a Bader volume for anionic electrons, and the right figure is an integrated charge density inside the Bader volume along the c-axis. The Bader volume contains 2.976 electrons, which is 1.488 per formula unit. (b) Distribution of a partial charge density (-0.5 eV < E-E_F < 0). Anionic electrons fill the 1D hollow space.

The DOS and band structures projected on each species and anionic electron sites are shown in Fig. 5.3 and 5.4 to examine the detailed interaction between electrons from the yttrium, silicon atoms, and the anionic electron sites. Considering symmetry by translation in the c-axis direction and rotation about the axis parallel to the c-axis and passing through the center of the a-b plane, symmetrically distinguishable sites are two yttrium atoms, one silicon atom, and anionic electron site (AE) as shown in Fig. 5.3 (a). Looking at Projected DOS (Fig. 5.3 (b)), it can be seen that the interaction between each site mainly occurs in three energy regions indicated with purple boxes. These interactions can be confirmed by examining the partial charge densities corresponding to each energy region. Partial charge densities for each energy region are shown in Fig. 5.3 (c). In the energy range of $-1.75\ \text{eV} < E\text{-}E_F < -1.25\ \text{eV}$, we can see that there is an interaction between Si1 and Y2 site, while an interaction between Si1 and Y1 site occurs in $-1.25\ \text{eV} < E\text{-}E_F < -0.75$ eV. Also, even though the projected DOS shows contributions from the Y1, Y2, and AE sites in the energy range of $-0.5\ \text{eV} < E\text{-}E_F < 0\ \text{eV}$, the corresponding partial charge density implies that there is an interaction between Y1 d orbitals and anionic electrons. The interaction between Y1 d orbitals and anionic electrons can be confirmed more clearly through the projected band structure to each site (Fig 5.4). In Fig. 5.4, comparing the projected bands of the AE site (blue lines) with those of the Y1, Y2, and Si1 sites, it can be seen that the Y1 d orbitals and anionic electrons contribute to the same bands, that is, there exists strong hybridization between Y1 d orbitals and anionic electrons. However, the projected bands of the Y2 site does not overlap with the bands associated with anionic electrons.

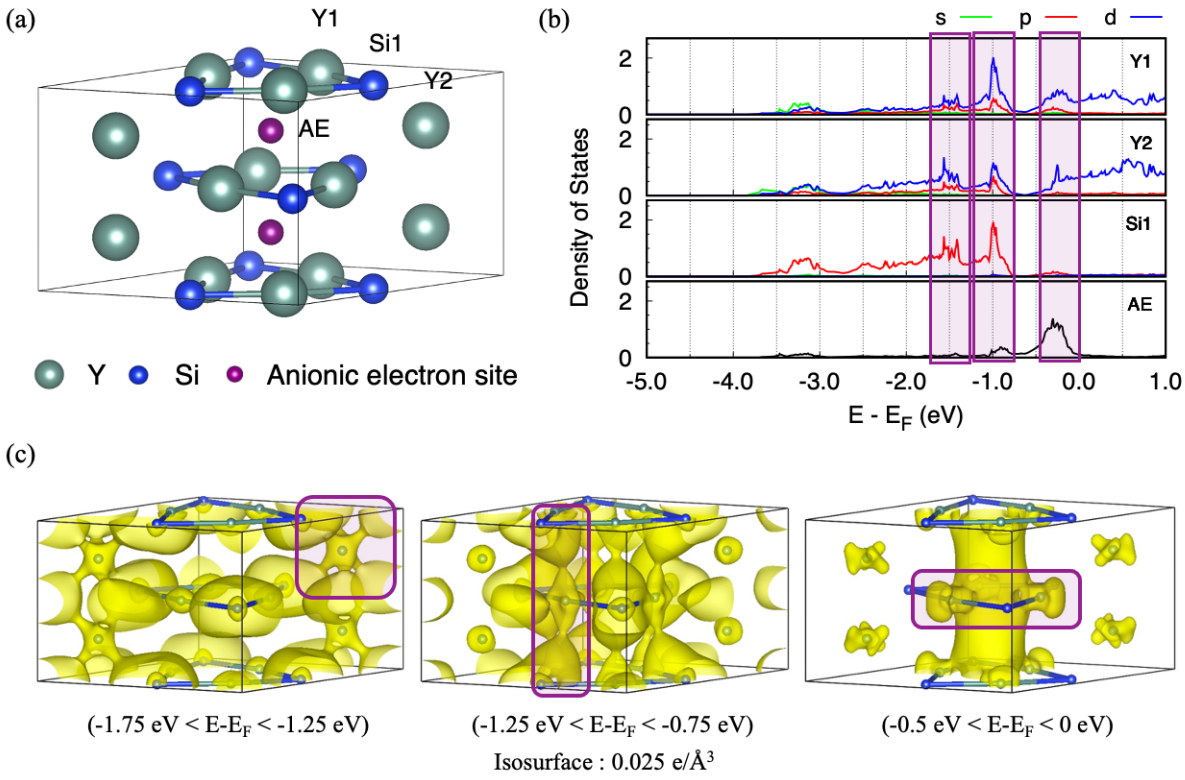


Figure 5. 3 Interactions between electrons from yttrium, silicon, and anionic electron site. (a) Symmetrically distinguishable atoms and anionic electron sites inside a unit cell. (b) Orbital projected DOS for each distinguishable atoms and anionic electrons. The purple boxes are indicating energy regions where interactions between each atom occur. (c) Partial charge densities of different energy ranges showing interactions between each atom and anionic electron.

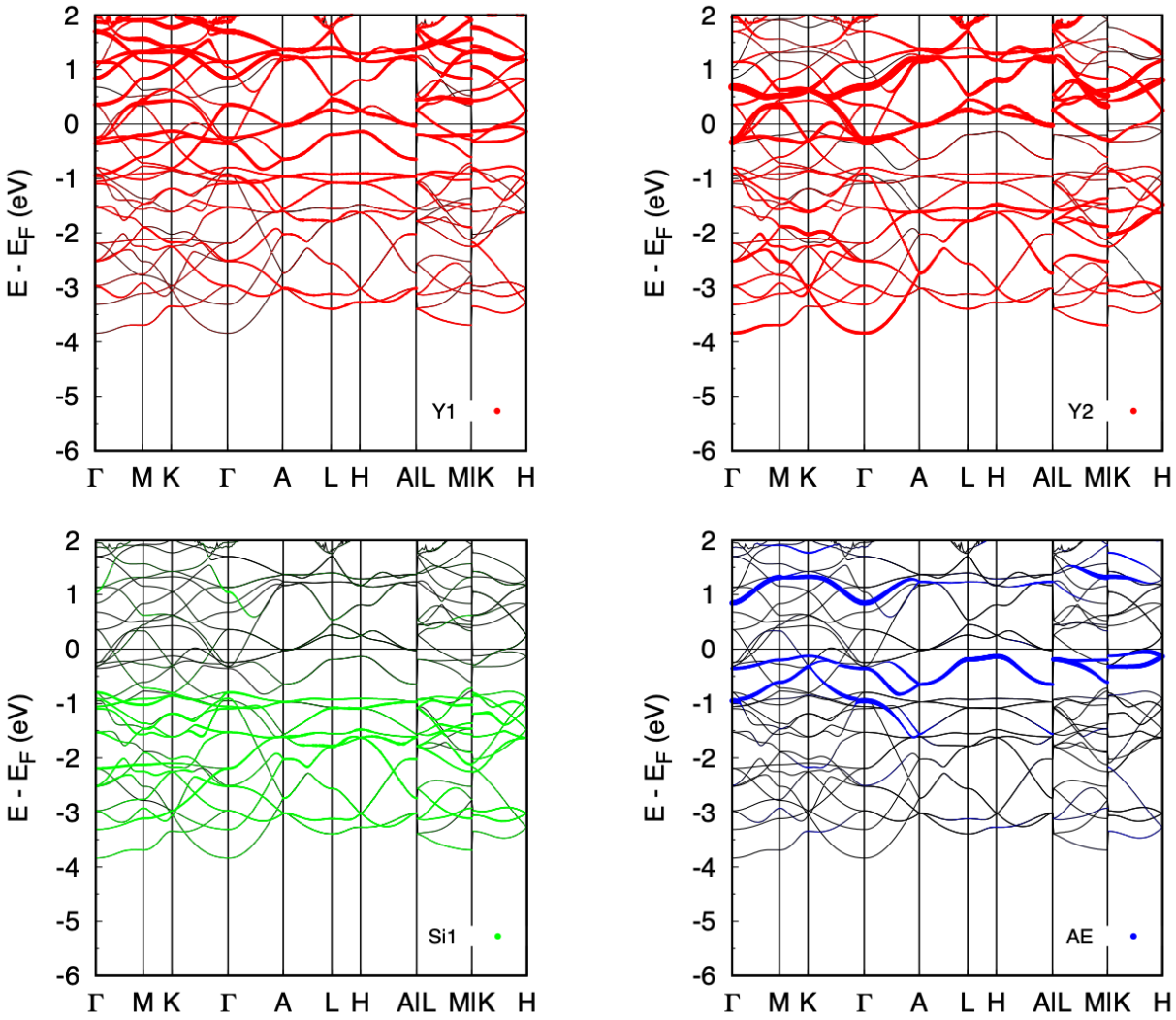


Figure 5. 4 Projected band structure for each distinguishable atoms and anionic electron sites.

5.2.2 Effect of Vibrational Modes on Anionic Electrons

As discussed earlier, anionic electrons in the Y_5Si_3 lattice are distributed in a 1D hollow space formed by stacking of triangular Y-Si rings in the c-axis direction. One of the factors that can affect the distribution of anionic electrons is the change in atomic positions due to lattice vibrations. To check whether the distribution of anionic electrons is affected by the lattice vibration, phonon dispersion relation was calculated, and the anionic electron density for several different atomic configurations caused by selected vibrational modes was investigated.

Phonon dispersion relation

Figure 5.5 shows the phonon dispersion relation obtained by DFT calculations and special k-points in the Brillouin zone. The wave vector determines the direction and wavelength of the lattice vibration that proceeds in the form of waves by the collective motion of the constituent atoms. A primitive unit cell composed of N atoms has a 3N degree of freedom and shows 3N phonon branches. Since the Y_5Si_3 primitive unit cell contains 16 atoms, there are 48 phonon branches, including 3 acoustic and 45 optical branches.

In the phonon dispersion relation in Fig. 5.5, each blue line represents these branches. The three branches converging to zero frequency at the Γ point correspond to those acoustic branches. To examine the effect of lattice vibration on the anionic electron distribution, I investigated how the low-frequency modes at Γ and A points change the atomic configuration, and thus the anionic electron density.

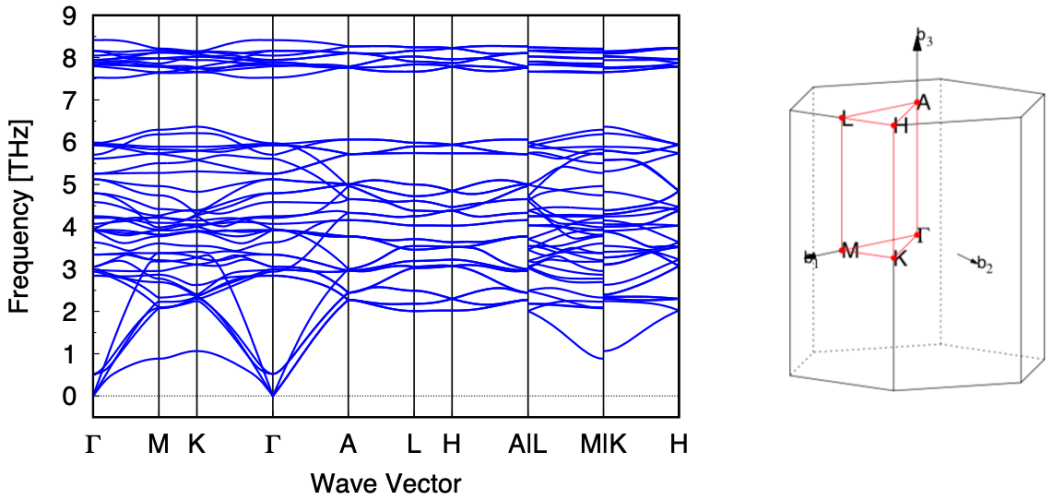


Figure 5. 5 Phonon dispersion relation and Brillouin zone of Y_5Si_3.

Vibrational modes at *Γ* point

The *Γ* point corresponds to the wave vector $k = 0$, and vibration modes at this point have an infinite wavelength. That is, identical atoms located in all unit cells exhibit the same movement. Since the three acoustic branches appearing at the A point represent translations in the *x*, *y*, and *z* directions, of course, they do not affect the relative atomic positions and anionic electron density in the lattice. Next, the optical branch appears at 0.52 THz, and two vibrational modes (4^{th} and 5^{th}) are degenerate in this branch, and the atomic configuration for each mode can be seen in Fig. 5.6. The yellow and blue triangles in the figure show the triangles created by the yttrium atoms that make up the Y-Si ring. The two triangles are spaced $c/2$ apart along the c-axis, and as seen from the top-view, they are twisted by $\pi/6$ to form a hexagram, also known as the star of David. The 4^{th} and 5^{th} modes at the *Γ* points show very similar vibrations. In both cases, rolling of Y-Si rings occurs about an axis laid in the a-b plane, and the axes for each mode are perpendicular to each other.

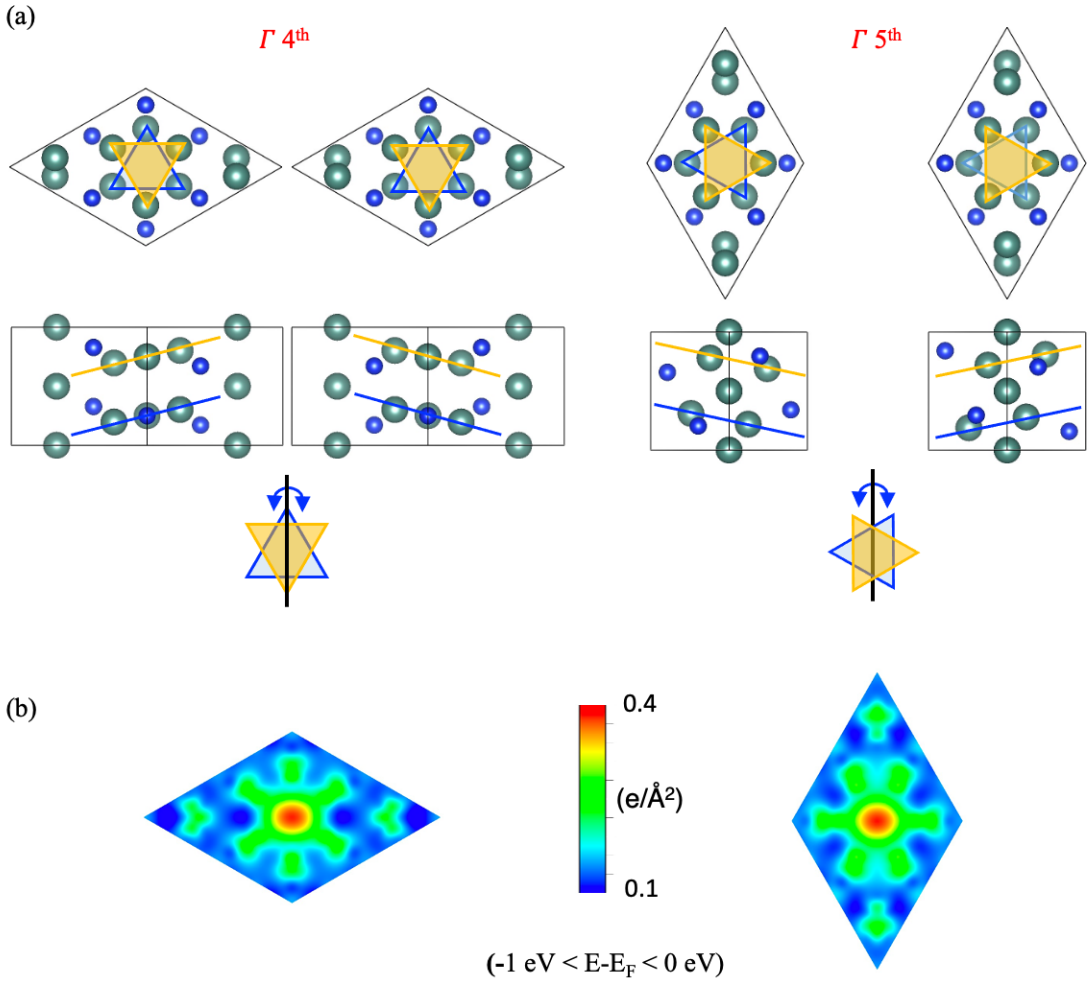


Figure 5. 6 4th and 5th vibrational modes at *Γ* point. (a) Atomic configurations and (b) corresponding partial charge densities in the energy range of -1 eV < $E-E_F$ < 0 eV for each vibrational mode.

The partial charge densities integrated along the c-axis are shown in Fig. 5.6 (b) and tell us that the distribution of anionic electrons located at the center of 1D hollow space is hardly affected by the deformed atomic configuration except that the circular shape is deformed into an ellipse.

Vibrational modes at *A* point

The A point corresponds to the wave vector $\vec{k} = \pi/c\ \hat{b}_3$ and is located at the Brillouin zone boundary. The wavelength of this wave vector is $2c$, and vibration modes at this point take a form of a standing wave. In other words, identical atoms in two adjacent unit cells along the c-axis move in opposite directions with the same amplitude. The lowest frequency phonon branch at the *A* point happens at 2.27 THz, and four vibrational modes are degenerate in this branch. The 1st and 3rd vibrational modes are illustrated in Fig. 5.7. The 2nd and 4th modes are identical with the 1st and 3rd modes respectively if the lattice is translated by $c/4$ along the c axis and rotated by π. In the figure, there are red, blue, and yellow triangles. As in the previous case, each triangle is formed by the yttrium atoms that make up the Y-Si ring. The yellow triangle is located in the nodal plane of the standing wave formed along the c-axis, so the change in atomic position hardly occurs, but the planes where the red and blue triangles lie will vibrate in opposite directions. The vibrations in the 1st and 3rd mode take place in directions perpendicular to each other. As in the case of the Γ point, partial charge densities near the Fermi level for both modes are shown in Fig. 5.7. The length of the simulation cell in the c-axis direction was doubled compared to the modes at the Γ point, so this was reflected in the scale bar. As shown in Figure 5.7 (b), it can be seen that although the shape of the anionic electron density is deformed from a circle to a triangular shape by these vibrational modes, the overall distribution is not significantly affected.

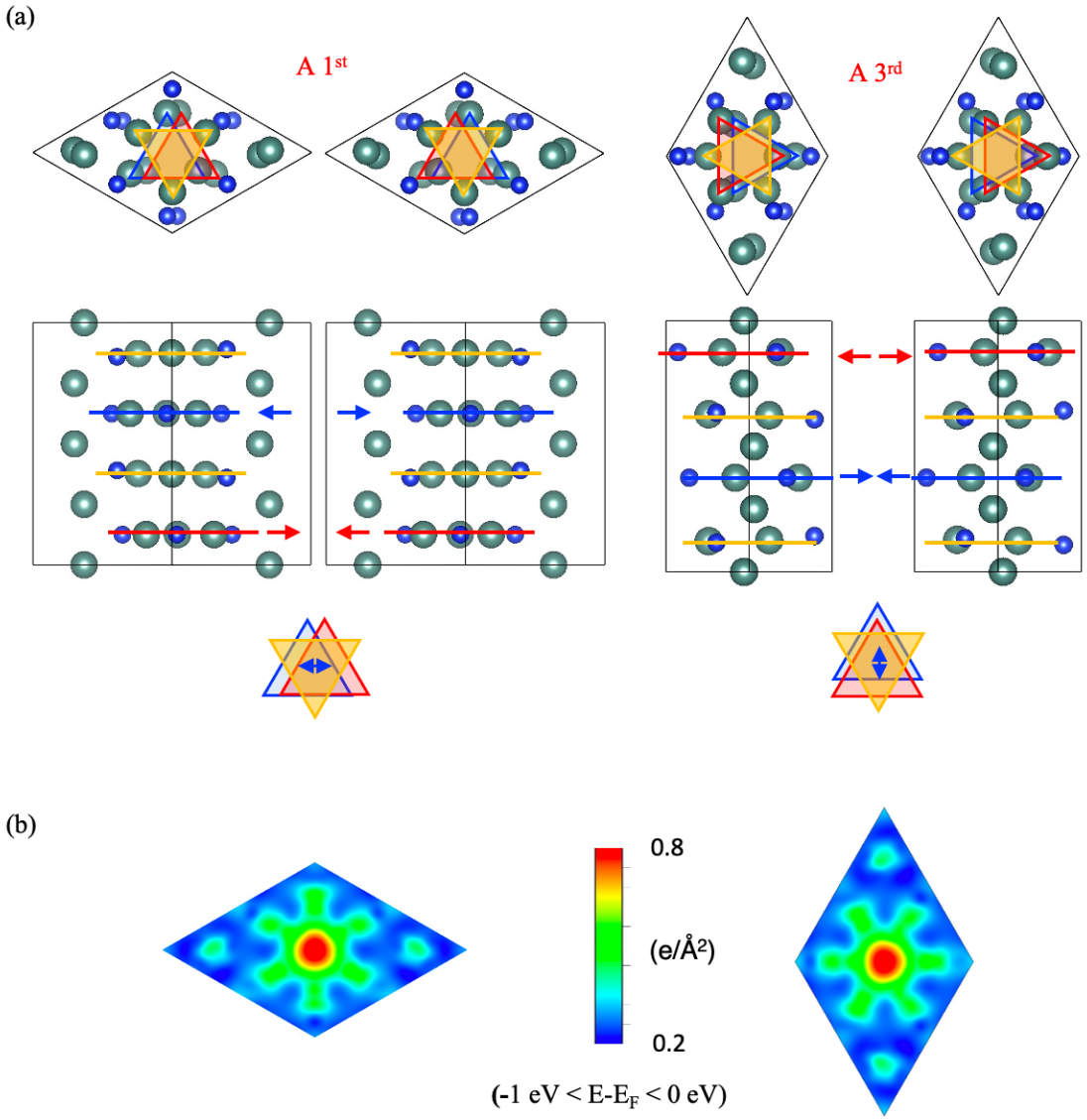


Figure 5. 7 1st and 3rd vibrational modes at *A* point. (a) Atomic configurations and (b) corresponding partial charge densities in the energy range of -1 eV < $E-E_F$ < 0 eV for each vibrational mode.

5.2.3 Electron-Donating Ability of Y_5Si_3 (001) Surface to Metal Atoms

So far, the characteristics of Y_5Si_3 as an electride were examined in detail by focusing on confirming the existence of anionic electrons. The property of anionic electrons, which are distributed near the Fermi level and are not strongly bound to any atom, means that the electrides are able to donate electrons to other systems readily. This electron-donating ability of the electrides suggests the possibility of being used as a catalyst. In fact, it has been reported by Hosono's group that the electrides such as $12CaO \cdot 7Al_2O_3$[27,125,134,135], Ca_2N [126,136], LnRuSi [127] can enhance the catalytic activity for direct ammonia synthesis by reducing activation energy of nitrogen dissociation. Y_5Si_3 is also one of those electride that can be used as a catalyst for the ammonia synthesis reported by the same group. [26] In all the literature mentioned above, electrides were used as a support for a Ruthenium catalyst, and the essential mechanism for the ammonia synthesis is the transfer of electrons from the electrides to Ruthenium atoms, where the dissociation of nitrogen molecules takes place. In this section, I verify the electron-donating ability of Y_5Si_3 in more detail by examining how charge transfer occurs through the interaction between the Y_5Si_3 (001) surface and various metal atoms. To investigate the interaction between the surface and various metal atoms, Y_5Si_3 (001) 1×1 surface slab was constructed first. The surface slab contains four layers of the Y-Si ring and terminates with those rings on both ends. After constructing the surface slab, a metal atom was placed on top of the outermost Y-Si ring, and the upper half of the slab and the metal atom were fully relaxed. The first way to visually check the charge transfer between the two materials is to look into the differential charge density. The visualized differential charge densities, shown in Fig. 5.8 is computed by using the below formula.

$$\Delta\rho = \rho[Y_5Si_3(001) + M]_{slab} - \rho[Y_5Si_3]_{slab} - \rho[M]_{atom}$$

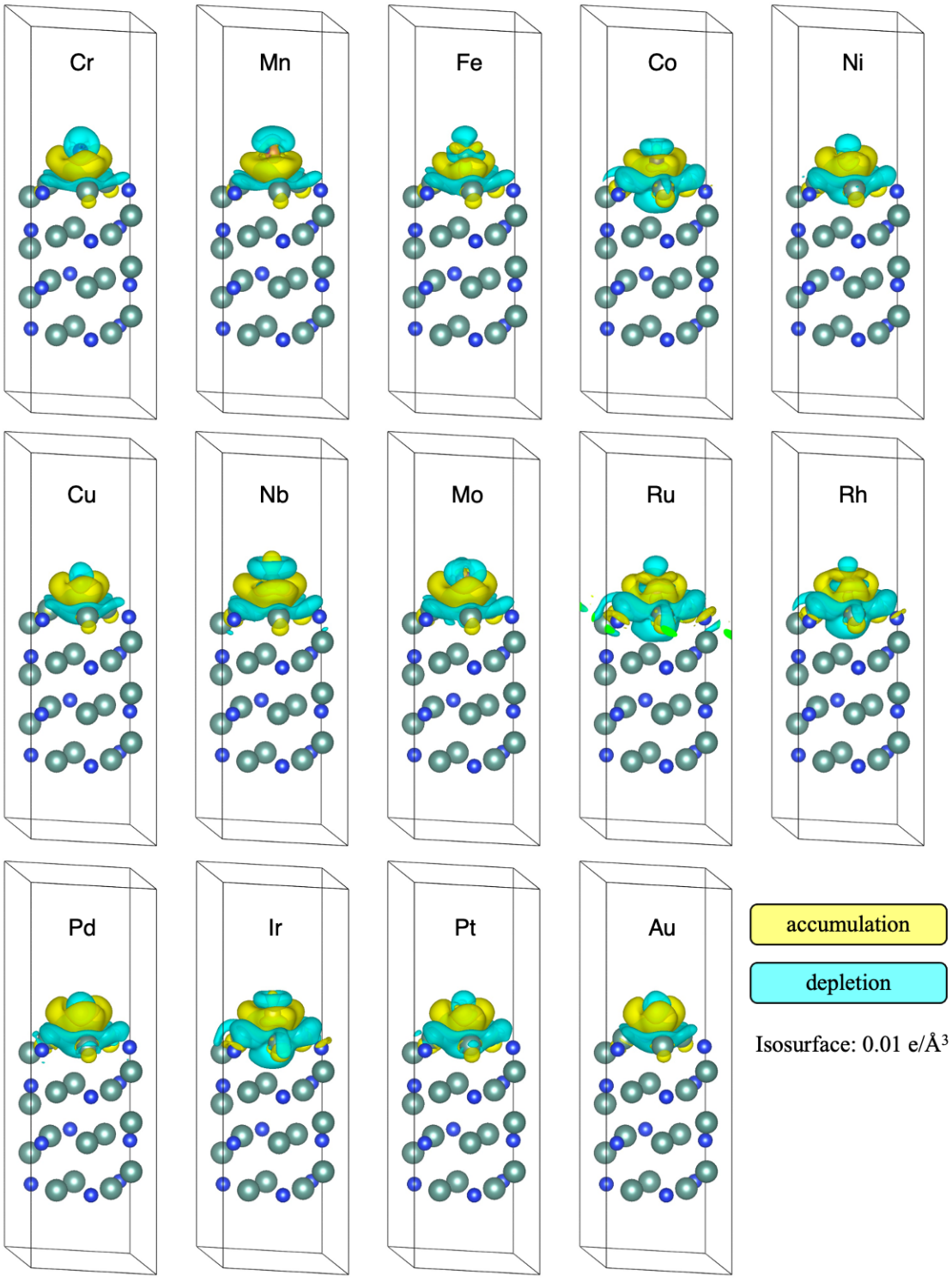


Figure 5. 8 Differential charge distribution of Y_5Si_3 (001) surface slab with metal atoms.

where, $\rho[Y_5Si_3(001)+M]_{slab}$ is the charge density of the fully relaxed Y_5Si_3 slab with the metal atom, and $\rho[Y_5Si_3(001)]_{slab}$, $\rho[M]_{atom}$ are the charge densities of the respective component where the atomic positions are the same with Y_5Si_3(001)+M. The first thing we can see in Fig. 5.8 is that charge transfer from the surface to the metal atom occurs for every considered metal atom. We need to note that electrons that accumulate on the metal atom do not come from yttrium or silicon atoms located on the outermost surface, but electrons distributed on the surface. This indicates that anionic electrons that were distributed between neighboring triangular Y-Si rings are still distributed on the surface even after the surface cleavage, and those electrons can be readily transferred to the metal atoms. The second thing to note is that, for some metal atoms, only these surface electrons migrate to the metal atom, but another charge depletion also occurs at the anionic electron site inside the surface for other metal atoms. The latter happens in the cases of Co, Ni, Ru, Rh, Pd, Ir, and Pt. To quantitatively analyze the amounts of electrons transferred from the Y_5Si_3 (001) surface to each metal atom, Bader charge analysis was performed, and the results are shown in Fig. 5.9 compared to the electron affinity of each metal atom. The electron affinity is defined as the amount of decrease in energy when a neutral atom absorbs an electron, and this value can be used as a measure of how easily an electron can be added to a neutral atom.

It is necessary to note that the Bader charge analysis is a method of determining the number of electrons allocated to each atom based on the geometrical distribution of electrons. Therefore, it is not possible to determine the exact charge state of each atom, but it is sufficient to confirm the general trend for charge transfer. As shown in Figure 5.9, the amounts of electrons transferred from the surface to each metal atom tend to be proportional to electron affinity. However, in the case of Co, Ni, Ru, Rh, Pd, Ir, and Pt atoms mentioned above, it can be seen that relatively large amounts of electrons are transferred to the metal atom. This confirms the fact that the anionic

electron inside the surface is transferred to these metal atoms. According to the data reviewed so far, the electron-donating property of the Y_5Si_3 (001) surface varies depending on the type of adsorbed metal atoms, and the difference is whether or not anionic electrons inside the surface can be extracted. Now we need to look at what causes this difference. Table 5.1 summarizes the electron configuration and estimated amounts of transferred charge for each atom.

Metal atoms that exhibit charge depletion at the anionic electron site inside the surface in the differential charge densities shown in Fig. 5.8, are indicated with red color and marked with an asterisk. As can be seen from the amount of transferred charge shown in the table, metal atoms marked with asterisk show relatively high values compared to other atoms. The commonality shown in the electron configuration of these atoms is that they have a small number of unpaired vacancies for the d orbital occupation.

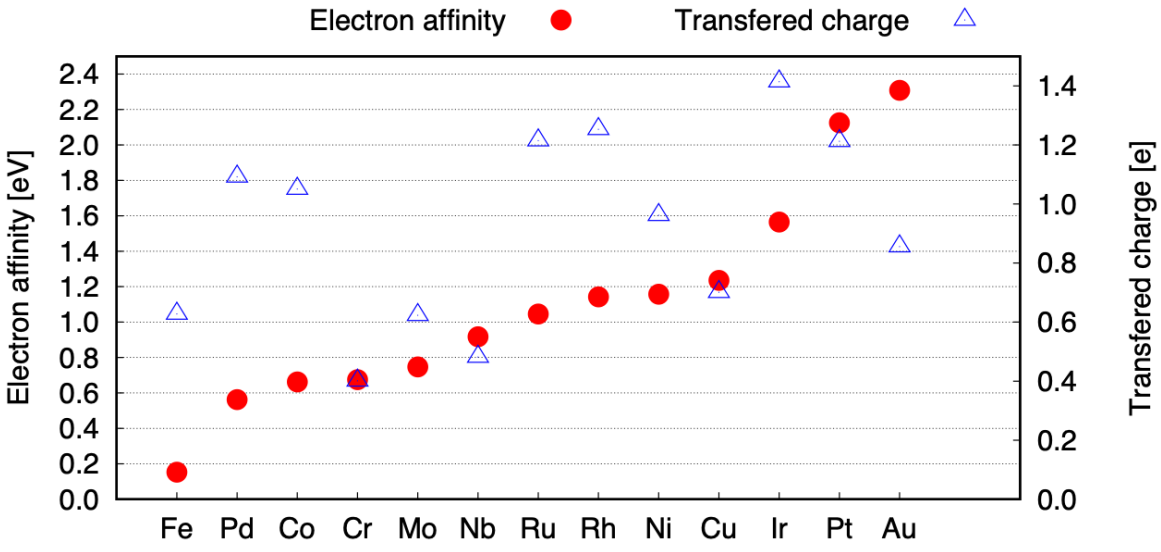


Figure 5. 9 Correlation between electron affinity and amount of transferred charge from Y_5Si_3 (001) surface to metal atoms.

Table 5. 1 Electron configurations and amount of transferred charge for various metal atoms.

Adsorbate	Electron configuration	Transferred charge (e)
Cr	[Ar] 3d5 4s1	0.401
Mn	[Ar] 3d5 4s2	0.435
Fe	[Ar] 3d6 4s2	0.628
Co *	[Ar] 3d7 4s2	1.051
Ni *	[Ar] 3d9 4s1	0.962
Cu	[Ar] 3d10 4s1	0.701
Nb	[Kr] 4d4 5s1	0.481
Mo	[Kr] 4d5 5s1	0.623
Ru *	[Kr] 4d7 5s1	1.214
Rh *	[Kr] 4d8 5s1	1.253
Pd *	[Kr] 4d10	1.092
Ir *	[Xe] 4f14 5d7 6s2	1.414
Pt *	[Xe] 4f14 5d9 6s1	1.212
Au	[Xe] 4f14 5d10 6s1	0.856

In the case of Pd, even though d orbitals are all filled, but since s orbital is empty, it seems to show a similar trend. Additional investigation of the interaction between the d orbitals of metal atoms and the anionic electrons of Y_5Si_3 is required to clearly understand these phenomena associated with charge transfer on Y_5Si_3 (001) surfaces.

5.2.4 Crystal and Electronic Structures of Y_5X_3 (X = Si, Ge, Sn, and Pb)

So far, the structural and electronic properties of Y_5Si_3 as an electride have been examined. One question we may have here is what changes can be made to the properties of electride when Si species is replaced with other elements of group 14. To answer this question, Si atoms are replaced with Ge, Sn, and Pb, and structural and electronic properties were examined.

Before investigating their properties, global structure optimization was performed to check whether the same structure as that of Y_5Si_3 can be the most stable for each chemical composition even when Si atom is replaced with another species, and the results are summarized in Table 5.2. Table 5.2 shows the space groups of four (meta)stable structures, and relative energy values compared to the most stable structure for each chemical composition. In all cases of Ge, Sn, and Pb, including Y_5Si_3, the structure with $P6_3/mcm$ space group belonging to the hexagonal crystal system was identified as the most stable structure and showed an energy difference of 60 meV/atom or more with other metastable structures.

Table 5. 2 Stable structures and corresponding energies for Y_5Si_3 (X = Si, Ge, Sn, and Pb) identified through crystal structure search.

	Space group [Relative energy (eV/atom)]			
	Y_5Si_3	Y_5Ge_3	Y_5Sn_3	Y_5Pb_3
1	$P6_3/mcm$ (#193) [0.000]	$P6_3/mcm$ (#193) [0.000]	$P6_3/mcm$ (#193) [0.000]	$P6_3/mcm$ (#193) [0.000]
2	$P\bar{1}$ (#2) [0.061]	I4/mcm (#140) [0.096]	C2/c (#15) [0.068]	Cmcm (#63) [0.113]
3	$P\bar{1}$ (#2) [0.072]	$P\bar{1}$ (#2) [0.107]	I4/mcm (#140) [0.082]	P2_1/m (#11) [0.116]
4	$P\bar{1}$ (#2) [0.089]	C2/c (#15) [0.114]	Cmcm (#63) [0.125]	P2_1/m (#11) [0.127]

This result implies that the same structure can be synthesized even if the Si atom is replaced with other group 14 elements in Y_5Si_3. Figure 5.10 shows the most stable structure for each chemical composition. They all show the identical atomic configuration, exhibiting the same triangular Y-X ring in the a-b plane. The specific changes in structural parameters resulting from replacing Si atom with other species are shown in the graphs in Fig. 5.11. As the atomic number of the X atom increases, the length of lattice vectors a and c gradually increases, and accordingly, the volume also increases. If we look at the ratio of lattice parameters a and c, Ge shows a similar ratio with Y_5Si_3, but in the case of Sn and Pb, the length of a increases more than the length of c, so that the expansion in the a-b plane is further intensified. Therefore, the distance between the yttrium atoms constituting the Y-X ring shows a similar trend.

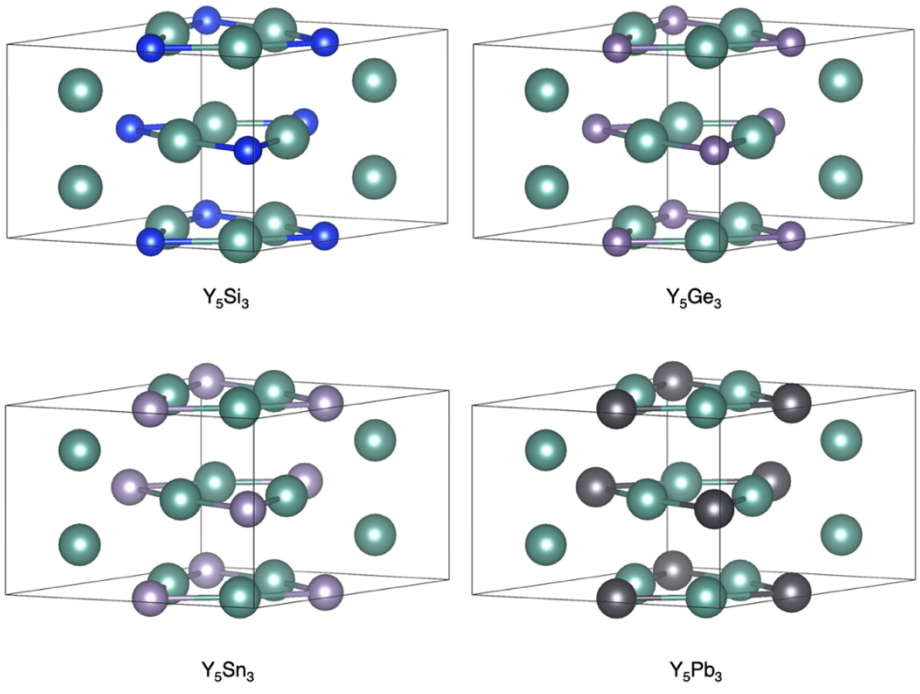


Figure 5. 10 Crystal structures of Y_5X_3 (X=Si, Ge, Sn, and Pb). They all show the identical atomic configuration belonging to the hexagonal crystal system with a space group of $P6_3/mcm$ (#193).

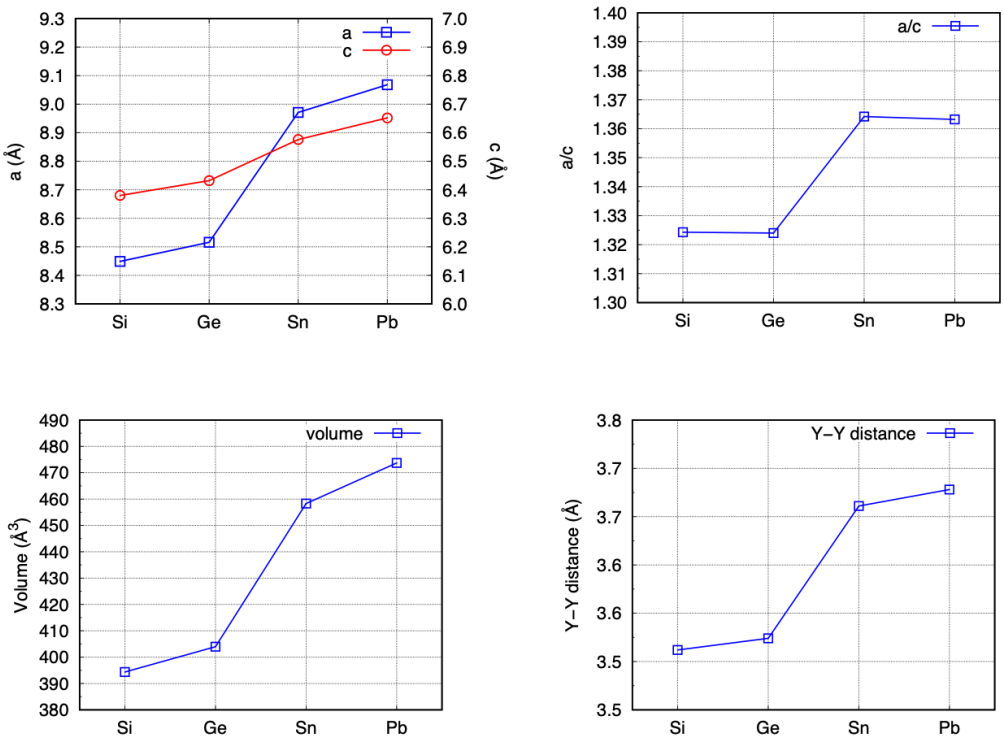


Figure 5. 11 Changes of structural parameters of Y_5X_3 (X=Si, Ge, Sn, and Pb). Y-Y distance means the distance between yttrium atoms that build the triangular ring in the a-b plane.

So far, I have examined structural changes caused by the substitution of Si atom with other elements, but our primary concern is whether these chemical compositions exhibit the same electronic properties as Y_5Si_3 containing anionic electrons inside the vacant space. Figure 5.12 shows the projected band structure and DOS calculated for each chemical composition, and the blue color in each graph indicates the contributions from the 1D hollow space, i.e., anionic electron sites. These plots for four different chemical compositions show almost identical results. In all cases, it can be seen that anionic electrons mostly contribute to two bands located in the energy range of -1.5 eV < $E-E_F$ < 0 eV near the Fermi level. The amounts of anionic electrons calculated through the Bader charge analysis are 1.49 (Y_5Si_3), 1.47 (Y_5Ge_3), 1.46 (Y_5Sn_3), and 1.27 (Y_5Pb_3) electron per formula unit, that do not show much difference.

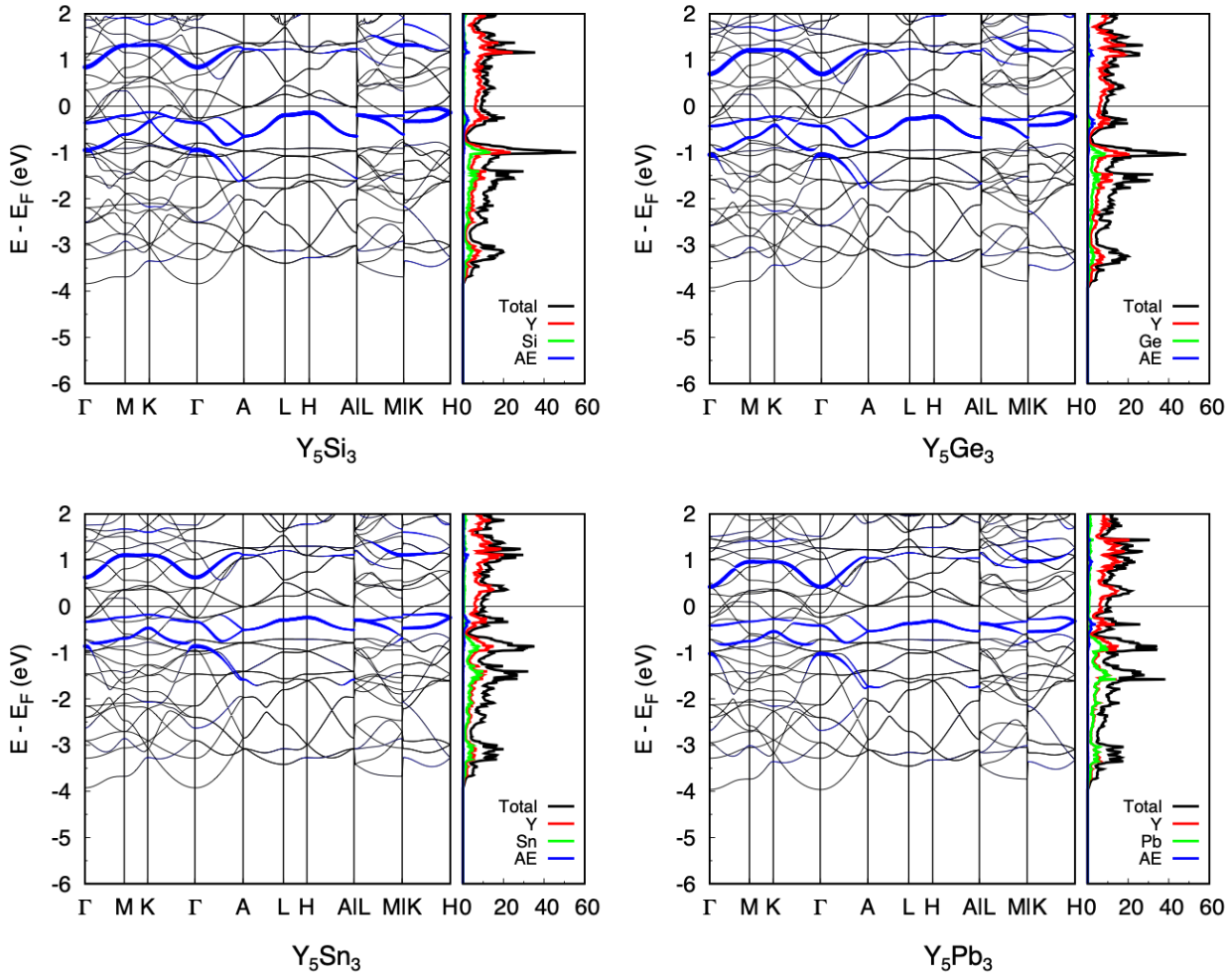


Figure 5. 12 Projected band structure and DOS of Y_5X_3 (X=Si, Ge, Sn, and Pb). The projected band structure shows contributions only from anionic electron sites.

5.3 Hydrogenation of Y_5Si_3

The following steps are required to understand and explain the hydrogenation mechanism of Y5Si3. 1) When the hydrogen atom is absorbed into Y_5Si_3, it is necessary to know where it can be stably located, that is, the stable occupation sites of the hydrogen atom. 2) When hydrogen contents x in $Y_5Si_3H_x$ increases as hydrogenation progresses, we need to know how the insertion of hydrogen atoms changes the entire crystal structure. 3) A favorable diffusion path should be identified by estimating diffusion barriers between each occupation site. 4) Finally, we need to check the penetration barrier of hydrogen through the surface of Y_5Si_3 to complete the discussion. In this section, the hydrogenation mechanism of Y_5Si_3 will be discussed according to the above procedure.

5.3.1 Stable Configurations of $Y_5Si_3H_x$ ($0.5 \leq x \leq 8$)

As a first step in understanding the hydrogenation of Y_5Si_3, a restricted crystal structure search was used to find (meta)stable configurations for the chemical composition of $Y_5Si_3H_x$. During the structure search, the structure of the parent Y_5Si_3 was fixed, and hydrogen atoms were randomly inserted into the Y_5Si_3, followed by relaxation of the entire structure to reach locally optimized configuration, as shown in Fig. 5.13. By repeating this process at least 300 times for different hydrogen contents, (meta)stable configurations of $Y_5Si_3H_x$ were identified.

$Y_5Si_3H_{0.5}$

Figure 5.14 shows identified locally stable configurations of $Y_5Si_3H_{0.5}$ and relative energy differences between those structures. There is one hydrogen atom in the unit cell. Structures other

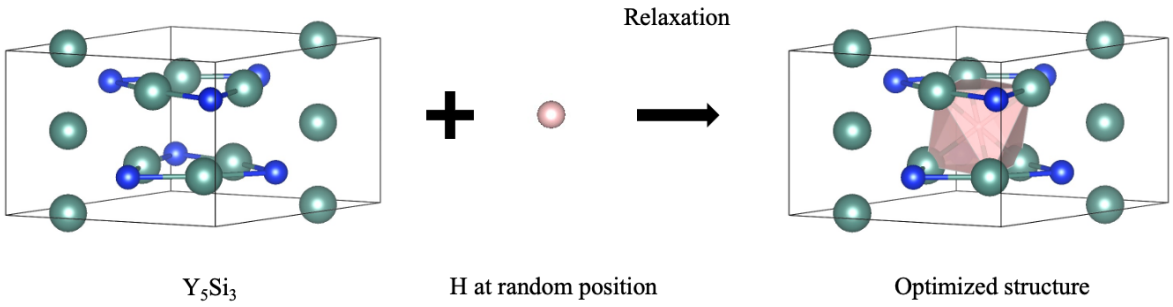


Figure 5. 13 Restricted crystal structure search for identifying stable hydrogen occupation sites of $Y_5Si_3H_{0.5}$.

than the five occupation sites shown in Fig. 5.14 were not identified, and thus the figure shows all possible locations for hydrogen occupation. In the case of the site 1, the most stable site, the hydrogen atom is located in the 1D hollow space where anionic electrons are distributed, while in the other four cases, the hydrogen atom is located outside the 1D vacant space. The site 1 is an octahedral site surrounded by six yttrium atoms, and the site 2 is also an octahedral site surrounded by five yttrium and one silicon atoms. Site 3, 4, and 5 form a hexahedron with three yttrium and two silicon atoms at vertices. There is an energy difference of 0.75 eV between site 1 and site 2, but a relatively small energy differences of less than 0.25 eV between site 2 ~ site 5.

The projected band structure and DOS were investigated to examine the effect of the hydrogen atom inserted at each site on the electronic structure, and they are shown in Fig. 5.15. The first thing we can notice from Fig. 5.15 is that, for all sites, a new electronic band emerges around -5 eV by hydrogen insertion. The formation of this new band indicates that the hydrogen atom absorbs one electron from Y_5Si_3 and becomes H^- ion. The second thing to look at is the effect of the inserted hydrogen atom on the anionic electrons. In this respect, site 1 and the rest of the hydrogen sites are in different situations. Compared with the Y_5Si_3 projected band structure, it can be seen that, in the case of site 1, one of the two bands associated with anionic electrons disappears, but in the

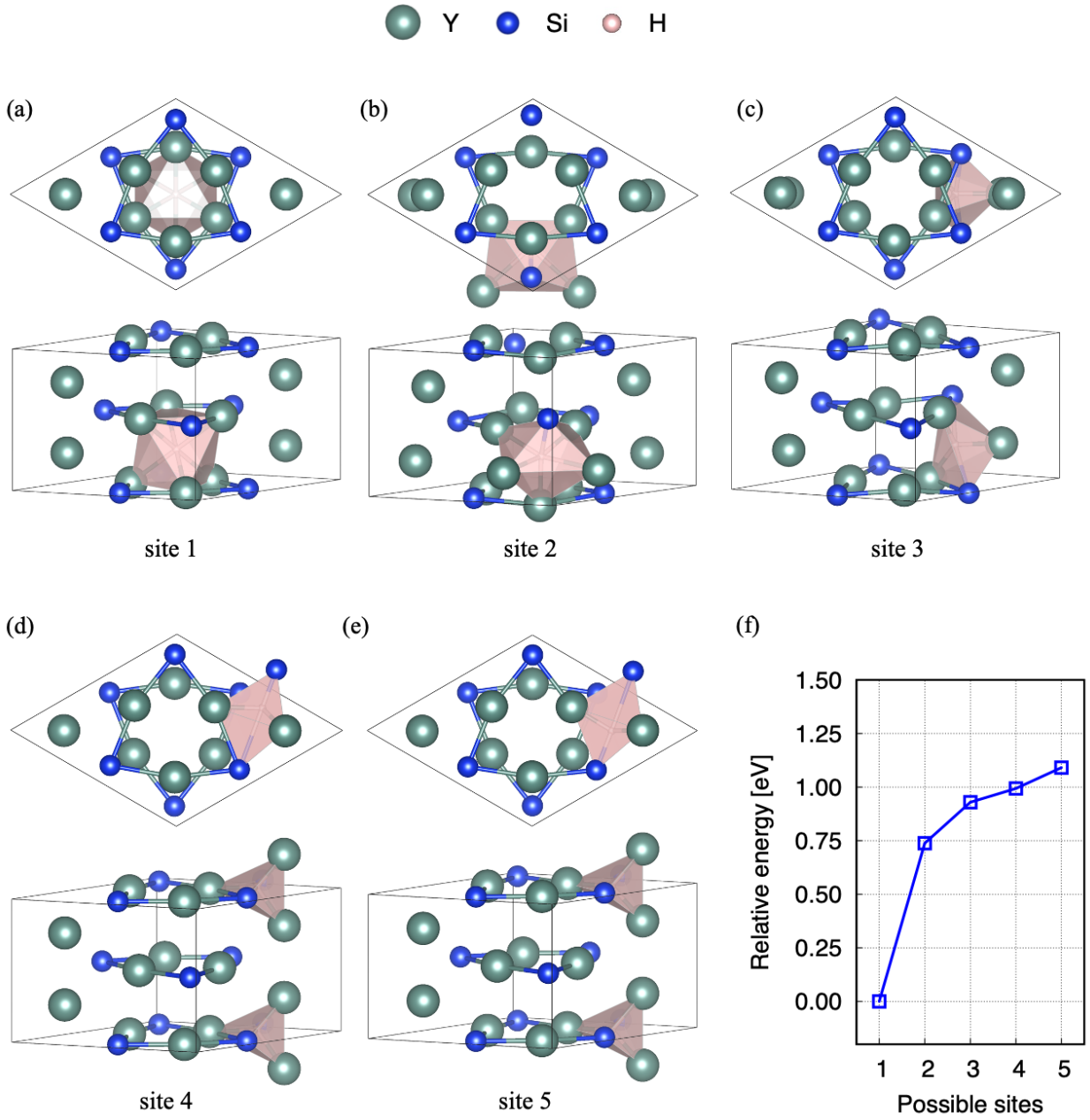


Figure 5. 14 Stable configurations of $Y_5Si_3H_{0.5}$ identified through crystal structure search. (a) ~ (e) Crystal structures of $Y_5Si_3H_{0.5}$ which contain one hydrogen atom in a unit cell. (f) Relative energy differences of identified configurations.

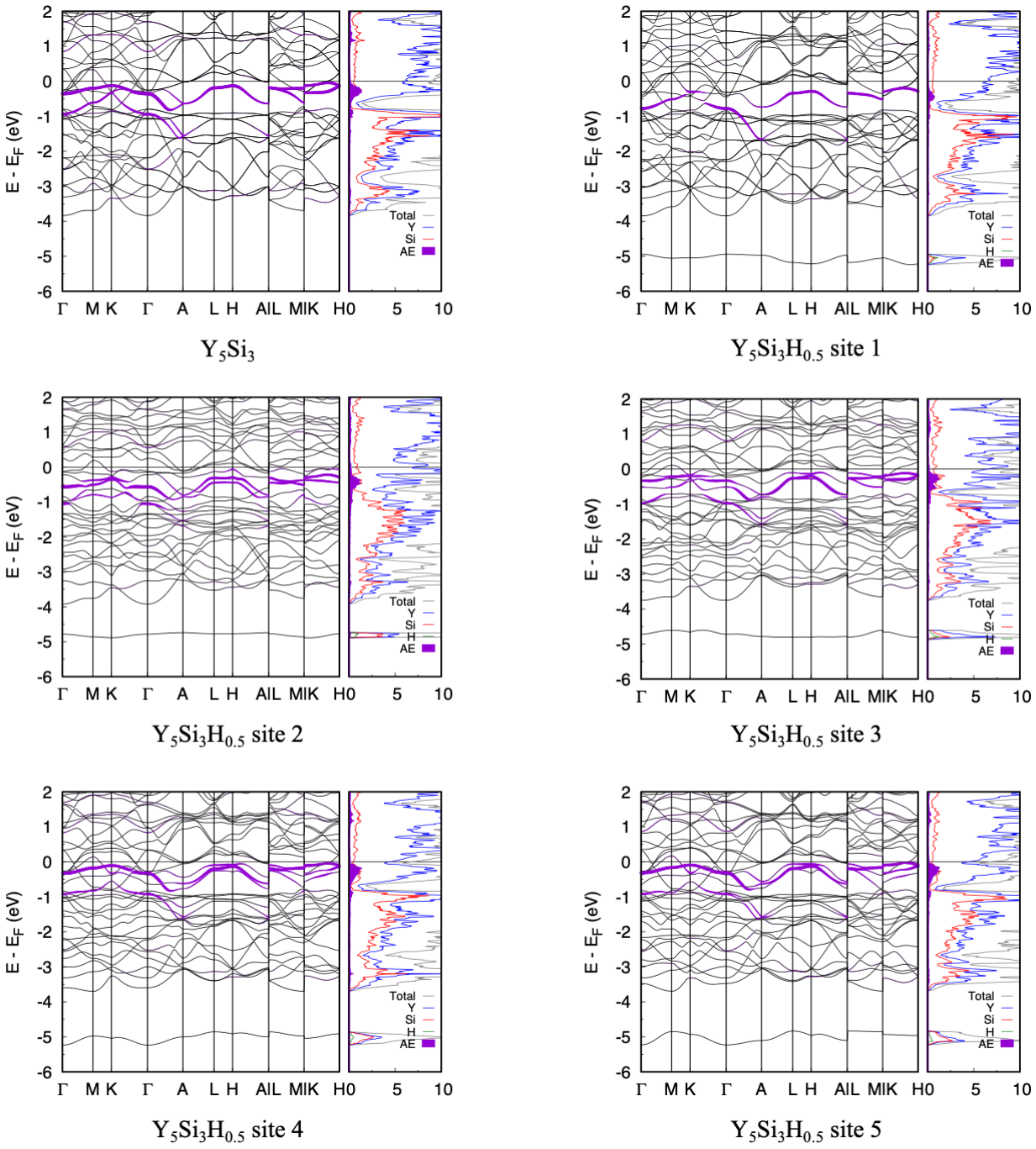


Figure 5. 15 Projected band structures and DOS of Y_5Si_3 and possible configurations of $Y_5Si_3H_{0.5}$ identified through crystal structure search. Contribution from the anionic electrons is indicated in purple color.

other cases, two bands are maintained without significant changes. That is, when the hydrogen atom is located at site 1, it absorbs anionic electrons distributed in the 1D vacant space and becomes H^- ion, but for other sites, it does not have a significant effect on anionic electrons except for a small deformation of the bands. The effect of the inserted hydrogen on the anionic electrons can be more clearly understood by looking at the partial charge densities near the Fermi level shown in Fig. 5.16. As shown in the figures, other sites except for site 1 do not significantly affect the distribution of anionic electrons filling the 1D hollow channel centered on the lattice. However, in the case of site 1, we can notice that the anionic electrons inside the octahedron, where the hydrogen atom is located, disappear. This is consistent with the loss of one anionic electron band in the projected band structure of site 1 in Fig. 5.15. The calculated amount of Bader charge for anionic electrons written next to the integrated partial charge density also confirms that the quantity of anionic electrons is reduced by half only in the case of site 1 from 1.488 to 0.746 e/f.u. Lastly, it is necessary to notice the shift of the Fermi level occurring in the band structure of site 1. If we look at the band structure, especially near the A point, we can realize that the Fermi level slightly goes up compared to Y_5Si_3. This phenomenon indicates that the amounts of electrons occupying metallic bands across the Fermi level increases. This phenomenon is caused by the difference between the number of disappearing anionic electrons and the number of electrons absorbed by hydrogen. The disappearance of one anionic electron band means that two electrons have transitioned to another state, of which one electron is absorbed by a hydrogen atom. Then, extra anionic electron that is not absorbed by the hydrogen atom moves to metallic bands, which increases the Fermi level. The differential charge density drawn in Fig. 5.17 shows this phenomenon more clearly. The differential charge density shows regions of charge accumulation and depletion due to charge transfer inside the unit cell.

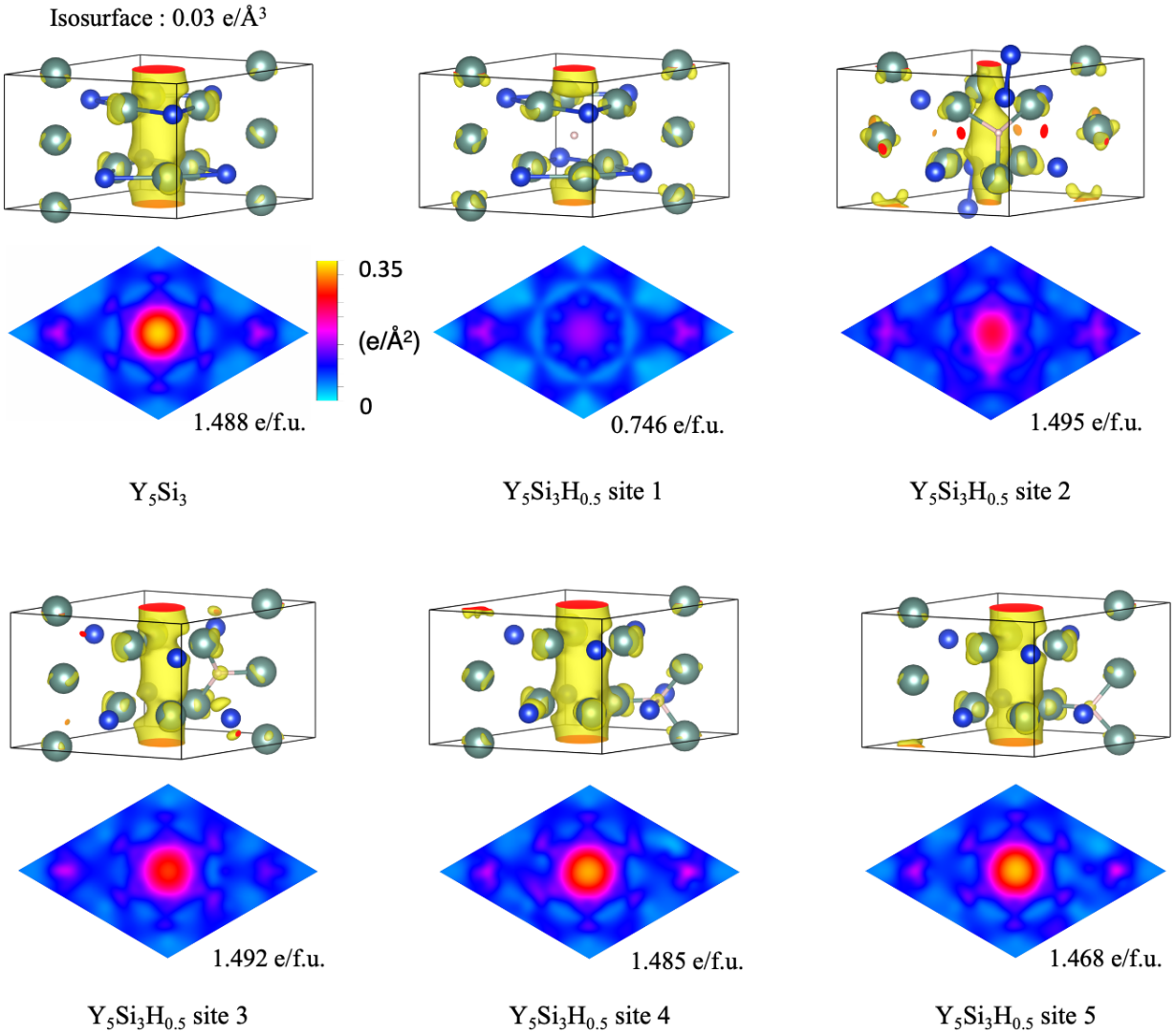


Figure 5. 16 Partial charge density of possible configurations of Y_5Si_3 and $Y_5Si_3H_{0.5}$ identified through crystal structure search. 3D and integrated (along c-axis) partial charge density in the energy range of -0.5 eV < E-E_F < 0 are drawn. Amount of the Bader charges of the anionic electrons are calculated from partial charge density in the energy range of -1.5 eV < E-E_F < 0.

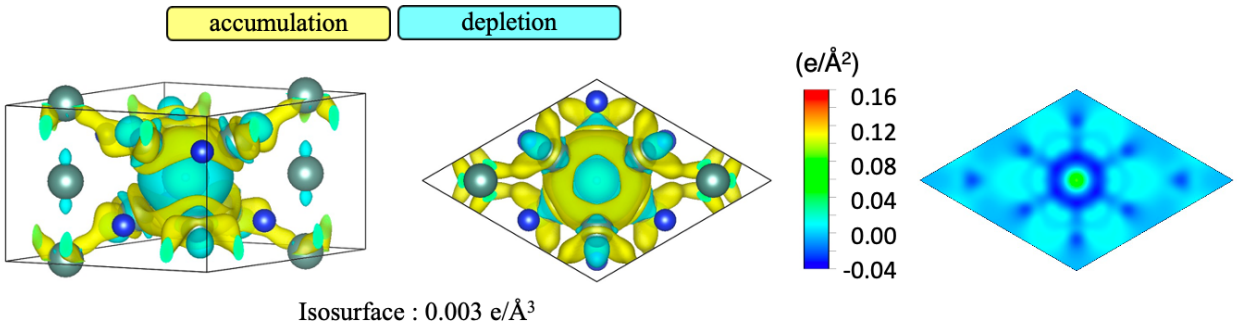


Figure 5. 17 Differential charge density due to the insertion of a hydrogen atom into the site 1 of $Y_5Si_3H_{0.5}$.

The differential charge density was calculated by applying the below formula.

$$\Delta\rho = \rho[Y_5Si_3H_{0.5}] - \rho[Y_5Si_3] - \rho[H]$$

$\rho[Y_5Si_3H_{0.5}]$ is the charge density of fully relaxed $Y_5Si_3H_{0.5}$, and $\rho[Y_5Si_3]$, $\rho[H]$ are the charge densities of respective component where the atomic positions are the same with $Y_5Si_3H_{0.5}$. Electron depletion occurring near the hydrogen atom and at the proximity of six yttrium atoms corresponds to the disappeared band in the projected band structure of site1 shown in Fig. 15.5, which is the hybridized band between the anionic electron and the d orbital of the adjacent yttrium atoms. One of these disappeared electrons is absorbed by the hydrogen atom in the center of the octahedron, and the other electron escapes from the anionic electron site and goes into other spaces outside the octahedron. From the integrated differential charge density along the c-axis shown on the right side of Fig. 5.17, we can also notice that electrons escape from the depletion region (blue) inside the octahedron and transferred to the hydrogen atom (green) in the center of the lattice and the outside the 1D hollow space (cyan).

The last thing to look at for the chemical composition of $Y_5Si_3H_{0.5}$ is an asymmetric change in anionic charge density caused by the hydrogen atom occupying site 2. As discussed above, hydrogen occupation in sites other than site 1 does not significantly affect the band of anionic electrons or the number of anionic electrons calculated through Bader charge analysis. However, in the case of site 2, a noticeable asymmetric deformation happens in the distribution of anionic electrons, as shown in Fig 5.18 (b) and (d). Site 2 is an octahedral site surrounded by five yttrium and one silicon atoms. This octahedron shares its face with the octahedral anionic electron site in the center of the lattice (Fig. 5.18 (a)). The differential charge density (Fig 5.18 (c) and (e)) shows that the hydrogen atom located at site 2 becomes an H^- ion by absorbing electrons from adjacent yttrium atoms and the surrounding space. Therefore, the deformations of the distribution of anionic electrons shown in Fig. 5.18 (b) and (d) can be thought to be caused by Coulomb repulsion between neighboring anionic electrons and the H^- ion.

$Y_5Si_3H_1$

$Y_5Si_3H_1$ contains two hydrogen atoms in the unit cell, and Fig. 5.19 shows identified locally stable configurations of $Y_5Si_3H_1$ and relative energy differences between those structures. In all cases except for configuration 2, two hydrogen atoms are located at occupation sites identified in the case of $Y_5Si_3H_{0.5}$, and the location of the hydrogen atoms are summarized in Table 5.3.

The energy differences between possible configurations are determined by the occupation site of the second hydrogen atom since the first hydrogen atoms are located at site 1, except for 2. Interestingly, the second most stable configuration 2 shows that two hydrogen atoms can exist together in a single site 1, indicating that the hydrogen atoms prefer to stay in the 1D hollow space even though they are concentrated at one site.

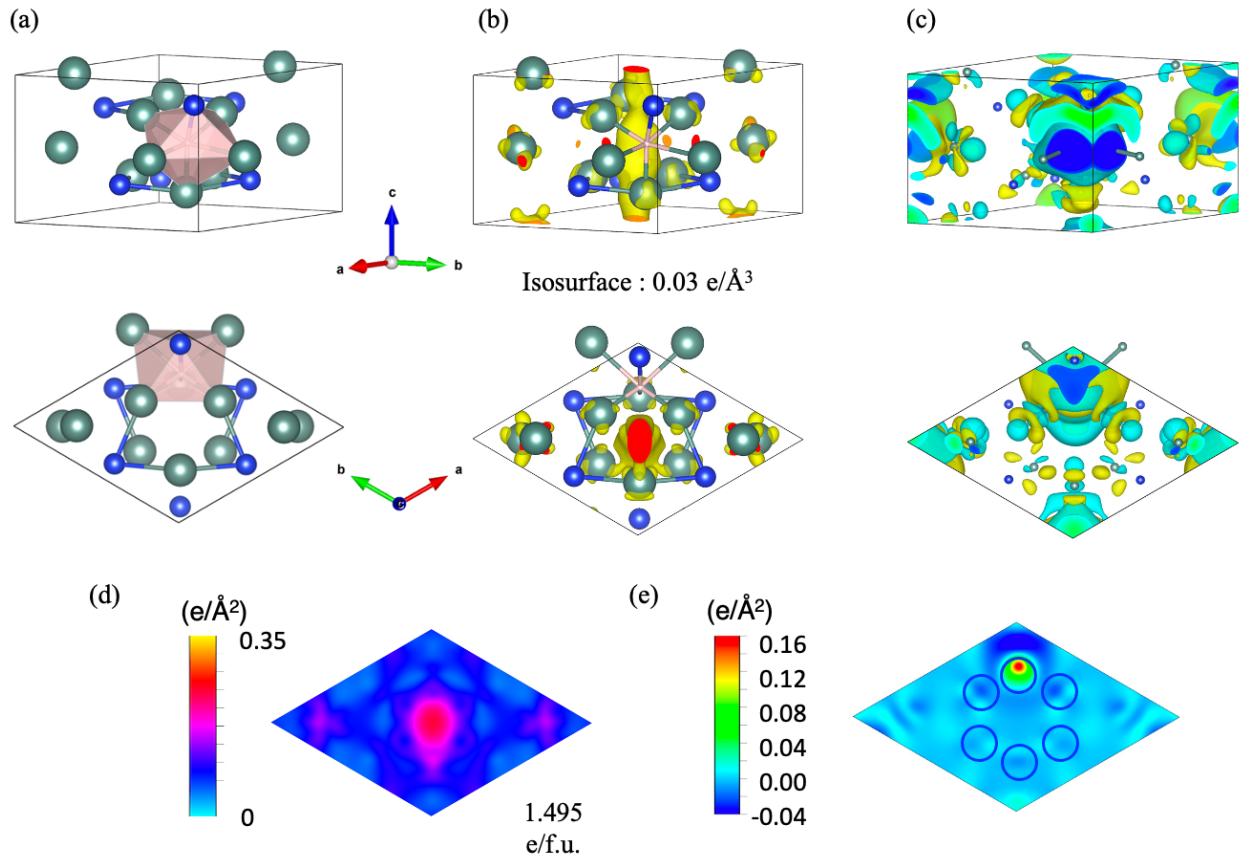


Figure 5. 18 The effect of a hydrogen atom located at site 2 of $Y_5Si_3H_{0.5}$ on the charge distribution. (a) Crystal structure of the site 2 of $Y_5Si_3H_{0.5}$ where the hydrogen atom is located at another octahedron site surrounded by five yttrium and one silicon atoms outside of the 1D hollow space. (b) Partial charge density (-0.5 eV < E-EF < 0), and (c) differential charge density. (d) Integrated partial charge density along c-axis. Anionic electron density shows asymmetric distribution. (e) Integrated differential charge density along c-axis. The six blue circles indicate the position of Yttrium atoms. It shows different levels of charge depletion and accumulation depending on the position of the yttrium atom.

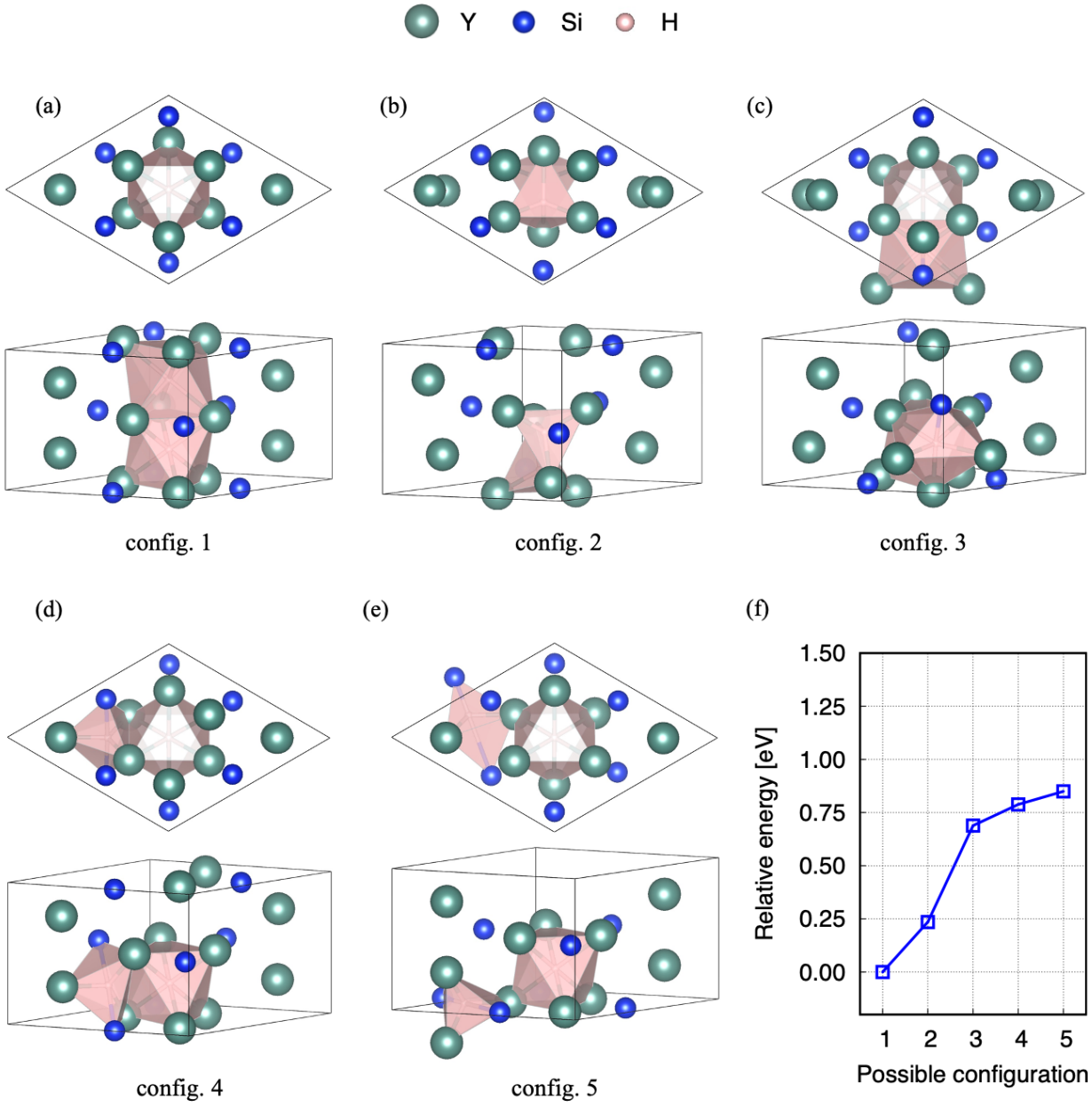


Figure 5. 19 Stable configurations of $Y_5Si_3H_1$ identified through crystal structure search. (a) ~ (e) Crystal structures of $Y_5Si_3H_1$ which contain two hydrogen atoms in a unit cell. (f) Relative energy differences of identified configurations.

Table 5. 3 Occupation sites of each hydrogen atom in $Y_5Si_3H_1$

Hydrogen atom	Occupation sites				
	Config. 1 [Fig. 5.19 (a)]	**Config. 2** [Fig. 5.19 (b)]	**Config. 3** [Fig. 5.19 (c)]	**Config. 4** [Fig. 5.19 (d)]	**Config. 5** [Fig. 5.19 (e)]
H1	Site 1	Double occupation in a single site 1	Site 1	Site 1	Site 1
H2	Site 1		Site 2	Site 3	Site 4

Projected band structures and DOS for each configuration are shown in Fig. 5.20. Like the case of $Y_5Si_3H_{0.5}$, where one new band corresponding to hydrogen s orbital is formed in the vicinity of -5 eV, two bands newly appear in the energy range of -6 eV < $E-E_F$ < - 4eV for all configurations of $Y_5Si_3H_1$. This means that the s orbitals of two hydrogen atoms are fully filled with electrons. Thus, both hydrogen atoms exist as H^- ions in the lattice. As can be predicted from the occupation sites of hydrogen atoms, in the case of configuration 1 where each hydrogen atoms are located at two anionic electron sites, two bands associated with anionic electrons disappear, while, for other configurations, one anionic electron band still show contributions from the hydrogen-free anionic electron site. Partial charge densities for each configuration in the energy range of -0.5 eV < $E-E_F$ < 0 eV (Fig. 5.21) also confirm this difference. In the case of configuration 1, the anionic electron density entirely disappears in the 1D hollow space, while, in other cases, the charge density is still present in the hydrogen-free anionic electron site. Moreover, for configuration 1, the shift of Fermi level, which occurs in the case of site 1 of $Y_5Si_3H_{0.5}$, also happens. This phenomenon is further enhanced because two hydrogen atoms occupy both anionic electron sites, so more electrons escape from the anionic electron site and fill the orbitals of metallic bands. If we compare the differential charge density of $Y_5Si_3H_1$ in Fig. 5.22 with that of $Y_5Si_3H_{0.5}$ shown in Fig. 5.17, it can be noticed that the same trend of charge transfer happens with an increased amount.

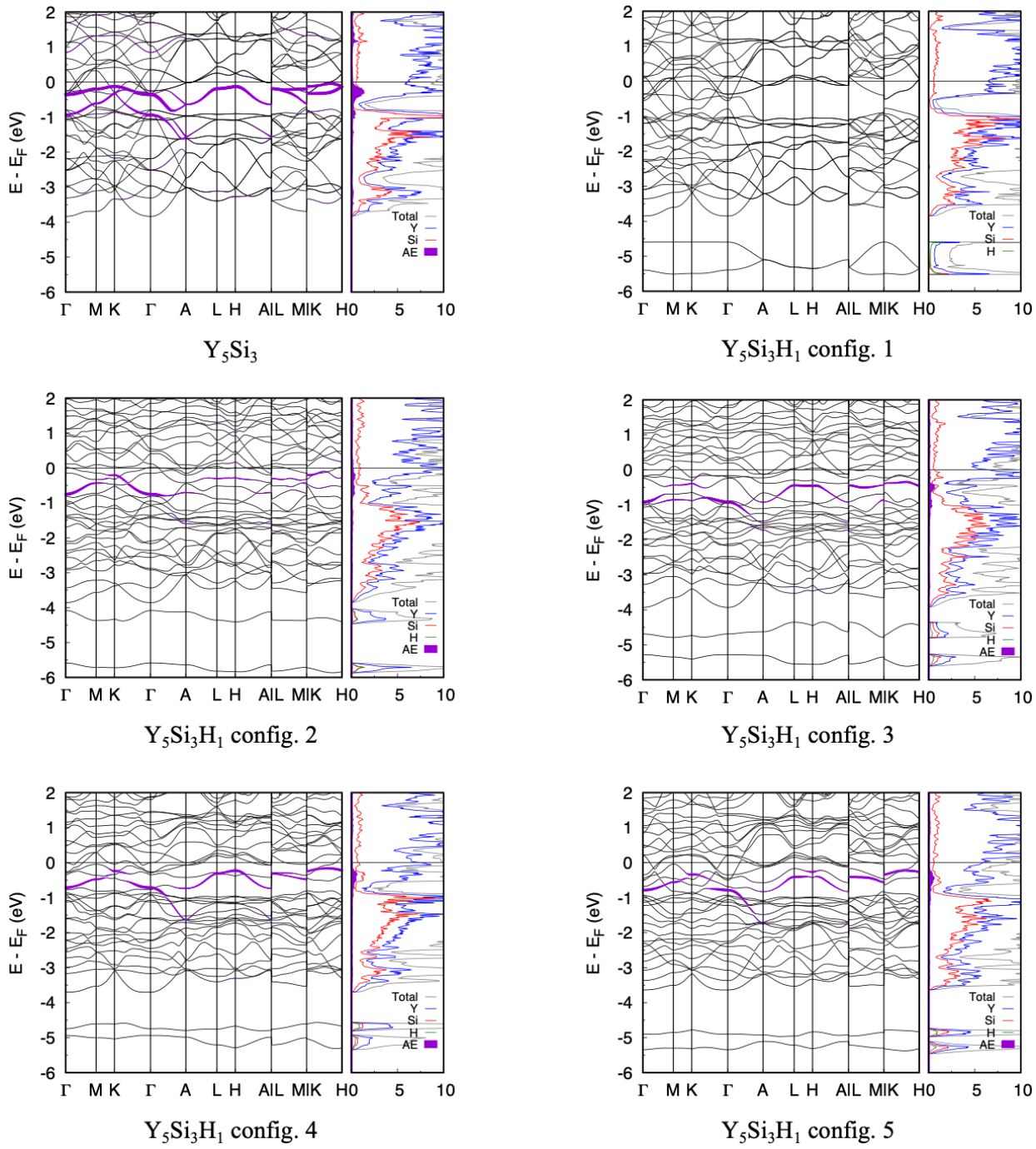


Figure 5. 20 Projected band structures and DOS of Y_5Si_3 and possible configurations of $Y_5Si_3H_1$ identified through crystal structure search. Contribution from the anionic electrons is indicated in purple color.

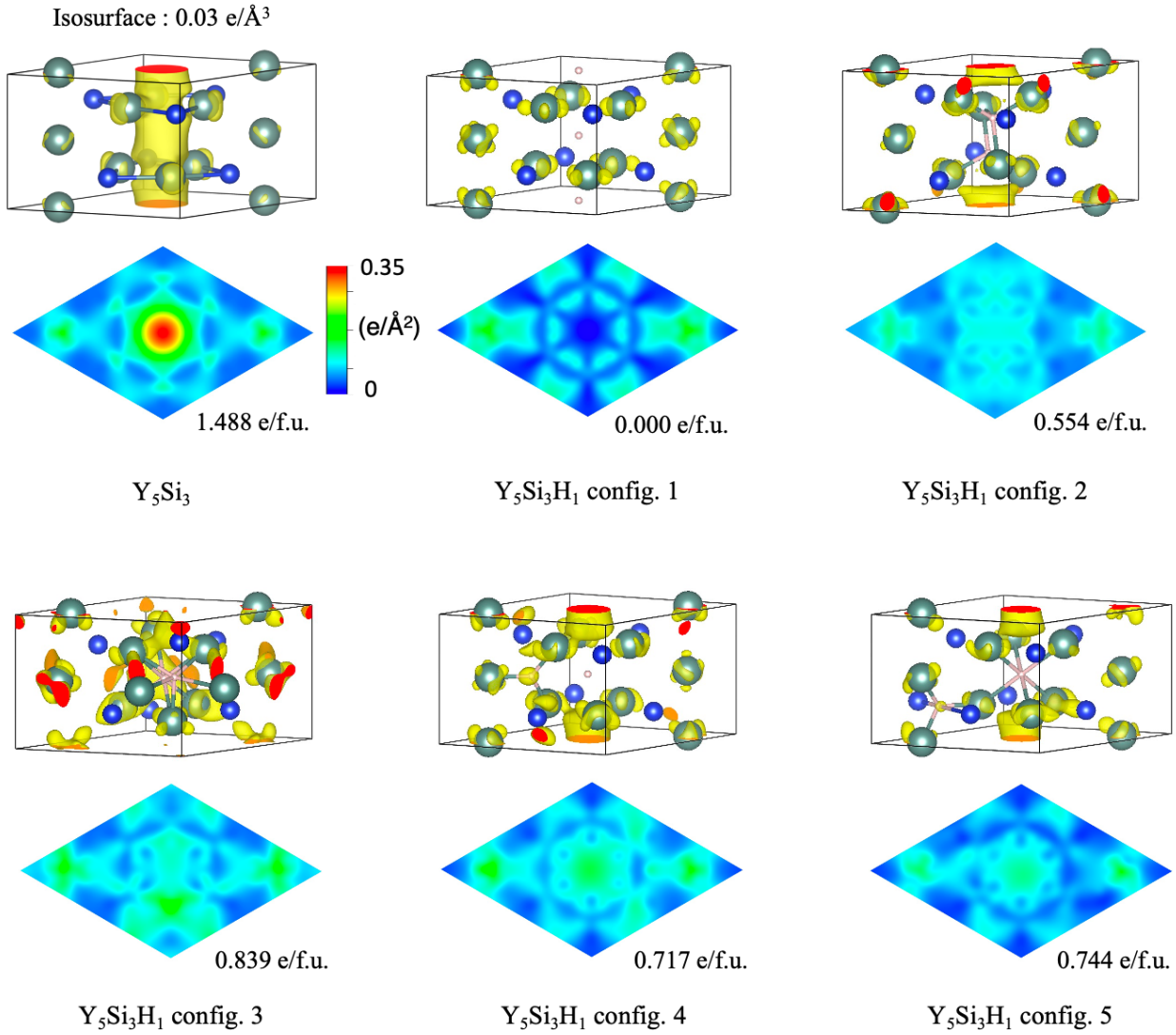


Figure 5. 21 Partial charge density of Y_5Si_3 and possible configurations of $Y_5Si_3H_1$ identified through crystal structure search. 3D and integrated (along c-axis) partial charge density in the energy range of -0.5 eV < E-E_F < 0 are drawn. Amount of the Bader charges of the anionic electrons are calculated from partial charge density in the energy range of -1.5 eV < E-E_F < 0.

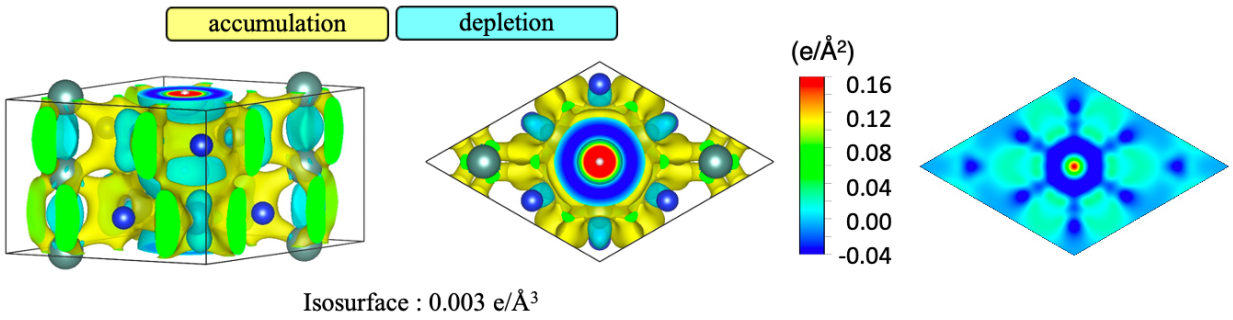


Figure 5. 22 Differential charge density due to the insertion of two hydrogen atoms into the config. 1 of $Y_5Si_3H_1$.

As the final point of discussion on the chemical composition of $Y_5Si_3H_1$, the interaction between two hydrogen atoms will be discussed. In the case of $Y_5Si_3H_{0.5}$, since the unit cell contains only one hydrogen atom, and considering the size of the unit cell, the interaction between the hydrogen atoms can be neglected because a distance between two hydrogen atoms is longer than 6 Å. However, in the case of $Y_5Si_3H_1$, we can expect that there is non-negligible interaction between hydrogen atoms because the spacing between them is relatively close. To examine the interaction between hydrogen atoms, additional investigations were carried out on two hydrogen-related bands placed in the energy range of -6 eV < $E-E_F$ < -4 eV. Figure 5.23 shows the band structure and DOS projected on each hydrogen atom, and band resolved partial charge densities corresponding to the bonding and anti-bonding states formed by the interaction between hydrogen atoms. In the figure, the left panel of the band structure shows contributions from the first hydrogen atom, while the right panel shows contributions from the second hydrogen atom. Fig. 5.23 (a) and (b) are for configuration 1 and 2, respectively. The hydrogen atoms in configuration 1 can be thought of like a 1D H^- ion chain aligned in the c-axis direction with the same spacing, and in the case of configuration 2, they can be considered as a $2H^-$ dimer confined in limited space of the lattice. The same phenomenon in both configurations is that two hydrogen atoms contribute

equally to the two bands lying in the energy range of -6 eV < E-E_F < -4 eV. This tells us that these two bands correspond to bonding and anti-bonding level caused by the interaction between hydrogen atoms. In the case of configuration 2, since the distance between hydrogen atoms is closer than that of configuration 1, the interaction becomes stronger, and the energy gap between the bonding and anti-bonding level increases accordingly.

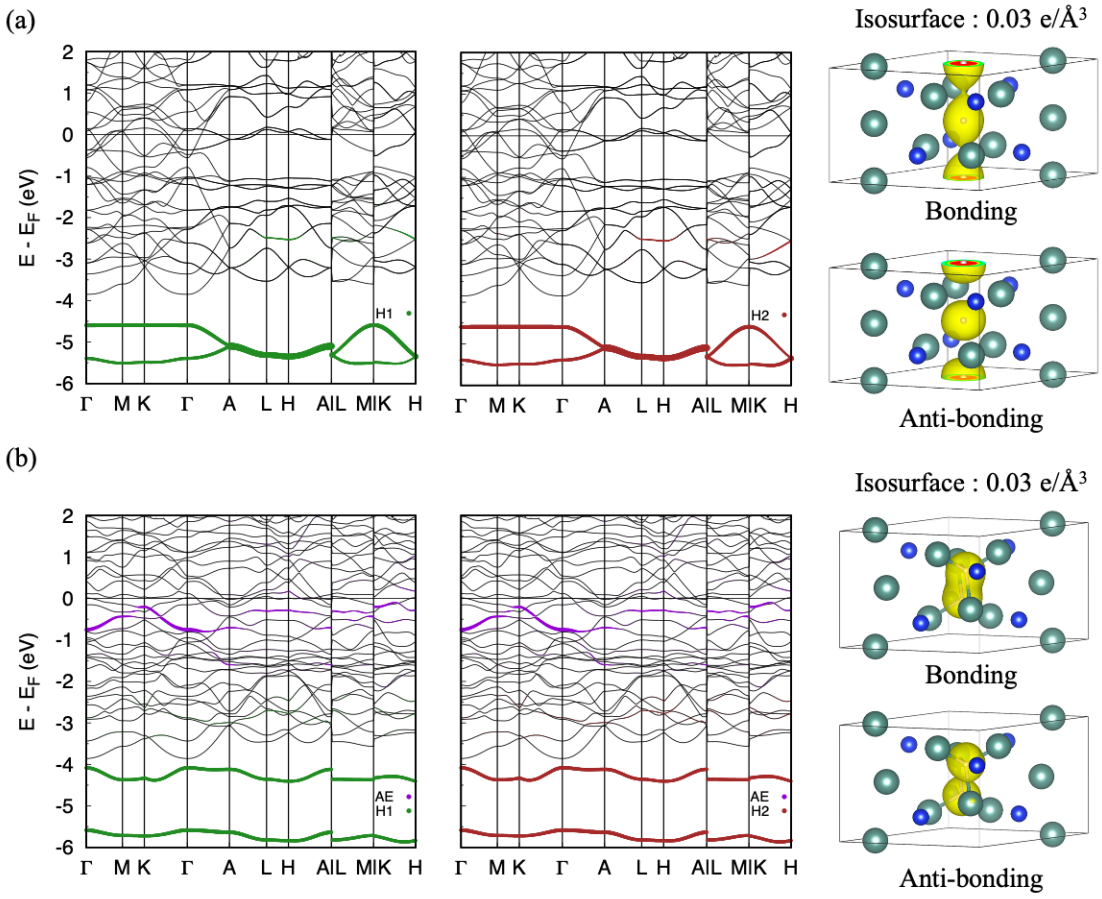


Figure 5. 23 Interaction between two hydrogen atoms in config. 1 and config. 2 of $Y_5Si_3H_1$. Projected band structure and DOS with partial charge density of bonding and anti-bonding electron band for (a) config. 1 and (b) config. 2.

$Y_5Si_3H_{1.5}$

Figure 5.24 shows the stable configurations identified through the crystal structure search for the hydrogen content of $Y_5Si_3H_{1.5}$. These configurations also consist of a combination of the possible hydrogen occupation sites we have seen so far for the lower hydrogen content. It should be noted here that the configuration 1 where all three hydrogen atoms remain in 1D hollow space is more stable than other configurations where one hydrogen atom is located at the outside of 1D hollow space. The occupation sites of hydrogen atoms for each configuration are listed in Table 5.4. The purpose of identifying stable configurations of this chemical composition, $Y_5Si_3H_{1.5}$, is to provide structural information for the diffusion barrier analysis which will be discussed in the next section. Therefore, further analysis of electronic structures such as band structure, DOS, partial charge density, and differential charge density was not carried out.

Table 5. 4 Occupation sites of each hydrogen atom in $Y_5Si_3H_{1.5}$

Hydrogen atom	**Occupation sites**				
	Config. 1 [Fig. 5.24 (a)]	**Config. 2** [Fig. 5.24 (b)]	**Config. 3** [Fig. 5.24 (c)]	**Config. 4** [Fig. 5.24 (d)]	**Config. 5** [Fig. 5.24 (e)]
H1	Double occupation in a single site 1	Site 1	Double occupation in a single site 1	Site 1	Site 1
H2		Site 1		Site 1	Site 1
H3	Site 1	Site 2	Site 2	Site 3	Site 4

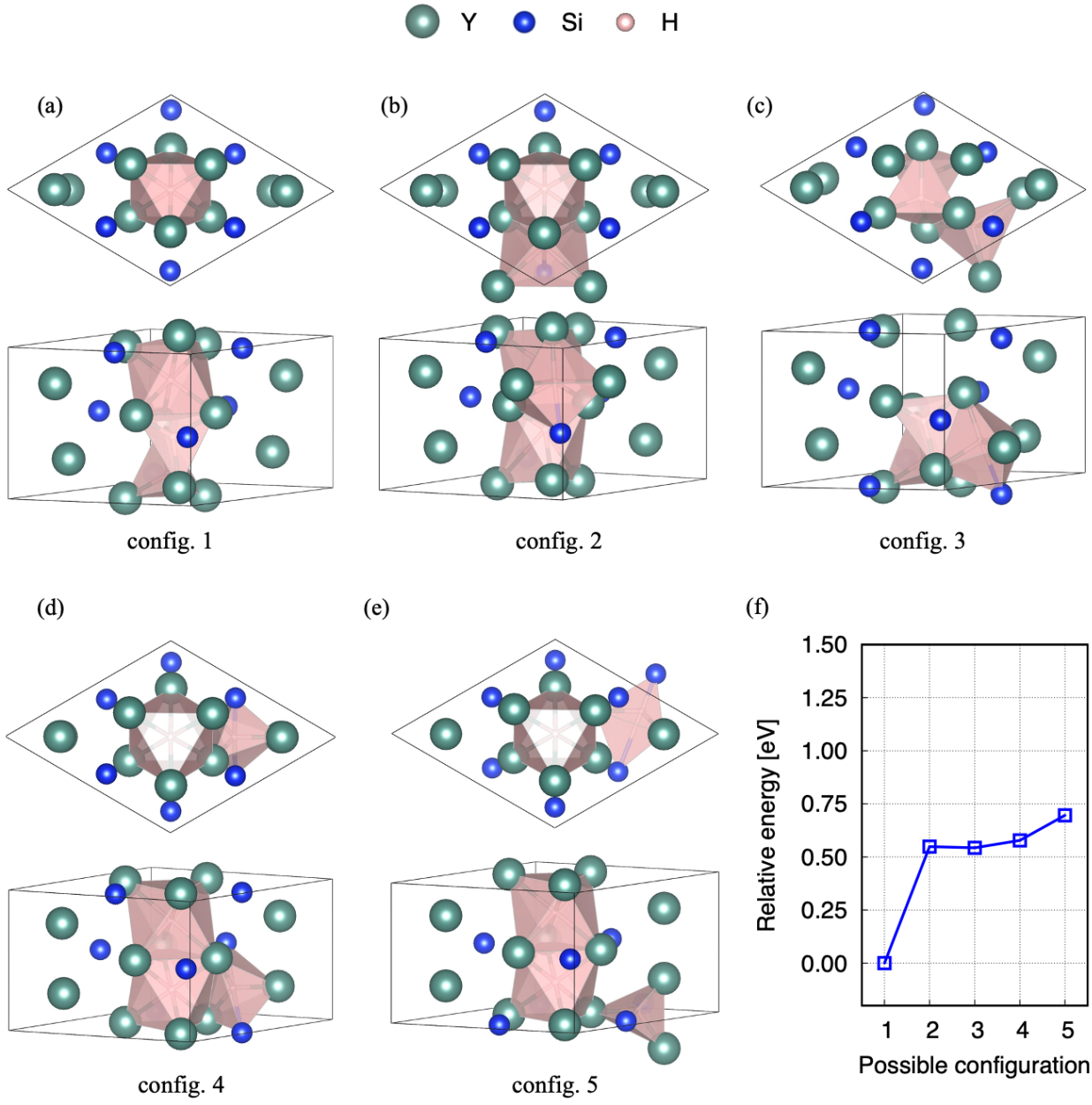


Figure 5. 24 Stable configurations of $Y_5Si_3H_{1.5}$ identified through crystal structure search. (a) ~ (e) Crystal structures of $Y_5Si_3H_{1.5}$ which contain three hydrogen atoms in a unit cell. (f) Relative energy differences of identified configurations.

Structural changes of $Y_5Si_3H_x$ ($0 \leq x \leq 8$)

In the previous discussion, the focus was on how the increase in hydrogen content changes the electronic structure of $Y_5Si_3H_x$. However, here I turn my attention to structural changes of $Y_5Si_3H_x$ due to the increase in hydrogen content. To examine the structural changes of $Y_5Si_3H_x$ caused by hydrogenation, restricted crystal structure searches were conducted up to the hydrogen content x=8 (16 hydrogen atoms in a Y_5Si_3 unit cell). First, I will discuss which sites the newly introduced hydrogen atoms occupy as hydrogenation progresses, and then I will look at how this trend affects structural parameters such as lattice vectors and volume.

Figures 5.25 ($0.5 \leq x \leq 4.0$) and 5.26 ($4.5 \leq x \leq 8.0$) show the structures identified as the most stable for each hydrogen content. As discussed previously, in the early stages of hydrogenation ($0.5 \leq x \leq 1.5$), hydrogen atom begins to fill a 1D hollow space in the center of the lattice where anionic electrons are distributed. At $Y_5Si_3H_{1.5}$, two hydrogen atoms are located at one of the two available site 1 (double occupation), and the other hydrogen atom occupies another site 1. Then, when x reaches to $Y_5Si_3H_2$, occupation in site 2 surrounding the 1D hollow space initiates. In the hydrogen content of $Y_5Si_3H_2$, the case where all four hydrogen atoms are located at two site 1 (two double occupation) in the center of the lattice does not occur, which means that this configuration is not stable at least at low hydrogen content. From x=2, the hydrogen atoms additionally occupy site 2, and when x becomes 3.5, the second double occupation in site 1 takes place. As shown in the top view of Fig. 5.25, in the case of x=3.5, four hydrogen atoms are located in the space surrounded by yttrium atoms in the center of the lattice, and three hydrogen atoms are placed in three of site 2, respectively. When x reaches to 4, two site 1 (double occupancy) and four site 2 (single occupancy) are saturated by eight hydrogen atoms. In brief, the tendency of hydrogen occupancy occurring in $0.5 \leq x \leq 4.0$ range can be summarized as follow.

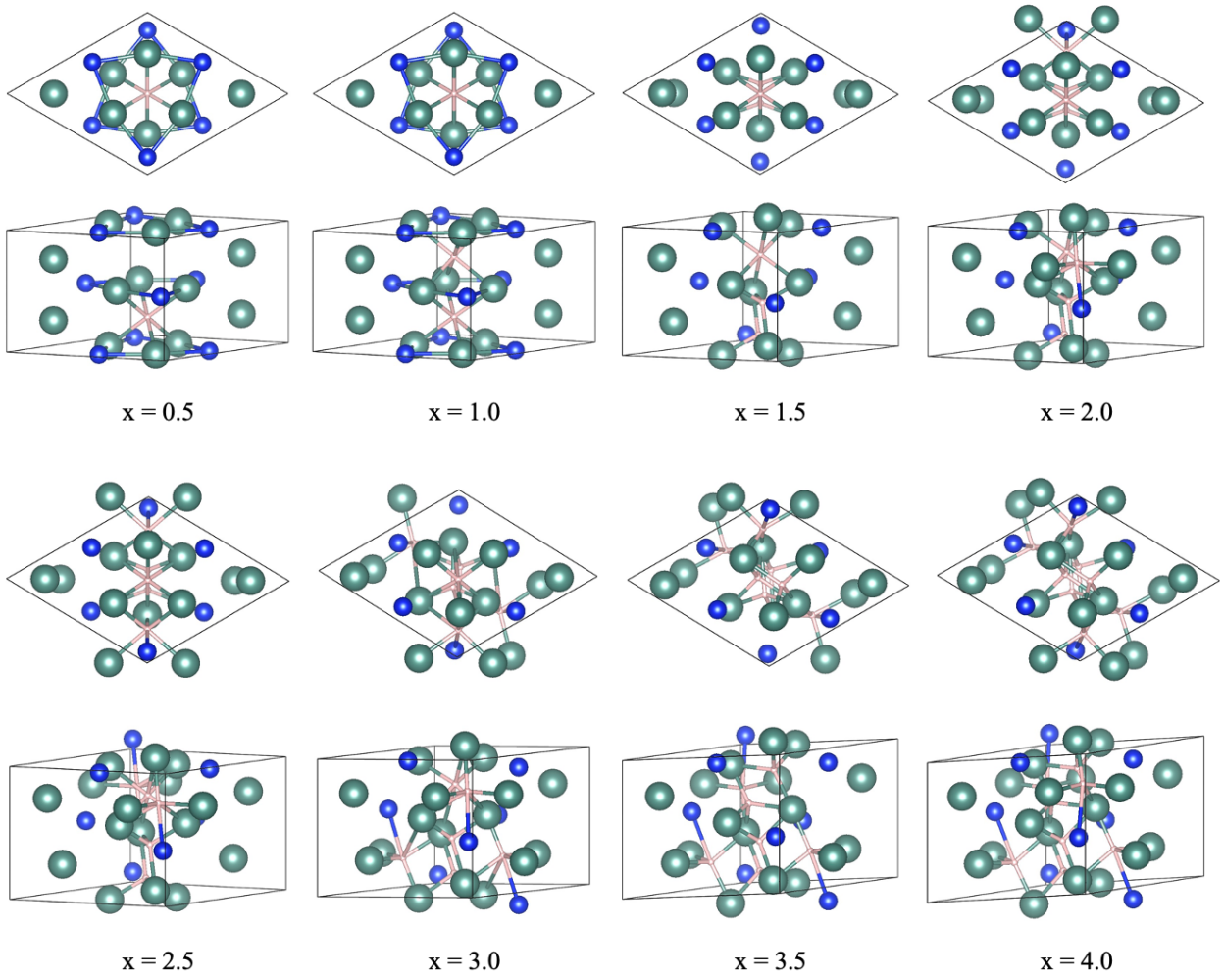


Figure 5. 25 Crystal structures of the most stable configurations of $Y_5Si_3H_x$ ($0.5 \leq x \leq 4$) identified through crystal structure search.

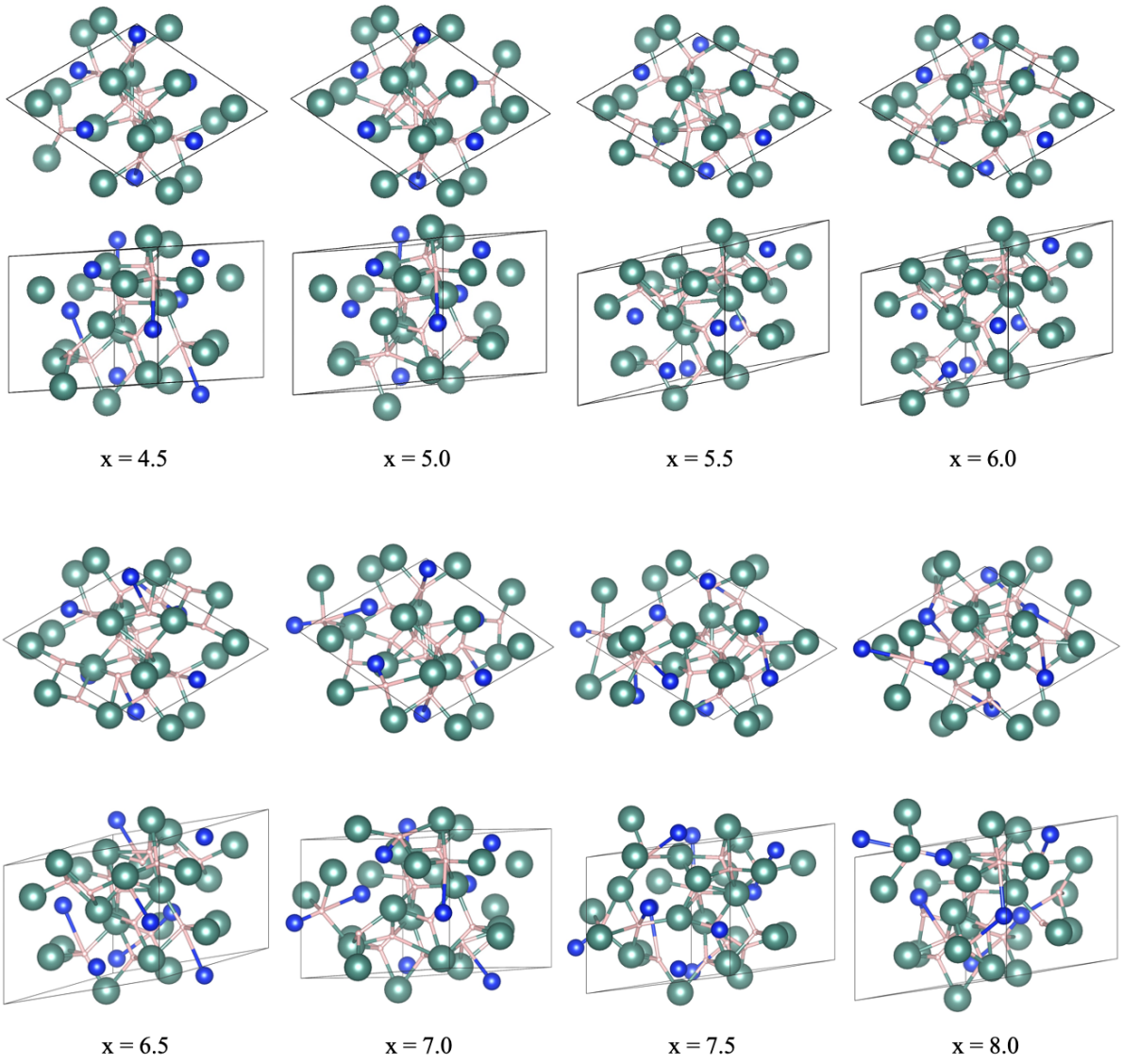


Figure 5. 26 Crystal structures of the most stable configurations of $Y_5Si_3H_x$ ($4.5 \leq x \leq 8$) identified through crystal structure search.

The two site 1 located in the 1D hollow space in the center of the lattice are filled with hydrogen atoms first, and then hydrogen atoms begin to occupy site 2. Furthermore, at x=1.5 and 3.5, the first and second double occupation of the hydrogen atoms on site 1 occurs. Finally, available site 1 and site 2 are saturated with eight hydrogen atoms at x=4. When the hydrogen content x exceeds 4, a more complex pattern appears, as shown in Fig. 5.26. Once site 1 and site 2 are saturated, additionally intercalated hydrogen atoms begin to occupy arbitrary sites that cannot be classified into the stable sites identified in the case of $Y_5Si_3H_{0.5}$. It is also difficult to find a consistent pattern, such as found in the range of $0.5 \leq x \leq 4.0$.

Figure 5.27 shows how the formation energy, volume, and lattice parameters of $Y_5Si_3H_x$ change as the hydrogenation progresses. The formation energy was calculated using the following formula.

$$E_f = E_{\text{bulk}}(Y_5Si_3H_x) - E_{\text{bulk}}(Y_5Si_3) - x \cdot 1/2\, E_{\text{molecule}}(H_2)$$

This quantity represents the amount of energy that decreases when hydrogen in the form of a molecule is absorbed into one formula unit of Y_5Si_3. From the plot (Fig. 5.27 (a)), we can see that as the hydrogen content increases, the formation energy continues to decrease and gradually increases after around x=6. This implies that, if we ignore energy barriers for hydrogen diffusion, and the effect of temperature, hydrogen intercalation into the Y_5Si_3 lattice can be achieved up to about $Y_5Si_3H_6$. However, it is known that such spontaneous hydrogenation does not occur unless a sufficient temperature for hydrogen diffusion is reached [28]. However, if we consider the fact that the maximum hydrogen content of $Y_5Si_3H_x$ at the sufficiently high temperature is 6.8 [28], the formation energy plot obtained through DFT calculations shows meaningful results confirming that the higher hydrogen conctet is not achievable.

Next, changes in structural parameters due to the hydrogenation will be discussed. Structural parameters for different hydrogen content are listed in Table 5.5 and plotted in Fig. 5.27 (b) ~ (d). The table shows the raw data for those parameters, and in the graphs, changing ratios are plotted compared to the pristine structure, Y_5Si_3.

Table 5. 5 Changes of structural parameters as x increases in $Y_5Si_3H_x$

x	a (Å)	b (Å)	c (Å)	α (°)	β (°)	γ (°)	volume (Å^3)	Space group	lattice system
0.0	8.453	8.453	6.377	90.0	90.0	120.0	394.6	$P6_3/mcm$ (#193)	Hexagonal
0.5	8.460	8.460	6.312	90.0	90.0	120.0	391.2	$P\bar{3}1m$ (#162)	Hexagonal
1.0	8.464	8.464	6.253	90.0	90.0	120.0	388.0	$P6_3/mcm$ (#193)	Hexagonal
1.5	8.285	8.285	6.624	89.1	89.1	119.3	396.4	C2/m (#12)	Monoclinic
2.0	8.237	8.237	6.686	89.4	89.4	119.1	396.1	Cm (#8)	Monoclinic
2.5	8.199	8.199	6.744	89.6	89.6	119.0	396.5	C2/m (#12)	Monoclinic
3.0	8.062	8.136	6.948	87.4	88.2	117.8	402.0	P1 (#1)	Triclinic
3.5	8.035	8.273	7.001	85.0	89.3	118.4	406.9	P1 (#1)	Triclinic
4.0	8.014	8.322	7.052	84.0	90.0	118.8	409.2	Cc (#9)	Monoclinic
4.5	7.846	8.224	7.183	83.5	85.5	115.3	412.1	P1 (#1)	Triclinic
5.0	7.726	8.209	7.374	81.1	85.6	114.1	416.8	P1 (#1)	Triclinic
5.5	7.688	8.767	7.371	77.2	94.9	120.4	417.5	P1 (#1)	Triclinic
6.0	7.715	8.742	7.359	77.6	94.9	120.3	418.3	P1 (#1)	Triclinic
6.5	7.734	8.748	7.356	78.2	95.8	120.0	421.7	P1 (#1)	Triclinic
7.0	7.786	8.266	7.373	83.3	83.5	114.0	423.9	P1 (#1)	Triclinic
7.5	7.846	8.368	7.520	80.2	89.9	117.7	428.7	P1 (#1)	Triclinic
8.0	7.869	8.542	7.622	78.7	90.9	118.8	438.2	P1 (#1)	Triclinic

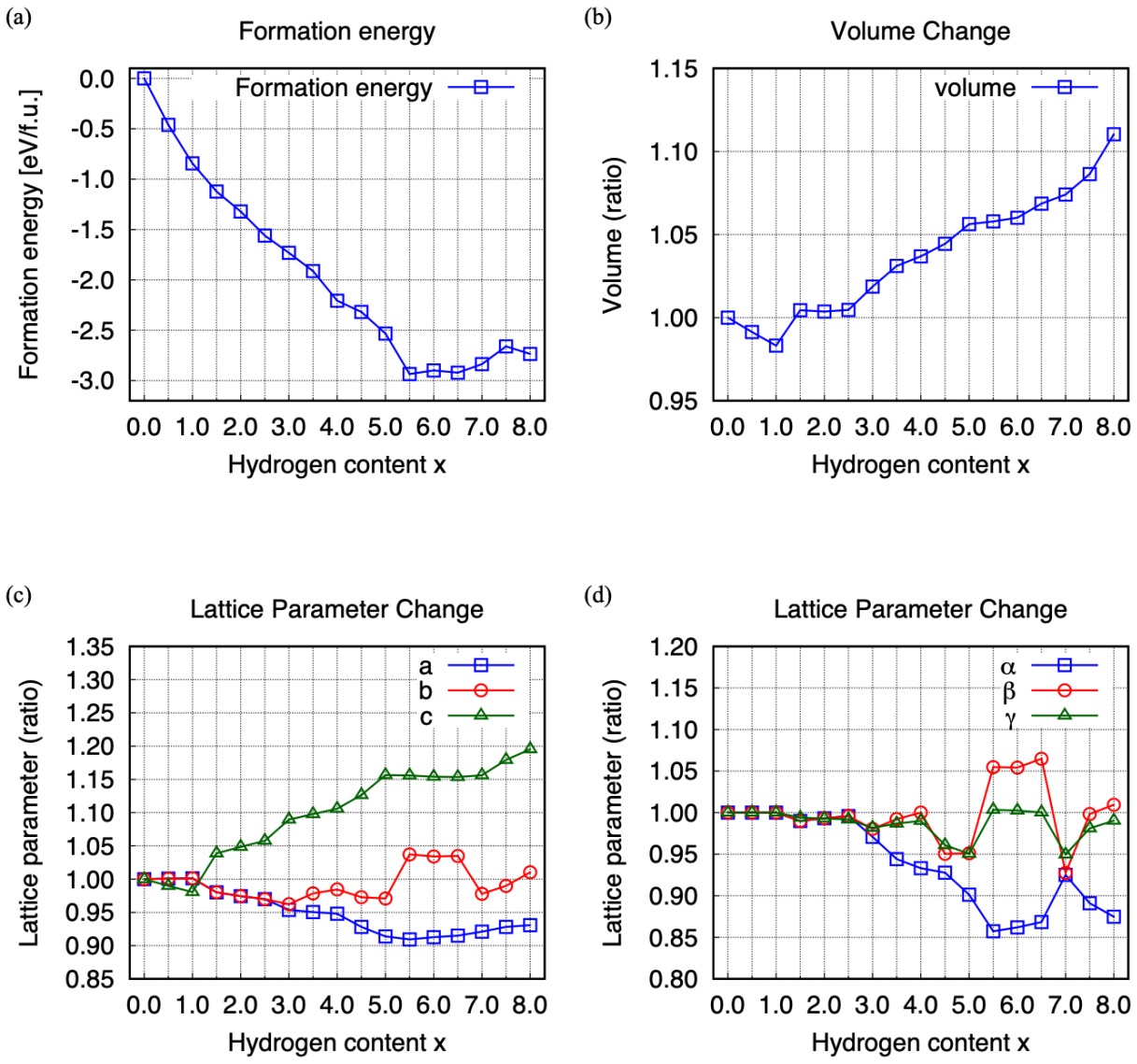


Figure 5. 27 Changes in formation energy and structural parameters of $Y_5Si_3H_x$ ($0 \leq x \leq 8$) (a) Formation energy per formula unit, (b) volume of unit cell, (c) lengths of lattice vectors, and (d) angles between lattice vectors as a function of hydrogen content x.

In the initial stage of hydrogenation ($0 \leq x \leq 1$), hydrogen atoms go into the site 1, shortening lattice constant c, and the volume decreases. However, angles between the lattice vectors are maintained, so the hexagonal lattice is unaffected. When x becomes 1.5, changes in lattice angles occurs, and the hexagonal lattice changes to monoclinic structure. The double occupation of hydrogen atoms in site 1 causes this structural deformation, where the shape of the octahedron surrounded by yttrium atoms is distorted, and the hexagonal symmetry is broken. Since then, as hydrogen atoms are additionally inserted, the volume increases. The next notable change occurs when x=3. Starting from this hydrogen content, the lengths of a and b, and the angles of α and β begin to differ from each other, resulting in a change of structure from monoclinic to triclinic lattice. This phenomenon is consistent with the experimental observation, where highly strained and disordered structures observed at the hydrogen content higher than 2.6 [28]. When the hydrogen content exceeds x=4, the hydrogen occupation proceeds without a certain pattern, as discussed above, and the lattice parameters are randomly and markedly fluctuate.

5.3.2 Diffusion of Hydrogen Ion in Y_5Si_3 Bulk Phase

So far, the atomic configurations that may occur during the hydrogenation process of Y_5Si_3 was discussed. From now on, hydrogen diffusion inside the Y_5Si_3 lattice will be discussed, which is an essential element in understanding the hydrogenation mechanism of Y_5Si_3.

The diffusion rate is determined by the rate constant or diffusion coefficient k, and the diffusion coefficient is given by the Arrhenius equation as follows.

$$k = Ae^{\frac{-E_b}{k_B T}},$$

where A is the pre-exponential factor, E_b is the energy barrier, k_B is the Boltzmann constant, and T is the temperature. Here, the energy barrier is a critical factor that determines the diffusion rate. In the $Y_5Si_3H_x$ lattice, various hydrogen diffusion paths are possible depending on the configuration of hydrogen occupations discussed above. Stable configurations of three different hydrogen contents, x=0.5, 1, and 1.5 in $Y_5Si_3H_x$, were considered, and a solid-state NEB method was used for DFT calculation of the diffusion barrier estimation.

As an example of diffusion paths, Fig. 5.28 shows three possible diffusion paths that can be considered for $Y_5Si_3H_{0.5}$. Path 1 is the diffusion from site 1 to another site 1, where a hydrogen atom moves along the c-axis through the 1D hollow space.

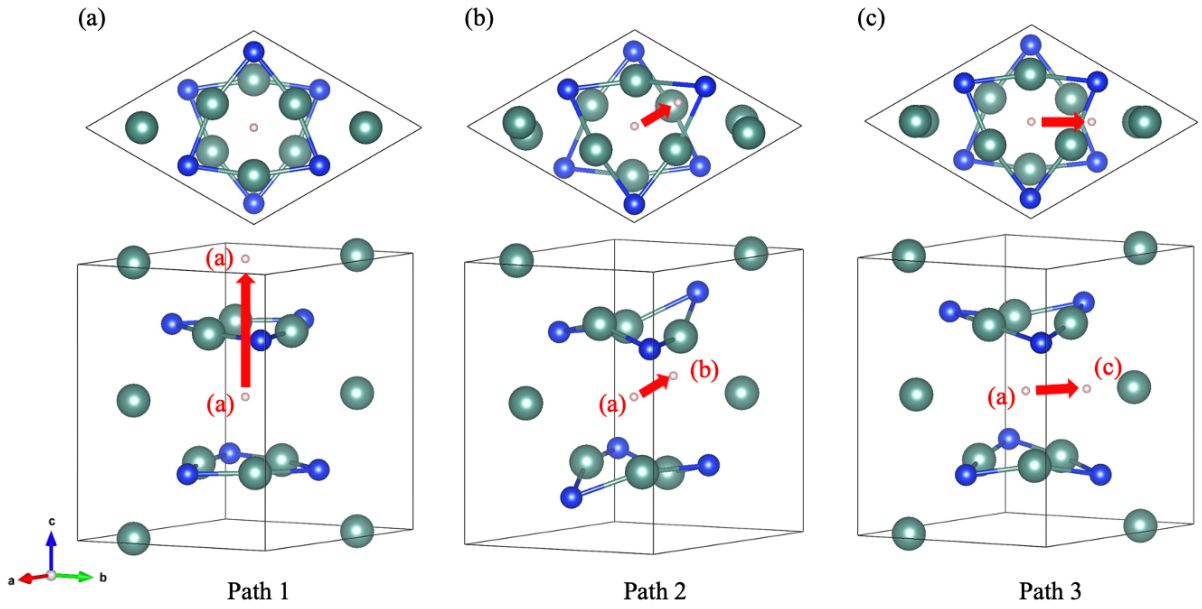


Figure 5. 28 Diffusion paths for hydrogen migration in the unit cell of $Y_5Si_3H_{0.5}$. To clearly show the paths, the length of the c-axis is elongated three times. (a) Path 1: diffusion from site 1 to another site 1 along the c-axis. (b) Path 2: diffusion from site 1 to site 2 in the ab-plane. (c) Path 3: diffusion from site 1 to site 3 in the ab-plane.

Paths 2 and 3 represent hydrogen diffusions from site 1 to site 2 and 3, respectively. For paths 2 and 3, the hydrogen atom moves from inside to outside of the 1D channel in the a-b plane.

The calculated energy barriers for possible diffusion paths at x=0.5, 1, and 1.5 are shown in Fig. 5.29 and listed in Table 5.6. Initial and final atomic configurations for each path are embedded in the plots. Figure 5.29 (a) shows the diffusion barriers for the three paths of $Y_5Si_3H_{0.5}$ described in Fig. 5.28. This plot reveals three fundamental facts regarding the hydrogen diffusion in the Y_5Si_3 lattice.

1) First, path 1 shows the lowest diffusion barrier of 0.44 eV, and that of path 2 and 3 are 0.76 eV and 0.92 eV, respectively, indicating that the path 1 is the principal channel for the hydrogen diffusion. In the path 1, the hydrogen atom has to overcome the barrier as it moves along the c-axis in the 1D hollow space, passing through a triangular ring formed by yttrium and silicon atoms.
2) Second, the energy changes of paths 2 and 3 through the reaction coordinate proceeds in the same way. In other words, in path 3, the hydrogen atom passes through site 2 and arrives at site 3.
3) Finally, the energy barriers for the reverse directions of path 2 and 3 are negligible, implying that, although site 2 and 3 are locally stable hydrogen occupation sites, the hydrogen atom readily diffuses to site1. This suggests that site1 is not only energetically but also dynamically the most favorable site for hydrogen occupancy.

Hydrogen diffusion barriers for the $Y_5Si_3H_1$ (Fig. 5.29 (b)) show similar results with $Y_5Si_3H_{0.5}$. In the initial state of path 1, both of two site 1 are occupied by hydrogen atoms, and one hydrogen atom moves along the c-axis forming a double-occupied site 1 in the final state.

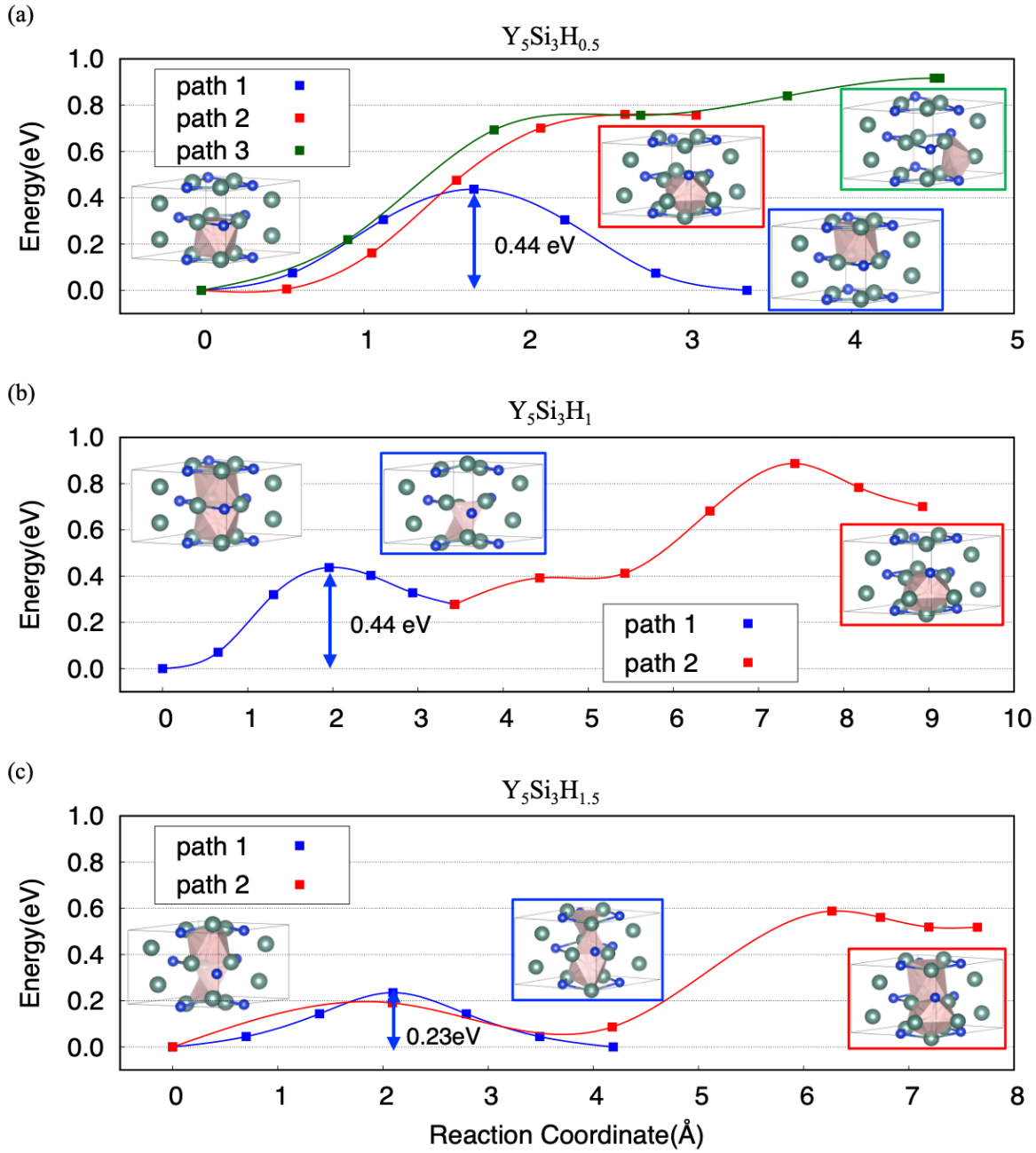


Figure 5. 29 Diffusion barriers for hydrogen migration in $Y_5Si_3H_x$ (a) x = 0.5, (b) x = 1, and (c) x=1.5. Images of the initial and final structures for each path are inserted inside the graph. For each composition, blue line is for the diffusion along the c-axis. Red and green lines are for diffusions in ab-plane.

Table 5. 6 Diffusion barriers of possible paths for $Y_5Si_3H_x$ (x=0.5, 1, and 1.5). Initial and final sites for the hydrogen diffusion is given in parentheses. Site 1* is indicating a double occupation of hydrogen atoms in site 1.

	Diffusion barrier (eV)		
	path 1	path 2	path 3
$Y_5Si_3H_{0.5}$	0.44 (site 1 to site 1)	0.76 (site 1 to site 2)	0.92 (site 1 to site 3)
$Y_5Si_3H_1$	0.44 (site 1 to site 1*)	0.61 (site 1* to site 2)	
$Y_5Si_3H_{1.5}$	0.23 (site 1* to site 1*)	0.59 (site 1* to site 2)	

Path 2 is a case where one hydrogen atom moves from double-occupied site 1 to adjacent site 2. The barrier for diffusion along the c-axis (path 1) shows the same value with that of the path 1 of $Y_5Si_3H_{0.5}$ which is 0.44 eV, and the barrier in the a-b plane (path 2) is 0.61 eV. Finally, in the case of $Y_5Si_3H_{1.5}$, the diffusion barrier along the c-axis is calculated to be 0.23 eV, which shows a decrease of 0.21 eV compared to 0.44 eV estimated in the lower hydrogen contents. This is mainly because the double-occupied state in the initial and final states of the diffusion path has higher energy than the single-occupied state. In other words, compared to path 1 of $Y_5Si_3H_{0.5}$, the energies of the initial and final states are higher, so the energy barrier gets relatively lowered. For the same reason, the energy barrier for diffusion in the a-b plane (path 2) is lower than that of $Y_5Si_3H_{0.5}$ by 0.17 eV.

Based on our understanding of the atomic configurations and diffusion barriers of $Y_5Si_3H_x$ described so far, we can explain several experimental results [28] on hydrogenation of Y_5Si_3 that the causes have not yet been clarified.

First, In the initial stage of hydrogenation of Y_5Si_3Hx, the hydrogen content slowly increased, but when $1 < x < 2$, rapid hydrogen adsorption was observed. It was claimed that this sudden rate change is attributed to a martensitic transformation, that is, deformation of the lattice structure caused by temperature change. As shown in Table 5.5, it is true that, in this hydrogen content range, the hexagonal symmetry is broken, and the structure deforms into a monoclinic structure. However, this is not the martensitic transformation, but a change of structure caused by the double occupation of hydrogen in site 1. The cause of the rapid adsorption occurring in this hydrogen content range is not the structure deformation, but the reduction of the diffusion barrier (-0.21eV) due to the double hydrogen occupation. The change in diffusion rate due to the reduction of the diffusion barrier, ΔE_b, can be estimated by considering the diffusion coefficient k as shown below.

$$\frac{k'}{k} = e^{-\frac{(E_b'-E_b)}{k_BT}} = e^{-\frac{\Delta E_b}{k_BT}}$$

The report regarding the hydrogenation of Y_5Si_3 demonstrated that the maximum hydrogen adsorption rate is achieved at 375°. At this temperature, the barrier reduction of 0.21 eV results in 43 times faster diffusion.

Second, when the hydrogen content exceeds 3, it was observed that this fast diffusion phenomenon begins to disappear, and the adsorption rate gets extremely slow even at the higher temperature. However, the cause of this phenomenon has not been clarified. The cause can be explained by considering a necessary condition for the fast diffusion, and the structural change of $Y_5Si_3H_x$. As discussed earlier, the main channel of the hydrogen diffusion is the 1D vacant space encompassed by Y-Si rings, and a key element inducing the fast diffusion is neighboring double and single occupation of hydrogen atoms. However, as shown in Fig. 5.25, when x=3.5, the 1D hollow space, the main diffusion channel, becomes saturated with four hydrogen atoms, and

diffusion can only happen in the a-b plane, which shows a higher diffusion barrier. This provides a reasonable explanation for the disappearance of fast diffusion, and the very slow hydrogen adsorption at higher hydrogen content.

5.3.3 Penetration of Hydrogen Atom and Molecule through Y_5Si_3 (001) Surface

As a final discussion on the hydrogen adsorption property of Y_5Si_3, hydrogen penetration through the Y_5Si_3 (001) surface was investigated. More specifically, the energy barrier required for hydrogen to penetrate Y_5Si_3 (001) surface was estimated using the DFT calculation. The case of a single hydrogen atom will be discussed first, and then a hydrogen molecule.

Penetration of hydrogen atom

Y_5Si_3 (001) 1×1 surface slab was constructed to calculate the penetration barrier of the hydrogen atom. The surface slab contains four layers of the Y-Si ring and terminates with those rings on both ends. After constructing the surface slab, the interaction between the surface and hydrogen atom was examined by moving the hydrogen atom continuously along the vertical line, which is parallel to the c-axis and passes through the center of the a-b plane. The hydrogen atom was placed 5 Å away from the outermost surface and moved toward the surface at intervals of 0.25 Å. At each point, the position of the hydrogen atom was fixed, and atoms on the surface slab were relaxed only in the a-b plane. The total energy, force acting on the hydrogen atom, differential charge density, and projected DOS were calculated at each point to investigate the interaction between the surface and the hydrogen atom.

Figure 5.30 (a) is a plot showing how the total energy of the slab and the force on the hydrogen atom change as the hydrogen atom moves, and Fig 5.30 (b) illustrates differential charge densities

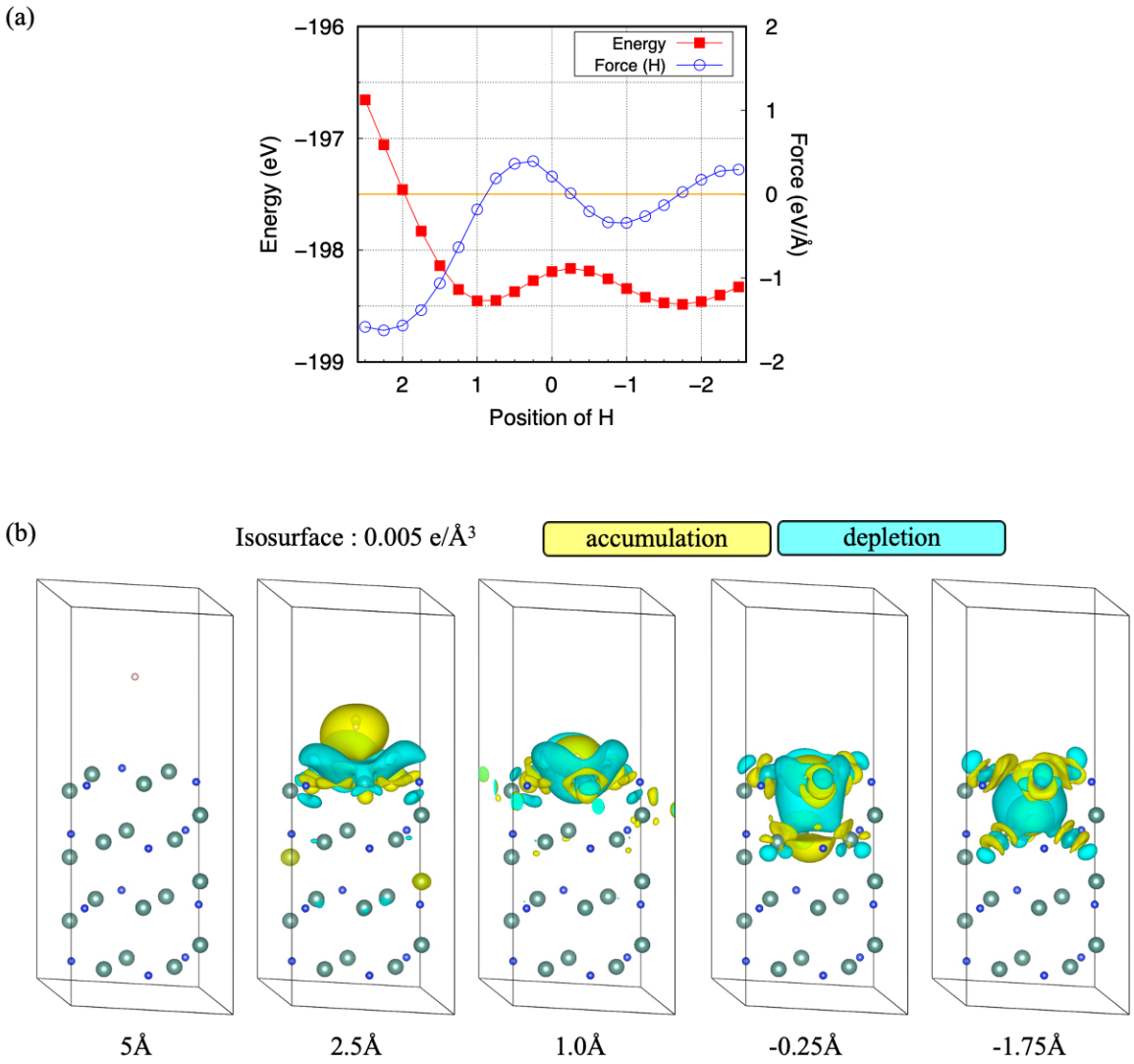


Figure 5. 30 Energy barrier for penetration of a hydrogen atom through Y_5Si_3 (001) surface. (a) Energy of surface slab and force on the hydrogen atom as a function of the position of the hydrogen atom. (b) Differential charge densities at different positions of the hydrogen atom.

at different hydrogen positions. The reference point for the hydrogen position is the plane of the outermost surface, and a positive number means outside the surface. From the differential charge densities showing the charge transfer between the surface and the hydrogen atom, we can notice that there is no interaction between the surface and the hydrogen atom when the hydrogen atom is located at 5Å. However, when it gets closer to the surface (2.5Å), electron transfers from the surface to the hydrogen atom, and the Coulomb attraction occurs between them. Figure 5.30 (a) shows that negative force is acting on the negatively charged hydrogen atom, or H^- ion due to this Coulomb attraction. Then, the H^- ion is dragged toward the surface and stabilized at 1Å. The energy plot shows that there is a penetration barrier of 0.29 eV for the hydrogen atom to pass through the triangular Y-Si ring located on the outermost surface. Once the hydrogen atom overcomes this barrier, the anionic electron distributed in the vacant space inside the surface is absorbed by the hydrogen atom. The projected DOS shown in Fig. 5.31 explains the charge state of the hydrogen atom and interaction with the surface more clearly. When the hydrogen atom is far from the surface (5 Å), only the spin up channel of the s orbital of the hydrogen atom is filled, but when the hydrogen atom reaches near the surface (2.5 Å), both the spin up and down channels are filled, and the hydrogen atom becomes an H^- ion. In the process of passing through the Y-Si ring (-0.25 Å), s orbital broadening occurs due to the interaction with the surrounding yttrium atoms. Once the hydrogen atom is fully seated in the vacant space (-1.75 Å) inside the surface, the interaction with the yttrium atoms gets weaker, and the s orbital band becomes sharp again.

We should note that the penetration barrier (0.29 eV) is less than the diffusion barrier (0.44 eV) in the bulk phase discussed earlier. This suggests that, during the hydrogenation reaction of Y_5Si_3, penetration through the surface cannot be a rate-limiting process, and the diffusion inside the material determines the overall hydrogen adsorption rate.

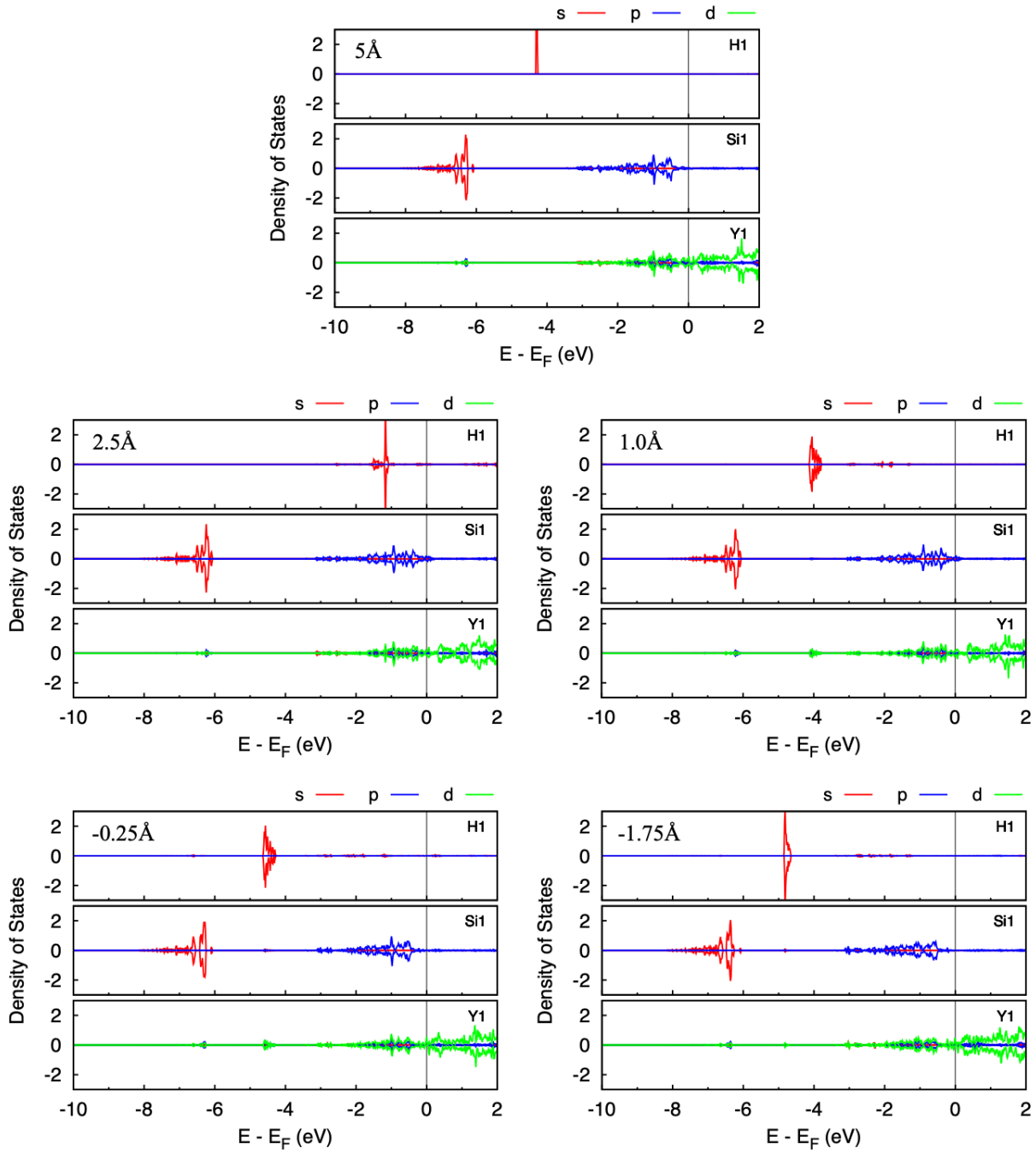


Figure 5. 31 Projected DOS of Y_5Si_3 (001) surface with a hydrogen atom at difference distances. Y1 and S1 mean the yttrium and silicon atom on the outermost surface.

Penetration of hydrogen molecule

The penetration of the hydrogen molecule through the Y_5Si_3 (001) surface was also examined. The investigation was carried out in a similar way as for the penetration of the hydrogen atom, except that the hydrogen molecule replaces the hydrogen atom. The hydrogen molecule was aligned perpendicular to the surface. The position of the bottom hydrogen atom close to the surface was fixed, and the top hydrogen atom and atoms in the Y_5Si_3 surface were relaxed. As shown in Fig. 5.32 (a), the force acting on the top hydrogen atom is zero at all positions, which means that the rest of the surface slab is fully relaxed except for the bottom hydrogen atom. The total energy of the slab, forces acting on the two hydrogen atoms, differential charge density, and projected DOS were calculated at different positions of the bottom hydrogen atom.

A noticeable change in the energy profile in the surface penetration process of the hydrogen molecule compared to the case of the hydrogen atom is that it does not exhibit the low energy state, i.e., a locally stable state, outside the surface. The reason can be inferred by comparing the differential charge densities shown in Fig. 5.30 (b) and Fig. 5.33(b). In the case of the single hydrogen atom, the charge transfer from the surface to the hydrogen atom occurs at 2.5 Å, and the Coulomb interaction results in the locally stable state outside the surface. However, in the case of the hydrogen molecule, the charge transfer does not occur until it passes through the outermost surface of the slab. Thus, the locally stable state outside the surface does not appear. In other words, in the case of the hydrogen atom, since the stable state exists outside the outermost surface, an energy barrier for passing through the triangular Y-Si ring emerges. However, in the case of the hydrogen molecule, one hydrogen atom can penetrate the outermost surface without this energy barrier. The projected DOS, shown in Fig. 5.33 confirms this different charge transfer trend more clearly. Before the position of the bottom hydrogen atom reaches to 0 Å, there is no significant

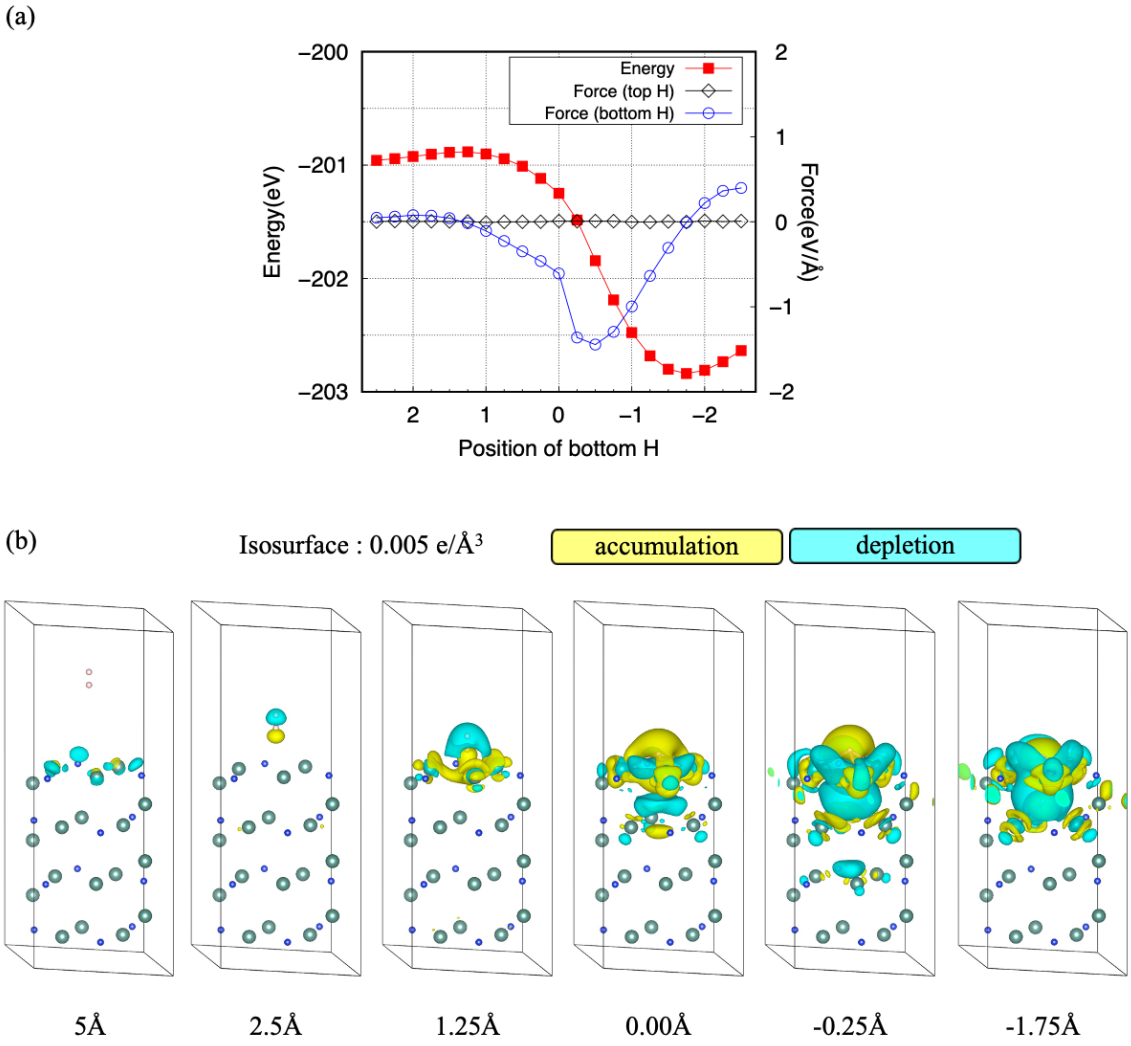


Figure 5. 32 Energy barrier for penetration of a hydrogen molecule through Y_5Si_3 (001) surface. (a) Energy of surface slab and forces on hydrogen atoms as a function of the position of the bottom hydrogen atom. (b) Differential charge densities at different positions of the hydrogen atom.

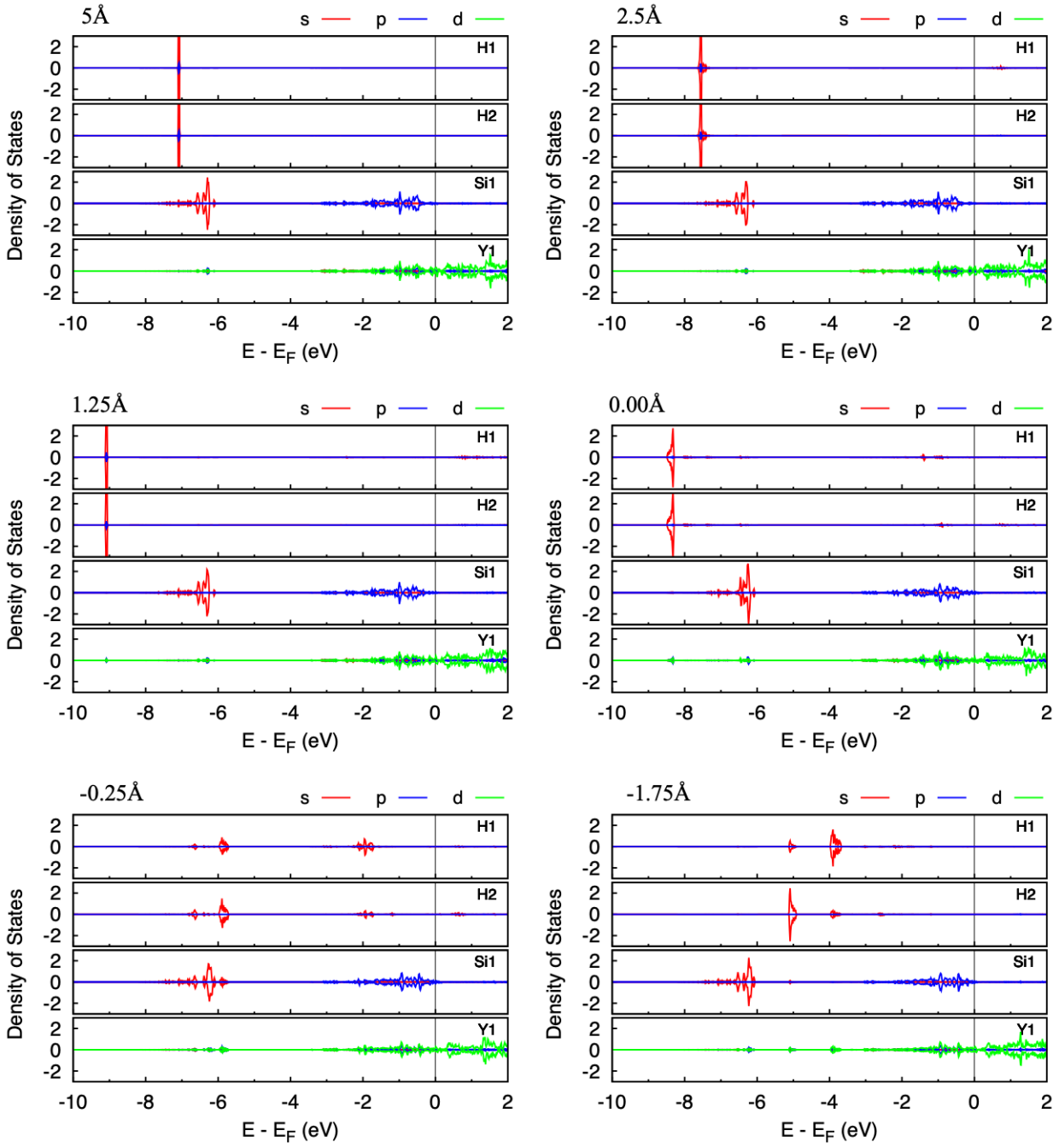


Figure 5. 33 Projected DOS of Y_5Si_3 (001) surface with a hydrogen molecule at difference distances. Y1 and S1 mean the yttrium and silicon atom on the outermost surface.

change in the electron occupation of the hydrogen molecule. However, as the bottom hydrogen atom passes through the outermost surface (at 0 Å), the electron occupancy of the anti-bonding level of the hydrogen molecule begins to appear, which implies a charge transfer from the surface to the hydrogen molecule. As the bottom hydrogen atom passes -0.25 Å, the distance between the two H^- ions increases, and the gap between the bonding and anti-bonding levels of the hydrogen molecule gets narrower. Finally, at -1.75 Å, the two H^- ions are separated into inside and outside of the surface and show weaker interaction.

Even though there is no energy barrier to penetrate the Y-Si ring near the outermost surface of Y_5Si_3, we can see that an energy barrier of 0.08 eV exists at a point 1.25 Å away from the surface. This energy barrier is not for passing through the surface but rather for overcoming a Coulomb repulsion between the hydrogen molecule and the surface, which occurs as the hydrogen molecule approaches the surface. This repulsion can be understood by looking at the differential charge density shown in Fig. 5.32 (b). Near the surface of the material, there exists an electric field accompanied by an increase in electrostatic potential energy, and the polarization of the hydrogen molecule is induced by this electric field as shown in the differential charge density at 2.5 Å. Since the dipole moment of the polarized hydrogen molecule and the surface dipole moment generated due to an electron spill out at the surface are directed in opposite directions, a repulsive force, and thus an energy barrier emerges.

In conclusion, if the energy barrier of 0.08 eV is overcome near the Y_5Si_3 (001) surface, a hydrogen molecule dissociates into two H^- ions, and one H^- ion can pass through the outermost surface without energy barrier. Given that the binding energy of the hydrogen molecule is -4.52 eV [137], 0.08 eV is a very low energy cost to dissociate the hydrogen molecule.

5.4 Summary

The anionic electrons distributed in the 1D hollow channel in Y_5Si_3 lattice was qualitatively and quantitatively analyzed through DFT calculation. As previously reported, it was reconfirmed that anionic electrons exist near the Fermi level in the energy range of $-1.5\ eV < E-E_F < 0$. However, it turned out that this material contains almost twice the anionic electrons (1.488 e/f.u.) than the reported value (0.79 e/f.u.). This study verified that the presence and distribution of these anionic electrons are robust against lattice vibrations. Global structure search revealed that even if Si species is replaced with other group 14 elements (Ge, Sn, and Pb), the structures with the same atomic configuration as Y_5Si_3 are the most stable structures. Except for slight changes in the lattice parameters, they all contain anionic electrons in the 1D hollow space. Furthermore, systematic exploration of $Y_5Si_3H_x$ using crystal structure search revealed a detailed hydrogenation mechanism by identifying favorable hydrogen occupation sites and estimating diffusion barriers between them. The dominant channel of the hydrogen diffusion is a 1D hollow space in which anionic electrons are distributed, and the diffusion rate increases rapidly as a double occupation of hydrogen atoms occurs at the single octahedral site when $x > 1$. However, when the 1D hollow space is saturated with a hydrogen atom ($x > 3$), such fast diffusion cannot occur, which is consistent with the experimental results. Investigation of the interaction between the hydrogen molecule and Y_5Si_3 (001) surface demonstrated that the hydrogen molecule readily dissociates into two H^- ions by absorbing electrons from the surface and one of the hydrides can penetrate the surface without an energy barrier.

Chapter 6

Conclusion and Outlook

The computational materials researches that discover and design new materials with improved target properties have become an integral part of the materials science field and has been accelerated through the combination of the global structure prediction algorithms and first-principles calculations [10,11,13,62,138,139]. Among the various available global structure prediction algorithms, the PSO algorithm has successfully predicted stable atomic configurations of crystalline solids [16,67,130,140], and first-principles calculations based on DFT have been developed to a decent level so that we can accurately predict the electronic, magnetic, and mechanical properties for a given atomic configuration [40,60].

In this study, extensive researches on Cs_xO, $Li_{1+x}Mn_2O_4$, and Y_5Si_3 have been conducted by combining the PSO algorithm and DFT calculations. As the last chapter of this dissertation, I briefly summarize the results and implications of my study and discuss directions for future research.

Cs_xO

In order to overcome the limitations of the experimental characterization of the cesium oxides compounds, computational approaches were applied to understand structural and electronic properties of Cs_xO. Through the global structure prediction, it has been demonstrated that not only the most stable structure, but also metastable structures of Cs_3O compound show the characteristics of electride. Also, surface slab modeling confirmed the decreasing trend of the work function due

to oxidation observed in the experiment [77,78], and we also identified atomic configuration and surface corresponding to the lowest work function, which is 0.66 eV. The thermodynamic stability of this lowest work function surface was investigated by comparing surface free energies, and we demonstrated that the lowest work function surface is stable in a wide range of oxygen chemical potential. Finally, the effect of adatom adsorption on the work function has been explored, and it was revealed that the work function of electride can be reduced by adatom adsorption, and anionic electrons play an important role. However, although the theoretical calculation proved the experimental results related to the work functions of Cs_xO and succeeded in specifying the minimum work function surface, there are still some requirements to further improve the calculation result.

The first relates to the accuracy of the calculated work function values. Although the calculated work functions are well-converged values with respect to the surface slab thickness, the width of the vacuum layer, and the k-point mesh, the computed work functions may vary depending on the exchange-correlation functional selected for calculations [141]. In this study, only GGA functional was utilized to compute the work functions. Although, for the Cs BCC structure, the GGA functional estimated sufficiently accurate work functions compared to the experimental values, it is necessary to verify the accuracy of computed work functions of Cs_xO through calculations using LDA or hybrid functionals. Furthermore, since the Cs is a heavy metal with an atomic number of 55, the relativistic effect such as the spin-orbit coupling on the surface energies and work functions should be explored.

The second is the consideration of the vacancies of the Cs atom at the outermost surface. In this study, perfect cleavages without surface vacancies was considered. However, indeed the surface vacancies result in off-stoichiometry of the outermost surface and affect the surface properties

such as the surface free energy and work function [142]. Therefore, it is also necessary to examine the changes in surface free energies and work functions due to the possible Cs surface vacancies.

Finally, one of the critical variables in changes in work function due to the adatom adsorption is the surface coverage of adsorbate [143]. The surface coverage of adsorbates is directly related to the induced surface dipole moment density, thus affecting the work function. In the case of the Cs_3O $P6_3/mcm$ (#193) structure, which is an electride, it was demonstrated that the adsorption of electronegative adsorbates can lower its work function. We expect that the work function would be reduced further by increasing the surface coverage of adsorbates, and it is required to find the optimum coverage.

$Li_{1+x}Mn_2O_4$

Although the phase transition from the cubic spinel structure ($LiMn_2O_4$) to the tetragonal spinel structure ($Li_2Mn_2O_4$) is known to have a profound effect on the cycle capacity of the battery operation, identifying intermediate structures through experiments has been challenging due to the two-phase reaction of the phase transition [99,110,144]. In this study, intermediate phases are extensively explored by applying the global structure prediction algorithm, and it was revealed that various degrees of freedom interplays in crystal formation in the intermediate composition ($Li_{1.5}Mn_2O_4$). Based on the theoretical exploration of the intermediate structures, we suggest that this diversity of the intermediate phases could deteriorate the cycle capacity, which implies that the cycle capacity can be improved by suppressing those degrees of freedom that occur during the phase transition.

The lithium manganese oxides are a type of strongly correlated material, and the DFT+U approach was used in this study to reflect the strong onsite Coulomb interaction of highly localized

Mn d-electrons. The Hubbard U value for the d-electron of Mn ions in the spinel structure was carefully chosen to be a value that was self-consistently calculated through the linear response theory and first-principles calculations [145]. Although the DFT+U method has been successfully applied to predict and explain various properties of spinel lithium manganese oxides, [146-149], The calculation results of this study need to be verified through other approaches such as DFT+DMFT [55,56] or RDMFT [57,58].

In addition, although our research has successfully described the various degrees of freedom associated with the intermediate phases, specific methods of restraining them have not been revealed in this study. Therefore, to improve the cycle stability, methods to prevent disordered structures in the intermediate phase should be found.

However, it must first be confirmed whether intermediate phases identified through theoretical studies occur during the actual battery operation. Although the experimental identification of intermediate phases has been limited due to the two-phase reactions, it has been found that a solid-solution reaction is possible without domain boundaries in the cathode material constructed by nanocrystalline $LiMn_2O_4$ with a size of 15 nm [24], which suggests the possibility of identifying intermediate structures by employing the neutron powder diffraction technique.

Y_5Si_3

The Y_5Si_3 is an electride where the anionic electrons are confined in the 1D vacant space in the hexagonal lattice. The potential as the catalyst [26] and ion transport material [28] demonstrated in the experiments were verified and explained through theoretical calculations. The presence and distribution of anionic electrons were reconfirmed through the analysis of the projected band structure and Bader charges. However, our study provided a refined description of the anionic

electrons by correcting misinterpretation in the literature [26]. To verify the potential of Y_5Si_3 as a catalyst, electron-donating property of the Y_5Si_3 (001) surface was investigated, and we demonstrated that the degree of the electron-donation varies depending on types of adsorbate, and effective metal atoms for the electron extraction were identified. Furthermore, we shed light on the hydrogenation mechanism of Y_5Si_3, revealing that the 1D hollow space is favorable hydrogen occupation sites and diffusion path. Experimentally observed fast diffusion [28] in the hydrogen content range $1 < x < 2$ was confirmed by evaluating diffusion barriers, and it was shown that the hydrogen molecule can readily dissociate into two H^- ions at the Y_5Si_3 surface.

However, the activation temperature for hydrogen diffusion of Y_5Si_3 is quite high (250°), and rapid diffusion occurs only when a higher temperature is reached (375°) [28]. However, as we demonstrated in section 5.2.4, when the Si atoms are replaced with other group 14 elements, it shows slightly expanded lattice parameters with the same lattice symmetry and atomic configuration. The extension of the lattice parameters leads to the enlargement of the triangular Y-Si ring, which acts as an obstacle to the hydrogen diffusion through the 1D hollow space. Therefore, we expect that the activation temperature for hydrogen diffusion can be lowered by replacing Si atoms with other elements, and we will investigate this in the near future.

Bibliography

[1] P. Hohenberg and W. Kohn, Phys. Rev. **136**, B864 (1964).

[2] W. Kohn and L. J. Sham, Phys. Rev. **140**, A1133 (1965).

[3] G. Kresse and J. Furthmüller, Phys. Rev. B **54**, 11169 (1996).

[4] E. Sanville, S. D. Kenny, R. Smith, and G. Henkelman, J. Comput. Chem. **28**, 899 (2007).

[5] W. Tang, E. Sanville, and G. Henkelman, J. Phys.: Condens. Matter **21**, 084204 (2009).

[6] G. Henkelman, B. P. Uberuaga, and H. Jónsson, J. Chem. Phys. **113**, 9901 (2000).

[7] G. Henkelman and H. Jónsson, J. Chem. Phys. **113**, 9978 (2000).

[8] V. L. Deringer, G. Csányi, and D. M. Proserpio, ChemPhysChem **18**, 873 (2017).

[9] J. Maddox, Nature **335**, 201 (1988).

[10] S. M. Woodley and R. Catlow, Nat. Mater. **7**, 937 (2008).

[11] A. R. Oganov, A. O. Lyakhov, and M. Valle, Acc. Chem. Res. **44**, 227 (2011).

[12] Y. Wang and Y. Ma, J. Chem. Phys. **140**, 040901 (2014).

[13] A. R. Oganov, C. J. Pickard, Q. Zhu, and R. J. Needs, Nat. Rev. Mater. **4**, 331 (2019).

[14] J. Kennedy and R. Eberhart, in *Proceedings of International Conference on Neural Networks* (IEEE, Piscataway, NJ, 1995), pp. 1942–1948.

[15] R. Eberhart and J. Kennedy, in *Proceedings of the Sixth International Symposium on Micro Machine and Human Science* (IEEE, Piscataway, NJ, 1995), pp. 39–43.

[16] Y. Wang, J. Lv, L. Zhu, and Y. Ma, Phys. Rev. B **82**, 094116 (2010).

[17] C. Park, S. W. Kim, and M. Yoon, Phys. Rev. Lett. **120**, 026401 (2018).

[18] J. J. Uebbing and L. W. James, J. Appl. Phys. **41**, 4505 (1970).

[19] V. Giorgis, F. Morini, T. Zhu, J. F. Robillard, X. Wallart, J. L. Codron, and E. Dubois, J. Appl. Phys. **120**, 205108 (2016).

[20] M.-H. Chen and C.-I. Wu, J. Appl. Phys. **104**, 113713 (2008).

[21] A. Hoff, I. Cruz-Cruz, M. C. Siqueira, K. D. Machado, and I. A. Hümmelgen, Sol. Energy Mater. Sol. Cells **171**, 1 (2017).

[22] A. Band, A. Albu-Yaron, T. Livneh, H. Cohen, Y. Feldman, L. Shimon, R. Popovitz-Biro, V. Lyahovitskaya, and R. Tenne, J. Phys. Chem. B **108**, 12360 (2004).

[23] S. Gemming, G. Seifert, C. Muhle, M. Jansen, A. Albu-Yaron, T. Arad, and R. Tenne, J. Solid State Chem. **178**, 1190 (2005).

[24] M. Okubo, Y. Mizuno, H. Yamada, J. Kim, E. Hosono, H. Zhou, T. Kudo, and I. Honma, ACS Nano **4**, 741 (2010).

[25] B. Song, G. M. Veith, J. Park, M. Yoon, P. S. Whitfield, M. J. Kirkham, J. Liu, and A. Huq, Chem. Mater. **31**, 124 (2019).

[26] Y. Lu, J. Li, T. Tada, Y. Toda, S. Ueda, T. Yokoyama, M. Kitano, and H. Hosono, J. Am. Chem. Soc. **138**, 3970 (2016).

[27] M. Kitano, S. Kanbara, Y. Inoue, N. Kuganathan, P. V. Sushko, T. Yokoyama, M. Hara, and H. Hosono, Nat. Commun. **6**, 1 (2015).

[28] I. J. McColm, V. Kotroczo, T. W. Button, N. J. Clark, and B. Bruer, J. Less. Common. Met. **115**, 113 (1986).

[29] I. Toli and S. Zou, Chem. Phys. Lett.: X **2**, 100021 (2019).

[30] M. Born and J. R. Oppenheimer, Ann. Physik **84**, 457 (1927).

[31] L. J. Butler, Annu. Rev. Phys. Chem. **49**, 125 (1998).

[32] S. Pisana, M. Lazzeri, C. Casiraghi, K. S. Novoselov, A. K. Geim, A. C. Ferrari, and F. Mauri, Nat. Mater. **6**, 198 (2007).

[33] G. Kolesov, E. Kaxiras, and E. Manousakis, Phys. Rev. B **98**, 195112 (2018).

[34] M. P. Bircher, E. Liberatore, N. J. Browning, S. Brickel, C. Hofmann, A. Patoz, O. T.

Unke, T. Zimmermann, M. Chergui, P. Hamm, U. Keller, M. Meuwly, H.-J. Woerner, J. Vaníček, and U. Rothlisberger, Structural Dynamics **4**, 061510 (2018).

[35] S. Y. Savrasov and D. Y. Savrasov, Phys. Rev. B **54**, 16487 (1996).

[36] D. Alfè, M. J. Gillan, and G. D. Price, Nature **401**, 462 (1999).

[37] B. G. Walker, C. Molteni, and N. Marzari, J. Phys.: Condens. Matter **16**, S2575 (2004).

[38] R. P. Feynman, Phys. Rev. **56**, 340 (1939).

[39] J. P. Perdew, K. Burke, and M. Ernzerhof, Phys. Rev. Lett. **77**, 3865 (1996).

[40] J. Hafner, J. Comput. Chem. **29**, 2044 (2008).

[41] J. P. Perdew, S. Kurth, A. Zupan, and P. Blaha, Phys. Rev. Lett. **82**, 2544 (1999).

[42] J. Tao, J. P. Perdew, V. N. Staroverov, and G. E. Scuseria, Phys. Rev. Lett. **91**, 146401 (2003).

[43] A. D. Becke, J. Chem. Phys. **98**, 1372 (1993).

[44] K. Kim and K. D. Jordan, Acc. Chem. Res. **98**, 10089 (2002).

[45] J. P. Perdew, M. Ernzerhof, and K. Burke, J. Chem. Phys. **105**, 9982 (1996).

[46] J. Heyd, G. E. Scuseria, and M. Ernzerhof, J. Chem. Phys. **118**, 8207 (2003).

[47] S. Steiner, S. Khmelevskyi, M. Marsmann, and G. Kresse, Phys. Rev. B **93**, 224425 (2016).

[48] H. Jiang, International Journal of Quantum Chemistry **115**, 722 (2015).

[49] V. Anisimov and O. Gunnarsson, Phys. Rev. B **43**, 7570 (1991).

[50] I. V. Solovyev, P. H. Dederichs, and V. I. Anisimov, Phys. Rev. B **50**, 16861 (1994).

[51] V. I. Anisimov, F. Aryasetiawan, and A. I. Lichtenstein, J. Phys.: Condens. Matter **9**, 767 (1997).

[52] O. Bengone, M. Alouani, P. Blöchl, and J. Hugel, Phys. Rev. B **62**, 16392 (2000).

[53] A. Rohrbach, J. Hafner, and G. Kresse, J. Phys.: Condens. Matter **15**, 979 (2003).

[54] B. Himmetoglu, A. Floris, S. de Gironcoli, and M. Cococcioni, International Journal of Quantum Chemistry **114**, 14 (2014).

[55] G. Kotliar, S. Y. Savrasov, K. Haule, V. S. Oudovenko, O. Parcollet, and C. A. Marianetti, Rev. Mod. Phys. **78**, 865 (2006).

[56] K. Held, Advances in Physics (2007).

[57] N. Helbig, N. N. Lathiotakis, and E. K. U. Gross, Phys. Rev. A **79**, 022504 (2009).

[58] S. Di Sabatino, J. A. Berger, L. Reining, and P. Romaniello, J. Chem. Phys. **143**, 024108 (2015).

[59] J. Hafner, Acta Mater. **48**, 71 (2000).

[60] J. Neugebauer and T. Hickel, Wiley Interdisciplinary Reviews: Computational Molecular Science **3**, 438 (2013).

[61] J. Pannetier, J. Bassas-Alsina, J. Rodríguez-Carvajal, and V. Caignaert, Nature **346**, 343 (1990).

[62] J. C. Schön and M. Jansen, Angew. Chem. Int. Ed. Engl. **35**, 1286 (1996).

[63] D. J. Wales and J. P. K. Doye, Acc. Chem. Res. **101**, 5111 (1997).

[64] R. Martoňák, A. Laio, and M. Parrinello, Phys. Rev. Lett. **90**, 075503 (2003).

[65] R. S. Judson, E. P. Jaeger, A. M. Treasurywala, and M. L. Peterson, J. Comput. Chem. **14**, 1407 (1993).

[66] D. M. Deaven and K. M. Ho, Phys. Rev. Lett. **75**, 288 (1995).

[67] H. Wang, Y. Wang, J. Lv, Q. Li, L. Zhang, and Y. Ma, Comput. Mater. Sci. **112**, 406 (2016).

[68] J. I. Malov, M. D. Shebzukhov, and V. B. Lazarev, Surf. Sci. **44**, 21 (1974).

[69] H. B. Michaelson, J. Appl. Phys. **48**, 4729 (2008).

[70] H. E. Ives, Astrophys. J. **60**, 209 (1924).

[71] J. A. Becker, Phys. Rev. **28**, 341 (1926).

[72] J. J. Scheer and J. van Laar, Solid State Commun. **3**, 189 (1965).

[73] L. R. Koller, Phys. Rev. **36**, 1639 (1930).

[74] A. A. Turnbull and G. B. Evans, J. Phys. D: Appl. Phys. **1**, 155 (1968).

[75] W. Klein, J. Appl. Phys. **40**, 4384 (1969).

[76] C. Y. Su, I. Lindau, and W. E. Spicer, Chem. Phys. Lett. **87**, 523 (1982).

[77] P. E. Gregory, P. Chye, H. Sunami, and W. E. Spicer, J. Appl. Phys. **46**, 3525 (1975).

[78] B. Woratschek, W. Sesselmann, J. Küppers, G. Ertl, and H. Haberland, J. Chem. Phys. **86**, 2411 (1987).

[79] T. C. Leung, C. L. Kao, W. S. Su, Y. J. Feng, and C. T. Chan, Phys. Rev. B **68**, 195408 (2003).

[80] P. C. Rusu and G. Brocks, J. Phys. Chem. B **110**, 22628 (2006).

[81] S. Kim, M. Lee, S. Lee, and S. Jhi, J. Phys.: Condens. Matter **29**, 315702 (2017).

[82] H. Föppl, Z. Anorg. Allg. Chem. **291**, 12 (1957).

[83] K.-R. Tsai, P. M. Harris, and E. N. Lassettre, J. Phys. Chem. **60**, 338 (1956).

[84] K.-R. Tsai, P. M. Harris, and E. N. Lassettre, J. Phys. Chem. **60**, 345 (1956).

[85] W. Sun, S. T. Dacek, S. P. Ong, G. Hautier, A. Jain, W. D. Richards, A. C. Gamst, K. A. Persson, and G. Ceder, Sci. Adv. **2**, e1600225 (2016).

[86] J. M. Zhang, Q. Pang, K. W. Xu, and V. Ji, Surf. Interface Anal. **40**, 1382 (2008).

[87] J. M. Zhang, Q. Pang, K. W. Xu, and V. Ji, Comput. Mater. Sci. **44**, 1360 (2009).

[88] Y. Takagi, T. Yamada, M. Yoshino, and T. Nagasaki, Ferroelectrics **490**, 167 (2016).

[89] X. Tian, T. Wang, L. Fan, Y. Wang, H. Lu, and Y. Mu, Appl. Surf. Sci. **427**, 357 (2018).

[90] R. Smoluchowski, Phys. Rev. **60**, 661 (1941).

[91] J. Li, J. Gayles, N. Kioussis, Z. Zhang, C. Grein, and F. Aqariden, J. Electron. Mater. **41**, 2745 (2012).

[92] J. Lerme, P. Dugourd, R. R. Hudgins, and M. F. Jarrold, Chem. Phys. Lett. **304**, 19 (1999).

[93] K. Reuter and M. Scheffler, Phys. Rev. B **65**, 035406 (2001).

[94] G.-X. Qian, R. M. Martin, and D. J. Chadi, Phys. Rev. B **38**, 7649 (1988).

[95] M. S. Whittingham, J. Electrochem. Soc. **123**, 315 (1976).

[96] K. Mizushima, P. C. Jones, P. J. Wiseman, and J. B. Goodenough, Mater. Res. Bull. **15**, 783 (1980).

[97] W. Li, B. Song, and A. Manthiram, Chem. Soc. Rev. **46**, 3006 (2017).

[98] A. Mauger, M. Armand, C. M. Julien, and K. Zaghib, J. Power Sources **353**, 333 (2017).

[99] M. M. Thackeray, W. I. F. David, P. G. Bruce, and J. B. Goodenough, Mater. Res. Bull. **18**, 461 (1983).

[100] M. M. Thackeray, P. J. Johnson, L. A. de Picciotto, P. G. Bruce, and J. B. Goodenough, Mater. Res. Bull. **19**, 179 (1984).

[101] B. A. Ammundsen, J. Rozière, and M. S. Islam, J. Phys. Chem. B. **101**, 8156 (1997).

[102] M. S. Islam and C. A. J. Fisher, Chem. Soc. Rev. **43**, 185 (2014).

[103] T. Ohzuku, M. Kitagawa, and T. Hirai, J. Electrochem. Soc. **137**, 769 (1990).

[104] G. A. Gehring and K. A. Gehring, Rep. Prog. Phys. **38**, 1 (1975).

[105] A. Yamada and M. Tanaka, Mater. Res. Bull. **30**, 715 (1995).

[106] C. Masquelier, M. Tabuchi, K. Ado, R. Kanno, Y. Kobayashi, Y. Maki, O. Nakamura,

and J. B. Goodenough, J. Solid State Chem. **123**, 255 (1996).

[107] H. Hayakawa, T. Takada, H. Enoki, and E. Akiba, J. Mater. Sci. Lett. **17**, 811 (1998).

[108] K. Oikawa, T. Kamiyama, F. Izumi, B. C. Chakoumakos, H. Ikuta, M. Wakihara, J. Li, and Y. Matsui, Solid State Ion. **109**, 35 (1998).

[109] J. Rodríguez-Carvajal, G. Rousse, C. Masquelier, and M. Hervieu, Phys. Rev. Lett. **81**, 4660 (1998).

[110] H. Berg, K. Göransson, B. Noläng, and J. O. Thomas, J. Mater. Chem. **9**, 2813 (1999).

[111] A. Van der Ven, C. Marianetti, D. Morgan, and G. Ceder, Solid State Ion. **135**, 21 (2000).

[112] D. A. Kitchaev, S. T. Dacek, W. Sun, and G. Ceder, J. Am. Chem. Soc. **139**, 2672 (2017).

[113] M. M. Thackeray, Prog. Solid State Chem. **25**, 1 (1997).

[114] R. Freitag and J. Conradie, J. Chem. Educ. **90**, 1692 (2013).

[115] J. L. Dye, Science **301**, 607 (2003).

[116] J. L. Dye, M. R. Yemen, M. G. DaGue, and J. M. Lehn, J. Chem. Phys. **68**, 1665 (1978).

[117] A. Ellaboudy, J. L. Dye, and P. B. Smith, Acc. Chem. Res. **105**, 6490 (1983).

[118] S. B. Dawes, D. L. Ward, R. H. Huang, and J. L. Dye, Acc. Chem. Res. **108**, 3534 (1986).

[119] R. H. Huang, M. K. Faber, K. J. Moeggenborg, D. L. Ward, and J. L. Dye, Nature **331**, 599 (1988).

[120] S. B. Dawes, J. L. Eglin, K. J. Moeggenborg, J. Kim, and J. L. Dye, Acc. Chem. Res. **113**, 1605 (1991).

[121] M. J. Wagner, R. H. Huang, J. L. Eglin, and J. L. Dye, Nature **368**, 726 (1994).

[122] Rui H Huang, Michael J Wagner, Deborah J Gilbert, Kerry A Reidy-Cedergren, Donald L Ward, A. Margaret K Faber, and J. L. Dye, Acc. Chem. Res. **119**, 3765 (1997).

[123] Qingshan Xie, Rui H Huang, Andrew S Ichimura, Richard C Phillips, A. William P Pratt

Jr, and J. L. Dye, Acc. Chem. Res. **122**, 6971 (2000).

[124] J. L. Dye, Acc. Chem. Res. **42**, 1564 (2009).

[125] M. Kitano, Y. Inoue, Y. Yamazaki, F. Hayashi, S. Kanbara, S. Matsuishi, T. Yokoyama, S. W. Kim, M. Hara, and H. Hosono, Nature Chem **4**, 934 (2012).

[126] M. Kitano, Y. Inoue, H. Ishikawa, K. Yamagata, T. Nakao, T. Tada, S. Matsuishi, T. Yokoyama, M. Hara, and H. Hosono, Chemical Science **7**, 4036 (2016).

[127] J. Li, J. Wu, H. Wang, Y. Lu, T. Ye, M. Sasase, X. Wu, M. Kitano, T. Inoshita, and H. Hosono, Chemical Science **10**, 5712 (2019).

[128] T. Inoshita, S. Jeong, N. Hamada, and H. Hosono, Phys. Rev. X **4**, (2014).

[129] T. Tada, S. Takemoto, S. Matsuishi, and H. Hosono, Inorg. Chem. **53**, 10347 (2014).

[130] W. Ming, M. Yoon, M.-H. Du, K. Lee, and S. W. Kim, J. Am. Chem. Soc. **138**, 15336 (2016).

[131] S. Zhao, E. Kan, and Z. Li, Wiley Interdisciplinary Reviews: Computational Molecular Science **6**, 430 (2016).

[132] Y. Toda, S. Matsuishi, K. Hayashi, K. Ueda, T. Kamiya, M. Hirano, and H. Hosono, Advanced Materials **16**, 685 (2004).

[133] H. Yanagi, K.-B. Kim, I. Koizumi, M. Kikuchi, H. Hiramatsu, M. Miyakawa, T. Kamiya, M. Hirano, and H. Hosono, Acc. Chem. Res. **113**, 18379 (2009).

[134] Y. Inoue, M. Kitano, S. W. Kim, T. Yokoyama, M. Hara, and H. Hosono, Acc. Chem. Res. **4**, 674 (2014).

[135] S. Kanbara, M. Kitano, Y. Inoue, T. Yokoyama, M. Hara, and H. Hosono, Acc. Chem. Res. **137**, 14517 (2015).

[136] K. Lee, S. W. Kim, Y. Toda, S. Matsuishi, and H. Hosono, Nature **494**, 336 (2013).

[137] J. R. Rumble, D. R. Lide, and T. J. Bruno, *CRC Handbook of Chemistry and Physics :*, 99 ed. (CRC Press, Boca Raton, FL, 2018).

[138] C. J. Pickard and R. J. Needs, J. Phys.: Condens. Matter **23**, 053201 (2011).

[139] K. T. Butler, J. M. Frost, J. M. Skelton, K. L. Svane, and A. Walsh, Chem. Soc. Rev. **45**, 6138 (2016).

[140] Y. Wang, J. Lv, L. Zhu, S. Lu, K. Yin, Q. Li, H. Wang, L. Zhang, and Y. Ma, J. Phys.: Condens. Matter **27**, (2015).

[141] N. E. Singh-Miller and N. Marzari, Phys. Rev. B **80**, 235407 (2009).

[142] D. L. Price, B. R. Cooper, and J. M. Wills, Phys. Rev. B **48**, 15311 (1993).

[143] R. W. Verhoef and M. Asscher, Surf. Sci. **391**, 11 (1997).

[144] De Li and H. Zhou, Mater. Today **17**, 451 (2014).

[145] F. Zhou, M. Cococcioni, C. A. Marianetti, D. Morgan, and G. Ceder, Phys. Rev. B **70**, 235121 (2004).

[146] B. Xu and S. Meng, J. Power Sources **195**, 4971 (2010).

[147] R. C. Longo, F. T. Kong, S. KC, M. S. Park, J. Yoon, D. H. Yeon, J. H. Park, S. G. Doo, and K. Cho, Phys. Chem. Chem. Phys. **16**, 11233 (2014).

[148] K. Hoang, J. Mater. Chem. A **2**, 18271 (2014).

[149] W.-W. Liu, D. Wang, Z. Wang, J. Deng, W.-M. Lau, and Y. Zhang, Phys. Chem. Chem. Phys. 19, 6481 (2017).

Vita

Jinseon Park was born in Chungju, South Korea. He attended Korea Military Academy from 2002 to 2006 where he received his Bachelor's degree in Applied Physics. After completion of his undergraduate degree, he served as a platoon leader and battalion staff officer for two years at the borderline between South and North Korea. In 2010, Jinseon Park earned his Master's degree in Physics from Texas A&M University-College Station with a concentration in biophysics. Following the completion of his M.S, he worked as an instructor for five years at Korea Military Academy. In 2015, he joined a Ph.D. program in the Department of Physics and Astronomy at the University of Tennessee-Knoxville and conducted his research at the Center for Nanophase Materials Sciences in Oak Ridge National Laboratory under the supervision of Dr. Mina Yoon. In the summer of 2020, Jinseon Park completed his Ph.D. in physics with a concentration in theoretical and computational condensed matter physics.